Far-Field Characterization and Control of Propagating Ultrashort Optical Near Fields

Dissertation zur Erlangung des
naturwissenschaftlichen Doktorgrades
der Julius-Maximilians-Universität
Würzburg

vorgelegt von
Christian Rewitz
aus Berlin

Würzburg 2014

Eingereicht am 26. November 2013
bei der Fakultät für Physik und Astronomie

1. Gutachter: Prof. Dr. Tobias Brixner
2. Gutachter: Prof. Dr. Bert Hecht
der Dissertation

1. Prüfer: Prof. Dr. Tobias Brixner
2. Prüfer: Prof. Dr. Bert Hecht
3. Prüfer: Prof. Dr. Wolfgang Kinzel
im Promotionskolloquium

Tag des Promotionskolloquiums: 26. März 2014

Doktorurkunde ausgehändigt am: _____

List of Publications

[Rewitz12a]
Rewitz, C.; Keitzl, T.; Tuchscherer, P.; Goetz, S.; Geisler, P.; Razinskas, G.; Hecht, B.; and Brixner, T.
Spectral-interference microscopy for characterization of functional plasmonic elements.
Optics Express **20(13)**, 14632-14647 (2012).

[Rewitz12b]
Rewitz, C.; Keitzl, T.; Tuchscherer, P.; Huang, J.-S.; Geisler, P.; Razinskas, G.; Hecht, B.; and Brixner, T.
Ultrafast Plasmon Propagation in Nanowires Characterized by Far-Field Spectral Interferometry.
Nano Letters **12(1)**, 45-49 (2012).

[Brixner13]
Brixner, T.; Aeschlimann, M.; Fischer, A.; Geisler, P.; Goetz, S.; Hecht, B.; Huang, J.-S.; Keitzl, T.; Kramer, C.; Melchior, P.; Pfeiffer, W.; Razinskas, G.; Rewitz, C.; Schneider, C.; Strüber, C.; Tuchscherer, P.; and Voronine, D. V.
Coherent spectroscopies on ultrashort time and length scales.
Ultrafast Phenomena XVIII, EPJ Web of Conferences **41**, 09017 (2013).

[Geisler13]
Geisler, P.; Razinskas, G.; Krauss, E.; Wu, X.-F.; Rewitz, C.; Tuchscherer, P.; Goetz, S.; Huang, C.-B.; Brixner, T.; and Hecht, B.
Multimode Plasmon Excitation and In Situ *Analysis in Top-Down Fabricated Nanocircuits.*
Physical Review Letters **111(18)**, 183901–5 (2013).

[Rewitz14]
Rewitz, C.; Razinskas, G.; Geisler, P.; Krauss, E.; Goetz, S.; Pawłowska, M.; Hecht, B.; and Brixner, T.
Coherent Control of Plasmon Propagation in a Nanocircuit.
Physical Review Applied **1(1)**, 014007–6 (2014).

The publications overleaf have partly been used in this dissertation as detailed in the following table. The initial version of each publication was written by the respective first author. Subsequent versions were influenced by the co-authors and edited by the first author. Sources of published figures within the dissertation are indicated in the respective captions.

Publication		Usage	Dissertation
[Rewitz12a]	pp. 3–13	text reproduced, modified, and extended	pp. 31–45
	pp. 14–15	text reproduced	pp. 82–83
	pp. 15–16	text reproduced and extended	pp. 84–85
[Rewitz12b]	pp. 1,3,4	parts of text reproduced, modified, and extended	pp. 47–51
	p. 2	parts of text reproduced	p. 35
	p. 4	part of text reproduced and extended	p. 81
[Geisler13]	pp. 2,4,5	parts of data and results reproduced	pp. 54–57
[Rewitz14]	pp. 1–5	text reproduced, modified, and extended	pp. 59–72
	supplemental	parts of text reproduced, modified, and extended	pp. 60–62
	supplemental	parts of text reproduced and modified	pp. 70–71
	supplemental	parts of text reproduced	pp. 85–86

Abstract

In this work, femtosecond laser pulses are used to launch optical excitations on different nanostructures. The excitations are confined below the diffraction limit and propagate along the nanostructures. Fundamental properties of these ultrashort optical near fields are determined by characterizing the far-field emission after propagation with a setup developed for this task. Furthermore, control of the nanooptical excitations' spatial and temporal evolution is demonstrated for a designed nanostructure.

Contents

1 Introduction

Optics is an important and interesting branch of physics that deals with light and its interaction with matter. A significant tool in this and other fields is the laser. It provides spatially and temporally coherent light beams for versatile experiments. In addition to narrow-band, continuous radiation there also exist spectrally broadband femtosecond pulses that are derived from mode-locked lasers. Together with sophisticated spectroscopic techniques, these ultrashort pulses allow tracking of ultrafast processes, e.g., the breaking of bonds in photochemical reactions after absorption of a photon. Furthermore, the spectral width of these laser pulses facilitates investigation of broad or multiple resonances at once.

In laboratories, laser light is usually guided as a free-space collimated beam. For other applications this is not desired or possible. For instance, intercontinental digital communication employs pulsed light transport via dielectric optical fibers. Compared to information transport via electrical transmission lines, the use of light is more efficient since the available bandwidth is much larger. Furthermore, optical fibers can span exceptionally long distances without the need of amplifiers, even though the first dielectric waveguides were short and lossy. On the other hand, when it comes to integration, dielectric waveguiding is limited by the fundamental law of diffraction and cannot compete with the footprint size of cutting-edge electronics.

Fortunately, the diffraction limit can be overcome by using metal waveguides. At metal–dielectric interfaces photons can interact with the surface electron density of the conductor to form so-called surface plasmon polaritons. These quasi particles encompass optical fields that propagate along the interface. Due to the evanescent decay of the optical fields perpendicular to the interface, the fields are highly confined to the metal surface and are, therefore, also termed near fields. Inherent to this sub-diffraction limited confinement is a field enhancement that can be orders of magnitude if localized resonances are involved [Novotny11]. The resulting increased light–matter interaction on the nanoscale opened up a wide research area [Biagioni12] and is employed in applications such as surface-enhanced Raman spectroscopy (SERS) [Jeanmaire77]. Thanks to the developments in nanotechnology that allow tailoring of metallic structures on the nanometer scale, the research field of plasmonics has emerged [Halas10]. It explores unique properties of the electromagnetic modes at nanostructured metal surfaces to find new physical effects and develop optical devices at the nanoscale [Lindquist12]. Today, plasmonics is an interdisciplinary area of research [Bozhevolnyi08] that combines interests in chemistry, biology, engineering, non-linear optics, and physics as a variety of applications have emerged. Examples include fluorescent enhancement, bio-sensing and -labeling, photovoltaics, nano imaging, and high-density optical data storage [Hayashi12].

Combining plasmonics and ultrafast laser pulses yields new possibilities for fundamental spectroscopic research and applications. Since this work deals with this combination, some theoretical background and experimental methods of both fields are introduced in Chapter 2.

An application that awakes a lot of interest is the future hybrid integration of photonic, plasmonic, and electronic functional elements for signal processing [Zia06]. The integration of photonic and plasmonic elements can also be termed ultrafast optical nano circuitry. For such circuits any integrated plasmonic element has to include the conversion from optical far field into near field modes at an input. The optical near fields then propagate and are processed, before being converted back into photons at an output [Barnes03]. Moreover, the elements should support a broad spectral width to allow the use of ultrashort pulses for ultrafast signal processing. The characterization of the overall performance, i.e., the response function, of such integrated plasmonic elements requires an optical technique with high spatial and ultrafast temporal resolution.

In this work, a setup that meets exactly these demands is presented in Chapter 3. The setup is termed spectral-interference microscope and is capable of measuring spatial-spectral response functions of plasmonic structures including integrated elements. From these response functions the group velocity and dispersion of propagating optical near fields are deduced. Both characteristics are of particular interest in the context of integrated plasmonic circuitry where signal delays are important for the implementation of, e.g., interferometric logic gates. Another application in which group velocity and dispersion are important is plasmonic nanofocusing as an option to transport light energy to a single molecule [Berweger12]. Plasmonic nanofocusing uses propagating near-field modes to concentrate optical energy at the tip of tapered metallic nanowires. The technique could lead to background-free near-field spectroscopy with ultrafast temporal resolution.

In Chapter 4 of this work the results of group velocity and dispersion measurements of various nanostructures that are suitable for nanooptical circuits and other applications are discussed. Thus, far-field characterization of propagating optical near fields is accomplished.

After this characterization part, the accumulated knowledge is used to implement control over near fields. Controlling the spatiotemporal evolution of near-field propagation is a key feature that will enhance the functionality of future nanooptical circuits and theoretical work showed that coherent control concepts can be applied for this task [Stockman02, Sukharev06, Tuchscherer09]. In these control schemes a far-field laser pulse—determined by its spectral amplitude, phase, and polarization—excites a particular superposition of near-field modes. Interference of these modes can then lead to light guidance and femtosecond energy localization at the nanoscale. To achieve this control, coherent and quantitative superposition of well-defined propagating near-field modes is a requirement. However, independent control over light coupling and propagation properties for plasmonic circuits is not trivial. Therefore, in Chapter 5, a designed nanocircuit meeting these demands is used to experimentally demonstrate single-pulse routing and spatiotemporal control. This fundamental implementation of the coherent control concept in the field of ultrafast plasmonics opens up new possibilities for research and applications.

2 Theoretical Background and Experimental Methods

Since this dissertation deals with propagating optical near fields that are excited using femtosecond laser pulses, this chapter first introduces some general, mathematical properties of these laser pulses (Section 2.1) and a method to characterize them (Section 2.2). Subsequently, the technique of confocal microscopy, which provides a basis for all experiments, is explained (Section 2.3). The chapter closes with a discussion of fundamental properties of propagating optical near fields in different (nano)structures (Section 2.4).

2.1 Femtosecond Laser Pulses

In the classical description of electromagnetism, Maxwell's equations describe the behavior of electric and magnetic fields. For a linear, homogeneous, isotropic, and nonmagnetic medium and in the absence of external charges or current densities theses equations can be combined to yield the so-called wave equation for the electric field $\vec{E}$. This equation shows that spatiotemporal electric distortions propagate as waves through the medium [Hecht02]:

$$\nabla^2 \vec{E}(\vec{r},t) - \varepsilon_0 \mu_0 \varepsilon \frac{\partial^2}{\partial t^2} \vec{E}(\vec{r},t) = 0. \tag{2.1}$$

The permittivity and permeability of vacuum are denoted ε_0 and μ_0, respectively. The permittivity of the medium is described by ε. Usually, the permittivity is a complex number and a decomposition into the real-valued refractive index n and extinction coefficient κ is defined by [Maier07]

$$\sqrt{\varepsilon} = n + \mathrm{i}\kappa. \tag{2.2}$$

A possible solution of Eq. (2.1) is a monochromatic plane wave with a polarization dependent amplitude $\vec{E_0}$ whose spatial propagation and temporal evolution is characterized by a complex-valued wave vector $\vec{k}$ and the oscillation frequency ω, respectively:

$$\vec{E}(\vec{r},t) = \vec{E_0} \cos(\vec{k}\vec{r} \pm \omega t) = \frac{\vec{E_0}}{2} \mathrm{e}^{\mathrm{i}(\vec{k}\vec{r} \pm \omega t)} + c.c. \tag{2.3}$$

Here, the $\pm$-sign defines the propagation direction as parallel or anti-parallel to the wave vector $\vec{k}$ and "$c.c.$" refers to the complex conjugate. Because the electric field is real valued, the term that is written out in the exponential notation determines the field unambiguously and, thus, is sometimes used alone. Similar to the oscillation frequency that defines the time $T = 2\pi/\omega$ it takes for the electric field to pass through its cycle, the wave vector specifies the wavelength, i.e., dimensions of spatial oscillations, via $\lambda = 2\pi/\,\mathrm{Re}[k]$, where Re[ ] denotes

the real part. The imaginary part of the wave vector accounts for possible absorption upon propagation. For wavelengths between approximately 400 nm and 750 nm (i.e., for oscillation frequencies between 4.7 rad/fs and 2.5 rad/fs) the electromagnetic waves are called visible light.

The monochromatic waves described so far are continuous in time. However, pulsed near-infrared radiation from a home-built Ti:Sapphire laser is used in this dissertation. In the following discussion, partly based on [Langhojer09], [Tuchscherer12], and the references therein, some mathematical aspects of these ultrashort pulses are presented.

Representation in Temporal and Frequency Domain

In contrast to an ideal plane wave, a laser beam does not extend infinitely perpendicular to the propagation direction, which is, e.g., defined along the z axis. Often, the transverse profile has a Gaussian shape that is accounted for with a space-dependent amplitude $\vec{E}_0(x, y, 0)$. The propagation of this profile can be described with Gaussian beam optics [CVI09]. However, to describe femtosecond laser pulses it is instructive to consider a fixed point in space and neglect any spatial dependency as well as the vector character of the field. Then, the pulse duration in which the fast temporal oscillations of the field at the so-called carrier frequency ω_0 occur, can be encoded into a temporal envelope $2A(t)$ and the scalar electric field is written as

$$\begin{aligned} E(t) = 2A(t)\cos[\phi(t)] &= A(t)\,\mathrm{e}^{\mathrm{i}\phi(t)} + c.c. \\ &= E^{+}(t) + c.c. \\ &= E^{+}(t) + E^{-}(t). \end{aligned} \tag{2.4}$$

Here, a temporal phase $\phi(t) = \omega_0 t + \varphi(t)$ has been introduced. It is separated into the carrier frequency part $\omega_0 t$ and a temporally varying term $\varphi(t)$ that allows to model, e.g., a variation of the momentary frequency of a laser pulse [Wollenhaupt07]. Again, the function $E^{+}(t)$ describes the field unambiguously because the electric field is real valued.

The temporal intensity $I(t)$ of a laser pulse is proportional to the temporal average of the squared electric field and can be computed via

$$I(t) = \varepsilon_0 cn\langle E^2(t)\rangle = \varepsilon_0 cn\frac{1}{T}\int_{t-T/2}^{t+T/2} E^2(t')\mathrm{d}t' = 2\varepsilon_0 cnA^2(t), \tag{2.5}$$

where $c = 1/\sqrt{\varepsilon_0\mu_0}$ is the speed of light in vacuum and n is the refractive index of the medium in which the measurement takes place [cf. Eq. (2.2)]. To calculate the integral in Eq. (2.5), the slowly varying envelope approximation has been used, which assumes that the amplitude of the laser pulse envelope is almost constant during one oscillation cycle [Diels06]. For the simple laser pulses used in this dissertation, the pulse duration is defined as the full-width at half-maximum (FWHM) of the temporal intensity:

$$\Delta t = \mathrm{FWHM}\{I(t)\}. \tag{2.6}$$

Femtosecond laser pulses can also be described in the frequency domain. An equivalent expression to $E^{+}(t)$ can be given by applying a Fourier transform to this complex-valued

function:

$$E^+(\omega) = \frac{1}{\sqrt{2\pi}} \int_{-\infty}^{\infty} E^+(t)\, \mathrm{e}^{-\mathrm{i}\omega t}\, \mathrm{d}t. \tag{2.7}$$

The temporal electric field can be recovered by an inverse Fourier transform, which basically shows that a laser pulse can be decomposed into monochromatic waves:

$$E^+(t) = \frac{1}{\sqrt{2\pi}} \int_{-\infty}^{\infty} E^+(\omega)\, \mathrm{e}^{\mathrm{i}\omega t}\, \mathrm{d}\omega. \tag{2.8}$$

It can be shown that $E^+(\omega)$ is the positive frequency part of the Fourier transform of the real-valued electric field [Diels06], i.e.,

$$E^+(\omega) = \begin{cases} E(\omega) & \text{if} \quad \omega \geq 0, \\ 0 & \text{if} \quad \omega < 0, \end{cases} \tag{2.9}$$

with

$$E(\omega) = \frac{1}{\sqrt{2\pi}} \int_{-\infty}^{\infty} E(t)\, \mathrm{e}^{-\mathrm{i}\omega t}\, \mathrm{d}t, \qquad \text{and} \qquad E(t) = \frac{1}{\sqrt{2\pi}} \int_{-\infty}^{\infty} E(\omega)\, \mathrm{e}^{\mathrm{i}\omega t}\, \mathrm{d}\omega. \tag{2.10}$$

In analogy to Eq. (2.4), the field can be separated into a real-valued spectral amplitude $A(\omega)$ and a spectral phase $\varphi(\omega)$

$$E^+(\omega) = A(\omega)\, \mathrm{e}^{-\mathrm{i}\varphi(\omega)}. \tag{2.11}$$

The finite width of spectral amplitudes is a direct consequence of the temporal envelope function, i.e., the temporal finite duration of a pulse manifests itself in a spectral bandwidth. The spectral intensity is calculated analogously to the temporal intensity

$$I(\omega) = 2\varepsilon_0 cnA^2(\omega), \tag{2.12}$$

and the spectral bandwidth is defined as the full-width at half-maximum of the spectral intensity

$$\Delta\omega = \mathrm{FWHM}\{I(\omega)\}, \tag{2.13}$$

which again is only sensible for the simple pulses as used in this dissertation.

Propagation and Dispersion

Having introduced the spectral representation of a laser pulse, the spatial dependency that has been neglected so far can be reconsidered. For this purpose, the wave equation [Eq. (2.1)] is transferred to the frequency domain by plugging in the corresponding description of the electric field [Eq. (2.10)]:

$$\nabla^2 \vec{E}(\vec{r}, \omega) + \frac{\omega^2}{c^2} \varepsilon(\omega) \vec{E}(\vec{r}, \omega) = 0. \tag{2.14}$$

This choice of representation has two advantages. First, the description inherently deals with monochromatic waves and their superposition. Second, it contains the frequency dependent permittivity $\varepsilon(\omega)$ of materials that can be measured experimentally, e.g., with spectroscopic ellipsometry [Fujiwara07], whereas an instantaneous response is assumed in the time domain representation [cf. Eq. (2.1)]. A straightforward solution of Eq. (2.14) is a monochromatic propagating plane wave and reads

$$\vec{E}(\vec{r},\omega) = \vec{E}(\vec{r}_0,\omega)\,\mathrm{e}^{\mathrm{i}\vec{k}\vec{r}}, \tag{2.15}$$

where the magnitude of the wave vector is given by the so-called dispersion relation

$$k^2 = k_x^2 + k_y^2 + k_z^2 = \frac{\omega^2}{c^2}\varepsilon(\omega), \tag{2.16}$$

as can be deduced easily when plugging the plane wave solution in Eq. (2.14).

In order to discuss propagation and dispersion effects, a linearly polarized laser pulse propagating along the z axis is considered. Again, only the positive frequency part [cf. Eq. (2.11)] is used to yield

$$E^+(z,\omega) = E^+(0,\omega)\,\mathrm{e}^{\mathrm{i}k_z(\omega)z} = A(0,\omega)\,\mathrm{e}^{-\mathrm{i}\varphi(z,\omega)}\,. \tag{2.17}$$

Here, the propagation factor $k_z(\omega)z$ has been included into the spectral phase $\varphi(z,\omega)$. By using the dispersion relation [Eq. (2.16), with $k_x = k_y = 0$] and Eq. (2.2) the spectral phase can then be written as

$$\varphi(z,\omega) = \varphi(0,\omega) - k_z(\omega)z = \varphi(0,\omega) - \frac{\omega}{c}[n(\omega) + \mathrm{i}\kappa(\omega)]z, \tag{2.18}$$

and can be viewed as a transfer function for pulse propagation in a medium. The extinction coefficient $\kappa(\omega)$ can be included into a real-valued amplitude $\hat{A}(z,\omega) = A(0,\omega)\,\mathrm{e}^{-\kappa(\omega)z}$ and the remaining real-valued spectral phase can be expanded into a Taylor series. This expansion is done around the carrier frequency ω_0, which is usually defined at the center of the spectral amplitude and, therefore, is often called center frequency:

$$\varphi(z,\omega) = \sum_{j=0}^{\infty} \frac{b_j}{j!}\,(\omega-\omega_0)^j \qquad \text{with } b_j = \left.\frac{\mathrm{d}^j\varphi(z,\omega)}{\mathrm{d}\omega^j}\right|_{\omega=\omega_0} \tag{2.19}$$

The coefficients b_j of this expansion can be written as

$$b_j = \left.\frac{\mathrm{d}^j\varphi(0,\omega)}{\mathrm{d}\omega^j}\right|_{\omega=\omega_0} + \frac{z}{c}\left(j\frac{\partial^{j-1}n(\omega)}{\partial\omega^{j-1}} + \omega\frac{\partial^j n(\omega)}{\partial\omega^j}\right)\Big|_{\omega=\omega_0}. \tag{2.20}$$

Hence, for a pulse with a constant spectral phase at $z = 0$ the propagation in vacuum ($n = 1$) yields only the coefficient $b_1 = z/c$, i.e., a linear spectral phase. The value of b_1 corresponds to the time Δt that the maximum of the temporal pulse envelope needs to propagate the distance z. Thus, a linear spectral phase corresponds to a shift of the temporal profile. This interrelation can also be deduced from the Fourier shift theorem applied to Eq. (2.10), but was introduced here via the spectral phase modulation upon propagation.

If the pulse propagates in a different medium, the spectral dependency of the refractive index $n(\omega)$ will lead to a higher-order spectral phase, i.e., $b_j \neq 0$ for $j > 1$. This is called

dispersion and usually elongates the pulse duration. For further information on temporal pulse shape manipulation via control of the spectral phase (and spectral amplitude) the reader is referred to the literature, e.g., [Wollenhaupt07] or [Brixner01a].

On the other hand, if the spectral phase of a laser pulse before entering and after exiting an element can be measured, the spectral phase transfer (or response) function of this element can be determined. For that, it is elementary to be able to measure spectral phases of femtosecond laser pulses, which is discussed in the next section.

2.2 Spectral Interferometry

It was shown in the last section that an ultrashort laser pulse is defined uniquely by $E^+(t)$ or $E^+(\omega)$. One of these quantities has to be determined for a complete characterization of a laser pulse. This is not a trivial task. To satisfy the Nyquist theorem in the time domain, the fast oscillations of $E(t)$ or $E^2(t)$ would have to be resolved by a device with a response time faster than $T/2$. For the pulses used in this dissertation this time is on the order of femtoseconds. On the other hand, $I(\omega)$ can be measured easily. A calibrated spectrometer can directly determine $I(\lambda)$ and the spectral intensity can be computed via the Jacobi transformation [Wollenhaupt07]

$$I_\omega(\omega) = (-)\frac{2\pi c}{\omega^2} I_\lambda(\frac{2\pi c}{\omega}), \tag{2.21}$$

where the minus sign indicates that the direction of axes changes. The spectral bandwidth in λ-space is defined analogously to Eq. (2.13): $\Delta\lambda = \mathrm{FWHM}\{I(\lambda)\}$. However, the phase information gets lost if intensities are measured. Nevertheless, there are many advanced measurement techniques that give access to the spectral phase of ultrashort pulses. A popular technique is frequency-resolved optical gating (FROG). It employs a delayed copy of the pulse (autocorrelation), a nonlinear process, spectrally resolved detection, and an iterative algorithm to reconstruct the phase (and amplitude) of an unknown laser pulse [Kane93, Trebino93, Trebino02]. A comprehensive overview of other techniques can be found, e.g., in [Dorrer01].

For the purpose of response function characterization of plasmonic elements in this dissertation, it is sufficient to employ a technique that yields the difference phase $\varphi_{\mathrm{diff}}(\omega) = \varphi(\omega) - \varphi_{\mathrm{ref}}(\omega)$ between a signal and a reference pulse. One of these techniques is called spectral interferometry [Lepetit95]. The phase evaluation in this method is noniterative and the detection scheme is linear in intensity. Therefore, spectral interferometry offers robustness and high sensitivity. This is essential to characterize weak signals emitted by nanostructures. Furthermore, complete characterization of the signal pulse is possible if the (usually more intense) reference pulse is characterized with a different technique, such as FROG. Then, the spectral phase of the signal pulse can be computed easily, as shown in the following.

The experimental setup for spectral interferometry used in this dissertation is shown in Fig. 2.1 and consists basically of an interferometer and a spectrometer. In the case discussed here, the spectral phase that a laser pulse accumulates upon traversing a microscope objective (cf. Section 2.3) twice is considered in order to introduce the technique. For this task the linearly polarized input pulse is divided into a reference pulse $E^+_{\mathrm{ref}}(\omega) = A_{\mathrm{ref}}(\omega)\,\mathrm{e}^{-\mathrm{i}\varphi_{\mathrm{ref}}(\omega)}$ and

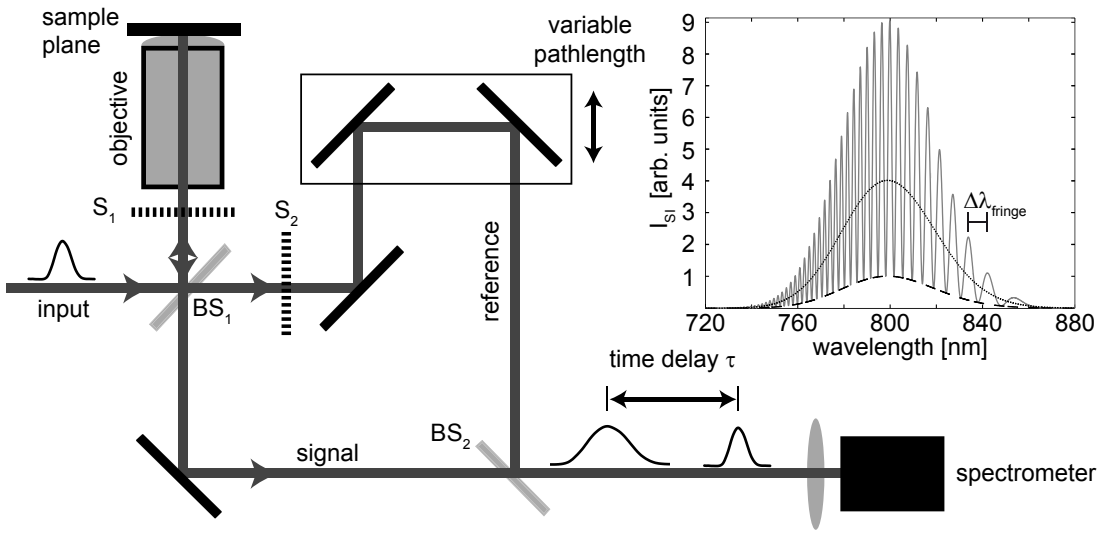

Figure 2.1: Schematic setup for a spectral-interferometry measurement in a microscope. The input pulse is split into a reference and signal pulse at BS_1. The reference pulse is guided via a delay stage to BS_2, where it is collinearly recombined with the signal pulse, which was reflected in the sample plane of the objective. Both pulses are focused into a spectrometer and both intensities can be measured independently by using automated shutters (S_1, S_2). Due to dispersion upon traversing the objective (and one beam splitter more than the reference pulse) the signal pulse accumulates more higher-order spectral phase than the reference pulse, i.e., it is temporally stretched (cf. Section 2.1). The interference of both pulses at a fixed time delay τ results in fringes in the detected spectral intensity. In the inset, the simulated spectral interference pattern (solid gray) for a typical input pulse used in the experimental part of this dissertation ($\lambda_0 = 800\,\mathrm{nm}$, $\Delta\lambda = 46\,\mathrm{nm}$), a time delay of $\tau = 600\,\mathrm{fs}$, and a second-order spectral phase of $b_2/2 = 1500\,\mathrm{fs}^2/\mathrm{rad}^2$ [cf. Eq. (2.19)] for the signal pulse is shown. Due to the nonlinear spectral phase, the fringe spacing $\Delta\lambda_{\mathrm{fringe}}$ of the interference pattern varies significantly with wavelength. The corresponding spectral intensities of the reference and signal pulse are shown with black lines (dotted and dashed, respectively).

a signal pulse $E^+(\omega) = A(\omega)\,\mathrm{e}^{-\mathrm{i}\varphi(\omega)}$ at the first beam splitter (BS_1). The reference pulse can be delayed or accelerated by a variable path length. The signal pulse is transmitted through to the objective and reflected back in the sample plane. Afterwards it is recombined collinearly with the reference pulse at the second beam splitter (BS_2) and subsequently focused into a spectrometer. The delay τ is kept fixed during the measurement.

Even though both pulses do not overlap in time, a spectral interference pattern can be recorded with the spectrometer, as shown in the inset (solid gray curve). The fringe separation depends on the temporal delay τ [$\Delta\lambda_{\mathrm{fringe}} = (\lambda^2/c)(1/\tau)$] and the difference phase $\varphi_{\mathrm{diff}}(\omega)$. For a constant or linear spectral difference phase and spectral bandwidths used in this dissertation, $\Delta\lambda_{\mathrm{fringe}}$ is almost constant along the wavelength axis. In Fig. 2.1, the example difference phase has a quadratic dependence on the frequency, with $b_2/2 = 1500\,\mathrm{fs}^2/\mathrm{rad}^2$ [cf. Eq. (2.19)]. Therefore, the fringe separation significantly varies with wavelength. In the following, the general theoretical principle of spectral-interference data evaluation for phase retrieval is discussed. A more specific and experimental description for spectral-interference microscopy is given in Section 3.3.

Mathematically, the recorded interference pattern in the frequency domain can be expressed as the squared superposition of the two complex-valued electric fields. By omitting the proportionality factors of Eq. (2.12) for the sake of simplicity, the expression can be written as

$$I_{SI}(\omega) = \left| E^{+}_{\mathrm{ref}}(\omega) + E^{+}(\omega)\, \mathrm{e}^{-\mathrm{i}\omega\tau} \right|^2 . \tag{2.22}$$

Here, the relative separation of the pulses is encoded in the delay term $-\omega\tau$ that is added to the spectral phase of the signal pulse [cf. Eq.(2.19), $b_1 = \tau$; the constant term $\tau\omega_0$ is left out for clarity]. The delay term can also be included in the definition of $\varphi(\omega)$ but is written separately here. The spectral intensities $I(\omega) = A^2(\omega)$ and $I_{\mathrm{ref}}(\omega) = A^2_{\mathrm{ref}}(\omega)$ are measured independently with the help of automatic shutters ($\mathrm{S}_1, \mathrm{S}_2$ in Fig. 2.1) and can be subtracted from the interference pattern to yield the interference term

$$\begin{aligned} S(\omega) &= I_{SI}(\omega) - I(\omega) - I_{\mathrm{ref}}(\omega) && (2.23)\\ &= \left[E^{+}_{\mathrm{ref}}(\omega)\right]^{*} E^{+}(\omega)\, \mathrm{e}^{-\mathrm{i}\omega\tau} + E^{+}_{\mathrm{ref}}(\omega) \left[E^{+}(\omega)\right]^{*} \mathrm{e}^{\mathrm{i}\omega\tau} && (2.24)\\ &= 2\sqrt{I_{\mathrm{ref}}(\omega) I(\omega)} \cos\left[\varphi_{\mathrm{ref}}(\omega) - \varphi(\omega) - \omega\tau\right], && (2.25) \end{aligned}$$

which contains the desired difference phase. Here, the star denotes complex conjugation. Equation (2.25) also illustrates the sensitivity of the technique: The absolute modulation depth of the interference pattern is a factor $4\sqrt{I_{\mathrm{ref}}(\omega)}$ larger than the amplitude $\sqrt{I(\omega)}$ of the signal field. This holds also in the wavelength domain and can be seen in the inset of Fig. 2.1, where the reference intensity (dotted) is four times larger than the signal intensity (dashed) and the modulation depth of the spectral interference signal (gray) is eight times larger than the signal intensity.

The direct evaluation of Eq. (2.25) via the arc-cosine function can lead to large phase errors in spectral regions where the cosine approaches unity [Lepetit95]. Therefore, a Fourier transform filtering method that allows to replace the unwanted cosine function with a complex-valued relation is explained in the following. This procedure is much less sensitive to noise than the direct evaluation. An intuitive access to the method can be deduced from Eq. (2.24): The inverse Fourier transform of the physically observable and, thus, real-valued interference term must result in two parts that carry the same information. The main oscillation frequency of $S(\omega)$, which is proportional to τ, is encoded in both inverse Fourier transformed parts with a shift from the DC position by $\pm\tau$ (cf. Figs. 3.5c,d):

$$\begin{aligned} S(t) &= \frac{1}{\sqrt{2\pi}} \int_{-\infty}^{\infty} S(\omega)\, \mathrm{e}^{\mathrm{i}\omega t}\, \mathrm{d}\omega \\ &= \frac{1}{\sqrt{2\pi}} \int_{-\infty}^{\infty} \left[E^{+}_{\mathrm{ref}}(\omega)\right]^{*} E^{+}(\omega)\, \mathrm{e}^{\mathrm{i}\omega(t-\tau)}\, \mathrm{d}\omega \\ &\quad + \left\{ \frac{1}{\sqrt{2\pi}} \int_{-\infty}^{\infty} \left[E^{+}_{\mathrm{ref}}(\omega)\right]^{*} E^{+}(\omega)\, \mathrm{e}^{\mathrm{i}\omega(-t-\tau)}\, \mathrm{d}\omega \right\}^{*} \\ &= \tilde{S}(t-\tau) + \tilde{S}^{*}(-t-\tau), && (2.26) \end{aligned}$$

with

$$\begin{aligned}\tilde{S}(t) &= \frac{1}{\sqrt{2\pi}} \int_{-\infty}^{\infty} \left[E^{+}_{\mathrm{ref}}(\omega)\right]^{*} E^{+}(\omega)\, \mathrm{e}^{\mathrm{i}\omega t}\, \mathrm{d}\omega \\ &= \frac{1}{\sqrt{2\pi}} \int_{-\infty}^{\infty} A_{\mathrm{ref}}(\omega) A(\omega)\, \mathrm{e}^{\mathrm{i}[\varphi_{\mathrm{ref}}(\omega)-\varphi(\omega)]}\, \mathrm{e}^{\mathrm{i}\omega t}\, \mathrm{d}\omega. \end{aligned} \tag{2.27}$$

Hence, all information is contained in, e.g., the positive temporal part of $S(t)$ and similarly to the spectral electric field definition of Eq. (2.9), the quantity

$$S^{+}(t) = \tilde{S}(t-\tau). \tag{2.28}$$

can be defined and isolated with a filter function.

The width of $S^{+}(t)$ depends on two things [cf. Eq. (2.27)]. First, it depends on the spectra $A_{\mathrm{ref}}(\omega)$ and $A(\omega)$ of both pulses, i.e., the bandwidth-limited pulse durations. Here, it should be noted that the reference pulse must have at least the same bandwidth as the signal pulse in order to obtain interference fringes over the whole spectral range of interest. Second, the width of $S^{+}(t)$ depends on the spectral difference phase between both pulses, i.e., the range of oscillation frequencies contained in the spectral interferogram (cf. inset of Fig. 2.1). In order to apply a filter function and isolate $S^{+}(t)$ from its counterpart the separation τ of the pulses has to be (much) larger than the width of $S^{+}(t)$. Furthermore, if the signal intensity $I(\omega)$ is not subtracted from the interference pattern [Eq. (2.23)], it will show up as a DC component in $S(t)$, which requests an even higher threshold for τ. On the other hand, a large separation τ yields closely spaced fringes in the interferogram that eventually cannot be resolved by the spectrometer (Nyquist limit). Therefore, τ has to be chosen according to the experimental parameters for good results (see also Section 3.3).

The possibility of isolating $S^{+}(t)$ is the condition that allows to transfer the cosine function of Eq. (2.25) into a complex-valued relation, the Fourier transform of $S^{+}(t)$:

$$\begin{aligned} S^{+}(\omega) &= \frac{1}{\sqrt{2\pi}} \int_{-\infty}^{\infty} \tilde{S}(t-\tau)\, \mathrm{e}^{-\mathrm{i}\omega t}\, \mathrm{d}t \\ &= \left[E^{+}_{\mathrm{ref}}(\omega)\right]^{*} E^{+}(\omega)\, \mathrm{e}^{-\mathrm{i}\omega\tau} \\ &= \sqrt{I_{\mathrm{ref}}(\omega) I(\omega)}\, \mathrm{e}^{\mathrm{i}[\varphi_{\mathrm{ref}}(\omega)-\varphi(\omega)-\omega\tau]}\,. \end{aligned} \tag{2.29}$$

The difference phase is now directly given by

$$\varphi_{\mathrm{diff}}(\omega) = \varphi(\omega) - \varphi_{\mathrm{ref}}(\omega) = -\arg\left\{S^{+}(\omega)\right\} - \omega\tau. \tag{2.30}$$

As mentioned at the beginning of this section, the phase of the reference pulse $\varphi_{\mathrm{ref}}(\omega)$ has to be measured additionally with a self-referencing technique if the phase of the signal pulse is to be determined. Furthermore, if the temporal separation τ is not known, it can be deduced by the linear coefficient of a polynomial fit of $\arg\{S^{+}(\omega)\}$. However, as discussed in Section 3.3, for a detailed analysis of the temporal separation other techniques are better suited.

2.3 Confocal Microscopy

The experimental method used in this work to launch optical excitations on nanostructures and collect their emission is called confocal microscopy. In the current section, the confocal principle is described with a ray-tracing model. Since this model is not sufficient to explain details of image formation in microscopes, the angular spectrum representation of optical fields is introduced subsequently. With the help of the angular spectrum framework, spatial resolution in microscopes and focusing of fields is discussed. Parts of this section are based on [Hecht06].

Ray-Tracing Model of Confocal Microscopy

Lenses and combinations of lenses have been used for a long time for imaging purposes, e.g., to magnify distant objects like stars (using telescopes) and to enlarge small structures in the vicinity, such as biological cells (using microscopes). In the so-called two-stage microscope, consisting of two focusing lenses, the first lens (called objective) produces an inverted real image of the object, which is then further magnified by the second lens (called eyepiece or ocular) [Träger12]. Because of various aberrations that occur upon imaging (chromatic and spherical aberration, coma, astigmatism, field curvature, and distortion) a microscope objective usually consists of multiple lenses, so that the combination of them corrects most of the aberrations, even for large acceptance angles θ (cf. Fig. 2.2a) [Demtröder04].

In modern microscopes the objectives are corrected for infinity, i.e., an almost aberration free image is produced at an infinite distance from the objective if the object is placed exactly in the focal plane. Therefore, a so-called tube lens has to be used to produce a real image, e.g., on a detector. Only the combination of an objective and an appropriate tube lens positioned within a compatible distance produces an image magnified by the factor imprinted on the objective. The magnification of such a system can simply be calculated as [Enderlein00, Hecht06]

$$M = f_{\mathrm{tl}}/f_{\mathrm{obj}}, \tag{2.31}$$

where f_{tl} and f_{obj} denote the focal length of the tube lens and objective, respectively. These infinity-corrected optical systems have the advantage that auxiliary components, such as beam splitters, deflection mirrors, or polarizers, can be introduced "into the parallel optical beam path between objective and tube lens with only a minimal effect on focus and aberration corrections." [Nicon13]

A ray-tracing model of such an infinity optical system is illustrated in Fig. 2.2a. Radiating ideal point sources (circle, star, rectangle) are imaged via an objective, a 45° deflection mirror and a tube lens to a detector. In wide-field microscopes the entire sample area is illuminated and the detector records the complete image at once. Contrary, in confocal microscopy a locally restricted volume around the objective's focal spot is excited only, as indicated by the light-gray ellipse in Fig. 2.2a (a way to achieve this is discussed later), and a sensitive detector without spatial resolution is used. The detector can, e.g., be an avalanche photo diode (APD) that records only intensities. Then, an image of the sample can be obtained, e.g., by raster scanning the sample plane through the excitation volume. In this case, a pinhole positioned confocal to the excitation volume, i.e., in the conjugated sample plane

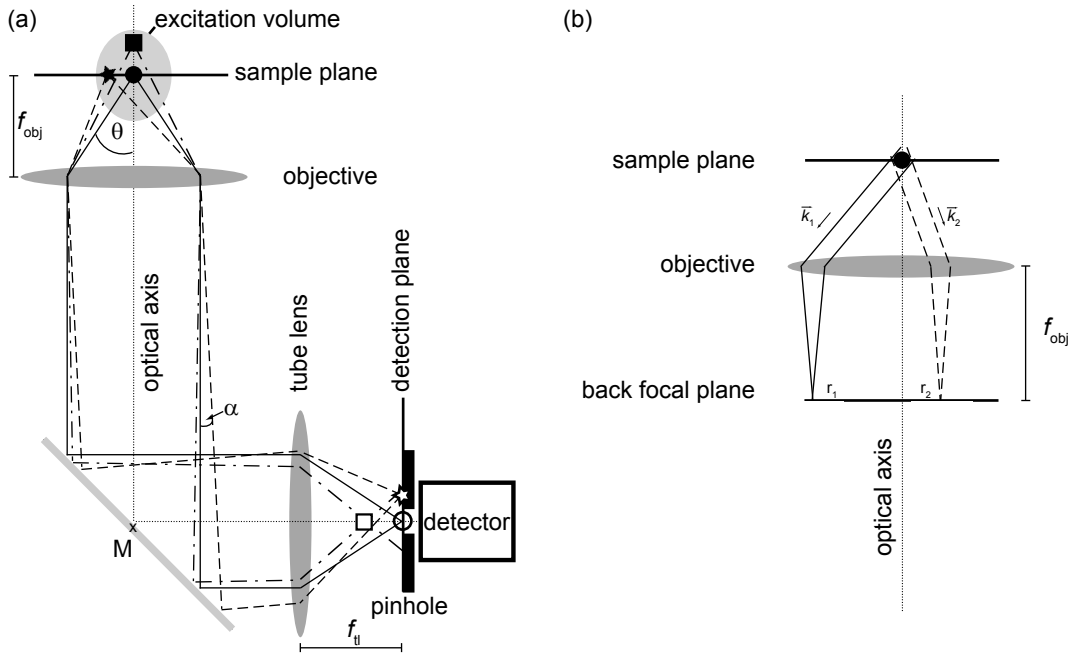

Figure 2.2: (a) Ray-tracing model of the confocal-microscopy principle. The radiation of ideal point sources (circle, star, rectangle) is collected by the objective within its opening angle 2θ and transformed into parallel rays that are redirected towards the tube lens via a 45° deflection mirror. Since the rays originating from off-axis positions (star, dashed lines) propagate at an angle α with respect to the optical axis (dotted line), the pinhole in the detection plane rejects them (open star). Intensity from out-of-sample-plane positions (rectangle) is reduced because the image focus is not in the detection plane (open rectangle). Figure based on [Hecht06]. (b) Principle of Fourier Imaging (conoscopy). Emission directions $\vec{k}_i$ of a point source (circle) are encoded in positions r_i in the back focal plane of the objective.

(detection plane in Fig. 2.2a) and on the optical axis, can be used to increase image sharpness by reducing unwanted intensity from out-of-focal-spot positions, as explained in the following.

An ideal point source in the focal plane and on the optical axis of the objective is indicated in Fig. 2.2a as a circle. The objective collects all radiation within its opening angle 2θ and transforms it into a collimated beam that propagates parallel to the optical axis (solid lines). This beam is consecutively focused by the tube lens into the image plane on the optical axis (open circle) where a pinhole is positioned. Thus, all intensity is collected by the detector behind the pinhole.

On the other hand, the collimated beam of a point source in the focal plane but slightly displaced from the optical axis (star) propagates at an angle α with respect to the optical axis (dashed lines). Note that α is determined by the focal length f_{obj} and the displacement via simple trigonometry, see also Section 3.4. Consequently, the tube lens focuses the beam next to the pinhole in the image plane (open star) and, thus, light emerging from the star's position in the sample plane does not reach the detector.

Suppression of recorded intensity from a point source located on the optical axis but not in the focal plane of the objective is also achieved with the confocal concept. Light from such a point (rectangle) is not collimated by the objective (dashed-dotted lines). In the case shown

here, the beam is slightly converging and is focused in front of the detection plane (open rectangle). Hence, the beam is partly blocked by the pinhole and the recorded intensity of that position is reduced.

In summary, the confocal principle improves image sharpness for raster scanning microscopes that use detectors without spatial resolution and locally restricted illumination.

An interesting aspect of lenses that is relevant for confocal microscopy and the next subsection can also be deduced from Fig. 2.2a: Lenses are sometimes referred to as Fourier transformers between real ($\vec{r}$) and reciprocal ($\vec{k}$) space. In the ray optics approximation, displacements in the focal plane with respect to the optical axis ($\vec{r}$) are encoded into propagation directions of collimated beams, i.e., $\vec{k}$-vectors, and vice versa. Hence, also the deflection mirror can be used to raster scan the sample plane: A tilt of $\alpha/2$ with M as center of rotation redirects emission from the position denoted with a star towards the pinhole. This concept is used in the spectral-interference microscope (Chapter 3). In this context it is interesting to note that the field of view, i.e., the lateral size of the sample plane that is correctly imaged into the detection plane, is, in principle, given by the objective (design). However, as can be anticipated from Fig. 2.2a, the size of the deflection mirror can limit the field of view further since beams originating from point sources displaced far from the optical axis are clipped.

Another application of a lens acting as (inverse) Fourier transformer is called Fourier imaging or conoscopy [Curto10] and is illustrated in Fig. 2.2b. Here, it is assumed that a point source on the optical axis (circle) radiates only in two different directions ($\vec{k_1}$ and $\vec{k_2}$), which is illustrated by solid and dashed collimated beams, respectively. After passing the lens, the direction of each collimated beam is encoded in a specific position r_i, now in the image-sided back focal plane of the objective. Note that, in contrast to the object-sided focal plane, the back focal plane is usually located within the housing of an infinity corrected objective. However, by imaging this back focal plane onto a detector, the angular emission of, e.g., single molecules [Lieb04], propagating plasmons [Grandidier08] or optical antennas [Curto10] can be characterized.

Angular Spectrum Representation of Optical Fields

In the ray-tracing model used above, a collimated optical beam is described by parallel rays. This model is sufficient to discuss the confocal principle. However, in contrast to reality, focal sizes in this model are infinitesimal small. Therefore, the model lacks an explanation for, e.g., the pinhole size that has to be chosen in a given microscope system. In order to tackle this question and provide an overview of basics in high-resolution imaging and strong focusing, the angular spectrum representation is briefly introduced in the following. This is done without presenting a detailed treatment or all intriguing facets of this concept.

"The angular spectrum representation is a mathematical technique to describe optical fields in homogeneous media." [Hecht06] The idea of the technique is to Fourier transform the known electric field $\vec{E}(\vec{r})$ at a given point $\vec{r} = (x, y, z)$ in a two-dimensional plane transverse to an arbitrary axis z. In analogy to the description of femtosecond pulses in the frequency domain rather than in the time domain (cf. Section 2.1), the resulting Fourier spectrum

$$\tilde{\vec{E}}(k_x, k_y; z) = \frac{1}{4\pi^2} \iint_{-\infty}^{+\infty} \vec{E}(x, y, z)\, \mathrm{e}^{-\mathrm{i}[k_x x + k_y y]}\, \mathrm{d}x\mathrm{d}y \tag{2.32}$$

is convenient to describe propagation of optical fields. Mathematically, the variables k_x and k_y are so-called spatial frequencies, or reciprocal coordinates, corresponding to the Cartesian transverse coordinates x and y. According to the Fourier theory, high spatial frequencies correspond to small variations in real space. However, the spatial frequencies also determine the propagation direction of constituent waves via the wave vector $\vec{k} = (k_x, k_y, k_z)$, as shown in the following.

In principle, the transverse x–y plane located at $z = 0$ can be the sample plane of a microscope. Upon illumination, structural data of this plane is imprinted on the light field. For instance, the information of a tiny hole in an otherwise opaque sample is then contained in $\vec{E}(x, y, z = 0)$, as the field is only present within the hole. The Fourier spectrum of this field [Eq. (2.32)] evolves along the z axis [Hecht06]:

$$\tilde{\vec{E}}(k_x, k_y; z) = \tilde{\vec{E}}(k_x, k_y; 0)\, \mathrm{e}^{\pm \mathrm{i} k_z z}\,. \tag{2.33}$$

This can be shown by using the wave equation [Eq. (2.14)] and the definition

$$k_z \equiv \sqrt{(k^2 - k_x^2 - k_y^2)}, \qquad \text{with} \qquad \mathrm{Im}[k_z] \geq 0, \tag{2.34}$$

where k is defined via the dispersion relation [cf. Eq. (2.16)]. From Eq. (2.33), it can be deduced that the Fourier spectrum in an arbitrary plane (e.g., an image plane) located at z can be calculated from a simple multiplication of the Fourier spectrum at the known plane (e.g., the sample plane) at $z = 0$ with the so-called propagator in reciprocal space, $\mathrm{e}^{\pm \mathrm{i} k_z z}$. Here, the $\pm$-sign refers to wave propagation into the positive or negative z direction, respectively.

By applying the inverse Fourier transform to Eq. (2.32) and inserting Eq. (2.33), one arrives at the so-called angular spectrum representation:

$$\vec{E}(x, y, z) = \iint_{-\infty}^{+\infty} \tilde{\vec{E}}(k_x, k_y; 0)\, \mathrm{e}^{\mathrm{i}[k_x x + k_y y \pm k_z z]}\, \mathrm{d}k_x \mathrm{d}k_y. \tag{2.35}$$

For dielectric media without losses the dispersion relation [Eq. (2.16)] reduces to $k = (\omega/c)n$, with the real and positive refractive index n [cf. Eq. (2.2)]. Therefore, depending on the point in the k_x–k_y space, i.e., the reciprocal sample space, the wavenumber k_z can be either real or imaginary. Hence, the propagator in reciprocal space, $\mathrm{e}^{\pm \mathrm{i} k_z z}$, is an oscillatory or exponentially decaying function, respectively, and two different solutions of Eq. (2.35) exist:

$$\mathrm{e}^{\mathrm{i}[k_x x + k_y y]}\, \mathrm{e}^{\pm \mathrm{i}|k_z| z} \qquad \text{for} \qquad k_x^2 + k_y^2 \leq k^2, \quad \text{and} \tag{2.36}$$

$$\mathrm{e}^{\mathrm{i}[k_x x + k_y y]}\, \mathrm{e}^{-|k_z||z|} \qquad \text{for} \qquad k_x^2 + k_y^2 > k^2. \tag{2.37}$$

Thus, in the angular spectrum representation, a superposition of plane [Eq. (2.36)] and evanescent [Eq. (2.37)] waves "propagate" the Fourier spectrum. Both kind of waves are solutions of Maxwell's equations. In the paraxial limit, where the wavevector $\vec{k} = (k_x, k_y, k_z)$ is almost parallel to the z axis and $k_x, k_y \ll k$, the angular spectrum representation becomes identical with the framework of Fourier optics [Hecht06].

It is interesting to discuss the different constituent waves of the angular spectrum representation. Plane waves that propagate along the z axis, with $k_z = k$, show no transverse

oscillations ($k_x^2 + k_y^2 = 0$) and extend infinitely in the x–y plane. Thus, no variation of $\vec{E}(x, y, z = 0)$ can be encoded into them and they carry no information about any structural data in the x–y sample plane. On the other hand, plane waves that propagate perpendicular to the z axis naturally have large oscillations in this transverse plane ($k_x^2 + k_y^2 = k^2$) and no dependence on the z coordinate, i.e., they extend infinitely along this coordinate. Due to the large oscillations within the sample plane, variations of $\vec{E}(x, y, z = 0)$ are encoded into these waves and they carry information about structural data in the sample plane. Evanescent waves [cf. Eq. (2.37)] cover even higher spatial frequencies in the transverse plane they are propagating in, i.e., they carry highly resolved information about spatial variations. However, this is at the expense of exponentially decaying fields along the z direction.

Thus, the propagator in reciprocal space is a low pass filter: Spatial frequencies $k_x^2 + k_y^2 > k^2$ of the original field in the transverse sample plane get lost upon propagation since they are exponentially damped out. Furthermore, each aperture in an imaging system, e.g., a lens, is also a low pass filter that rejects spatial frequencies corresponding to propagation directions of uncaptured plane waves. Therefore, they cannot contribute to image formation. For instance, for the example with a tiny hole in an otherwise opaque sample (cf. above), capturing only the plane wave that propagates along the z axis results in an image that shows a completely transparent sample, i.e., no structural data of the sample plane is obtained.

Spatial Resolution

As a direct consequence of the spatial frequency filtering explained above, even the image of a point source has a finite size. Mathematically, such a source is described by a delta function in space and is represented by an infinite bandwidth of spatial frequencies k_x, k_y. In a confocal microscope, the evanescent components [Eq. (2.37)] are always lost. For the propagating components [Eq. (2.36)] an objective can only capture plane waves within its opening angle 2θ, cf. Fig. 2.2a. A mathematical treatment in the angular spectrum framework shows that an electric dipole, which is a physical representation of a point source, situated in the sample plane of a confocal microscope and oriented within the transverse plane is imaged to an intensity distribution that is, along a transverse axis in the image plane, proportional to an Airy pattern [Hecht06]. The Airy pattern is well-known from diffraction problems and sketched in Fig. 2.3 in the context of focusing (cf. next subsection).

The function that maps a point source from the sample plane to the image plane is also called point-spread function since it describes how a point source spreads out to a finite size upon imaging. The radial distance for which the point-spread function in the image plane becomes zero the first time is usually defined as the Airy disk radius Δx_{image}. This radial distance naturally depends on the magnification M [cf. Eq. (2.31)] of the microscope [Hecht06]:

$$\Delta x_{\text{image}} = 0.6098 \frac{M \lambda_0}{\text{NA}}, \quad \text{NA} = n \sin(\theta). \tag{2.38}$$

Here, λ_0 is the vacuum wavelength and n is the refractive index in the object space. Furthermore, the so-called numerical aperture (NA) of the objective was introduced.

From Eq. (2.38) it can be deduced that, even for a magnification of $M = 1$, the image size of a point source is finite and depends on the effective wavelength λ_0/n of the light and the

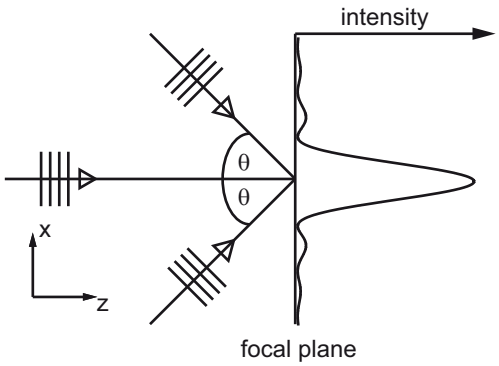

Figure 2.3: Schematic of focusing. Several plane waves impinge under different angles θ with respect to the z axis on the transverse focal plane. Constructive and destructive interference in this plane yields a spatially restricted intensity distribution in form of an Airy pattern. Figure adapted from [Rewitz09].

opening angle of the objective. This allows a sensible determination of the minimal pinhole size in a confocal microscope: Choosing the pinhole radius according to Eq. (2.38) ensures that almost all the intensity of a single dipole is detected.

In order to estimate the maximal sensible pinhole size, a criterion for the distinction of the images from two closely spaced point sources in the sample plane is needed. Different approaches exist to formulate such a spatial resolution criterion. They all have in common that the point-spread functions of two point sources are examined, but differ in details, such as the orientation and relative intensities of the two dipoles [Hecht06]. However, by requesting that the maximum of one point-spread function coincides with the first minimum of the other one, and using Eq. (2.38) one arrives at the Abbe criterion for the minimal resolvable separation Δx_{object} of two point sources in the sample plane:

$$\Delta x_{\text{object}} = 0.6098 \frac{\lambda_0}{n \sin(\theta)}. \tag{2.39}$$

Therefore, the confocal pinhole radius chosen above is also a sensible maximal radius since it corresponds to the resolution limit of the optical system. To enhance the resolution of an optical system for a given vacuum wavelength immersion-oil or water between the cover slip and the objective can be used to increase n above the vacuum level of 1. In this case, the objective corrections are optimized for a certain cover slip thickness, i.e., the sample plane (cf. Fig. 2.2a) is located exactly at the air-sided interface of the cover slip.

An even more optimistic formula for the resolution limit results from the simple argument that the entire spectrum of spatial frequencies within the numerical aperture of the objective contributes to the image formation [Hecht06]: $\Delta x_{\text{object}} = \frac{\lambda_0}{\pi \text{NA}}$. Going beyond this limit requires to sample higher spatial frequencies, also those associated with evanescent waves. This is possible with near-field optical microscopes. A comprehensive discussion of this technique can be found in [Hecht06].

Diffraction-Limited Focusing

An infinity corrected objective in a confocal microscope is often also used to focus excitation light into the sample plane in order to realize locally restricted excitation (cf. Fig. 2.2a, excitation volume). The principle of focusing can be seen as the inverse problem to the one discussed so far. In Fig. 2.3 a two-dimensional situation is sketched. Now, the interference of

propagating plane waves with different in-plane components $k_x = k \sin\theta$ but equal intensities yields a distribution proportional to the Airy pattern. When using high-NA objectives, a linearly polarized and collimated excitation beam can be focused down to this intensity distribution and a focal size according to Eq. (2.39) can be defined [Hecht06]. However, the spot will be elongated in the direction of polarization. In order to reach this so-called diffraction-limited focal size, the back aperture of the objective has to be overfilled by the collimated beam, i.e., the beam diameter has to be larger than the diameter of the back aperture. This ensures that all wave vectors $\vec{k}$ allowed by the numerical aperture are present with (ideally) similar intensity.

2.4 Propagating Optical Near Fields

In the last section, evanescent waves were mentioned as solutions of Maxwell's equations and used in the angular spectrum representation. In homogeneous media these optical fields do not propagate but decay exponentially away from the source and are, therefore, often called near fields. However, propagating optical near fields do exist. They "are electromagnetic excitations propagating at the interface between a dielectric and a conductor, evanescently confined in the perpendicular direction." [Maier07] Since they originate from the coupling of electromagnetic fields in the dielectric to oscillations of the conductor's electron plasma, they are also called surface plasmon polaritons (SPPs) or simply plasmons.

Starting with the wave equation, this section shows that plasmons are special solutions, i.e. modes, of the planar interface problem (Section 2.4.1) and that important characteristics can be deduced on this basis. Subsequently, more complex geometries such as multilayer structures (Section 2.4.2) and nanowires (Section 2.4.3), which form the basis of the nanostructures investigated in Chapters 4 and 5, are described. The discussion closes with an overview of possible excitation schemes (Section 2.4.4) and follows [Maier07], [Han13], and [Hecht06].

2.4.1 Electromagnetic Waves at a Planar Interface

Basic Equations and Discussion of Field Characteristics

In Section 2.1 the wave equation in the frequency domain [Eq. (2.14)] was introduced as the central equation that describes the propagation of monochromatic electric fields in a linear, homogeneous, isotropic, and nonmagnetic medium in the absence of any external charges or current densities. Now, the fields at an interface between two different homogeneous media are discussed. Consequently, the permittivity depends on the space coordinate $\vec{r}$. By defining $k_0 = \frac{\omega}{c} = \frac{2\pi}{\lambda_0}$ as magnitude of the wave vector in vacuum (λ_0 is the wavelength of light in vacuum), the wave equation simplifies to the homogeneous Helmholtz equation

$$\nabla^2 \vec{E}(\vec{r},\omega) + k_0^2 \varepsilon(\vec{r},\omega)\vec{E}(\vec{r},\omega) = 0. \tag{2.40}$$

For the next steps, it is instructive to proceed with a two-dimensional geometry, in which the waves propagate in x direction and the dielectric constant only depends on the z coordinate, i.e., $\varepsilon(\vec{r}) = \varepsilon(z)$ and $\partial/\partial y = 0$. The propagating waves can then be written

as $\vec{E}(x,y,z) = \vec{E}(z)e^{ik_{\mathrm{SPP}}x}$, where k_{SPP} is the propagation constant of the plasmons, i.e., the projection of the wave vector onto the propagation direction. With these assumptions, a system of equations for the electric and magnetic field components can be derived from the Helmholtz equation using Maxwell's curl equations [Maier07]. There exist two sets of self-consistent solutions with different polarization properties: For TM (transverse magnetic) modes only E_x, E_z and H_y are non-vanishing, whereas for TE (transverse electric) modes only H_x, H_z and E_y are nonzero. In the following, expressions for the electric field components of the TM modes are given [Maier07]:

$$E_x = -i\frac{1}{\omega\varepsilon_0\varepsilon}\frac{\partial H_y}{\partial z} \tag{2.41}$$

$$E_z = -\frac{k_{\mathrm{SPP}}}{\omega\varepsilon_0\varepsilon}H_y. \tag{2.42}$$

Furthermore, the wave equation of the TM mode's magnetic component reads [Maier07]

$$\frac{\partial^2 H_y}{\partial z^2} + (k_0^2\varepsilon - k_{\mathrm{SPP}}^2)H_y = 0. \tag{2.43}$$

With these formulas at hand, one can now look at the single interface problem between a non-absorbing dielectric and a metal, as sketched in Fig. 2.4a. The half space for $z > 0$ (light gray) is described by a positive real-valued dielectric function $\varepsilon_{\mathrm{d}}(\omega)$. The conducting half space for $z < 0$ (dark gray) is modeled with a permittivity function $\varepsilon_{\mathrm{m}}(\omega)$. Here, it should be noted that the metallic character requires a negative real part of the complex permittivity, i.e., $\mathrm{Re}[\varepsilon_{\mathrm{m}}(\omega)] < 0$. Now, by assuming solutions confined to the interface, i.e., with evanescent decay in the direction normal to the interface ($\propto \mathrm{e}^{-k_z z}$), the TM modes in both half spaces can be written as [Maier07]

$$H_y(z>0) = A_{\mathrm{d}}\,\mathrm{e}^{\mathrm{i}k_{\mathrm{SPP}}x}\,\mathrm{e}^{-k_{\mathrm{d}}z} \tag{2.44}$$

$$E_x(z>0) = \mathrm{i}A_{\mathrm{d}}\frac{k_{\mathrm{d}}}{\omega\varepsilon_0\varepsilon_{\mathrm{d}}}\,\mathrm{e}^{\mathrm{i}k_{\mathrm{SPP}}x}\,\mathrm{e}^{-k_{\mathrm{d}}z} \tag{2.45}$$

$$E_z(z>0) = -A_{\mathrm{d}}\frac{k_{\mathrm{SPP}}}{\omega\varepsilon_0\varepsilon_{\mathrm{d}}}\,\mathrm{e}^{\mathrm{i}k_{\mathrm{SPP}}x}\,\mathrm{e}^{-k_{\mathrm{d}}z}, \tag{2.46}$$

and

$$H_y(z<0) = A_{\mathrm{m}}\,\mathrm{e}^{\mathrm{i}k_{\mathrm{SPP}}x}\,\mathrm{e}^{k_{\mathrm{m}}z} \tag{2.47}$$

$$E_x(z<0) = -\mathrm{i}A_{\mathrm{m}}\frac{k_{\mathrm{m}}}{\omega\varepsilon_0\varepsilon_{\mathrm{m}}}\,\mathrm{e}^{\mathrm{i}k_{\mathrm{SPP}}x}\,\mathrm{e}^{k_{\mathrm{m}}z} \tag{2.48}$$

$$E_z(z<0) = -A_{\mathrm{m}}\frac{k_{\mathrm{SPP}}}{\omega\varepsilon_0\varepsilon_{\mathrm{m}}}\,\mathrm{e}^{\mathrm{i}k_{\mathrm{SPP}}x}\,\mathrm{e}^{k_{\mathrm{m}}z}\,. \tag{2.49}$$

In these equations A_{d} and A_{m} are proportionality factors. The component of the wave vector perpendicular to the interface (k_z) has been replaced by k_{d} and k_{m}, for the dielectric ($z > 0$) and metallic ($z < 0$) half space, respectively. It should be noted that the requested confinement perpendicular to the interface requires $\mathrm{Re}[k_{\mathrm{m}}]$, $\mathrm{Re}[k_{\mathrm{d}}] > 0$.

The solutions in both half spaces have to satisfy continuity conditions. The continuity of H_y requires $A_\mathrm{m} = A_\mathrm{d}$, whereas from the continuity of E_x it follows that

$$\frac{k_\mathrm{d}}{\varepsilon_\mathrm{d}} = -\frac{k_\mathrm{m}}{\varepsilon_\mathrm{m}}. \tag{2.50}$$

Furthermore, H_y has to fulfill the wave equation [Eq. (2.43)], yielding

$$k_\mathrm{m}^2 = k_\mathrm{SPP}^2 - k_0^2\varepsilon_\mathrm{m} \tag{2.51}$$
$$k_\mathrm{d}^2 = k_\mathrm{SPP}^2 - k_0^2\varepsilon_\mathrm{d}. \tag{2.52}$$

Combining the last three equations yields the dispersion relation of propagating optical near fields, i.e., a relation between the propagation constant (the momentum) and the angular frequency (the energy), an important equation for waves at the interface between a dielectric and metallic [Hecht06],

$$k_\mathrm{SPP} = k_0\sqrt{\frac{\varepsilon_\mathrm{m}\varepsilon_\mathrm{d}}{\varepsilon_\mathrm{m}+\varepsilon_\mathrm{d}}} = \frac{\omega}{c}\sqrt{\frac{\varepsilon_\mathrm{m}(\omega)\varepsilon_\mathrm{d}(\omega)}{\varepsilon_\mathrm{m}(\omega)+\varepsilon_\mathrm{d}(\omega)}}. \tag{2.53}$$

Since the demanded propagation along the interface requires that $\mathrm{Re}[k_\mathrm{SPP}] > 0$, it follows together with $\mathrm{Re}[k_\mathrm{m}]$, $\mathrm{Re}[k_\mathrm{d}] > 0$ that

$$\mathrm{Re}[\varepsilon_\mathrm{m}] < -\varepsilon_\mathrm{d} \tag{2.54}$$

has to hold, a condition that is satisfied for most metals and dielectrics in the long-wavelength part of the visible and in the infrared [Han13]. Furthermore, the fields can now be written as [Han13]

$$\vec{E}(z>0) = (E_x^0, 0, E_z^\mathrm{d})\cdot \mathrm{e}^{\mathrm{i}k_\mathrm{SPP}x}\exp(-z\sqrt{k_\mathrm{SPP}^2-\varepsilon_\mathrm{d}k_0^2}) \tag{2.55}$$
$$\vec{E}(z<0) = (E_x^0, 0, E_z^\mathrm{m})\cdot \mathrm{e}^{\mathrm{i}k_\mathrm{SPP}x}\exp(z\sqrt{k_\mathrm{SPP}^2-\varepsilon_\mathrm{m}k_0^2}), \tag{2.56}$$

where the normal and tangential field components are related to each other via

$$E_z^\mathrm{d} = \frac{\mathrm{i}k_\mathrm{SPP}}{\sqrt{k_\mathrm{SPP}^2-\varepsilon_\mathrm{d}k_0^2}}E_x^0, \tag{2.57}$$
$$E_z^\mathrm{m} = -\frac{\mathrm{i}k_\mathrm{SPP}}{\sqrt{k_\mathrm{SPP}^2-\varepsilon_\mathrm{m}k_0^2}}E_x^0, \quad \text{and} \tag{2.58}$$
$$E_x^0 = \frac{\mathrm{i}k_\mathrm{d}}{\omega\varepsilon_0\varepsilon_\mathrm{d}} = -\frac{\mathrm{i}k_\mathrm{m}}{\omega\varepsilon_0\varepsilon_\mathrm{m}}. \tag{2.59}$$

It is worthwhile to note that from connecting the solutions in each half space [Eqs. (2.44) to (2.49)] for the TE modes it follows that $A_\mathrm{m} = A_\mathrm{d} = 0$, i.e., at a planar single interface, only TM modes exist for surface plasmon polaritons [Maier07].

In Fig. 2.4b the sign-sensitive magnitudes $[|E_j|\cdot\mathrm{sign}(\mathrm{Re}\,[E_j])]$ of the two electric field components in each half space are plotted versus the distance z normal to the interface located at $z = 0$. Since some of the nanostructures investigated in this dissertation are

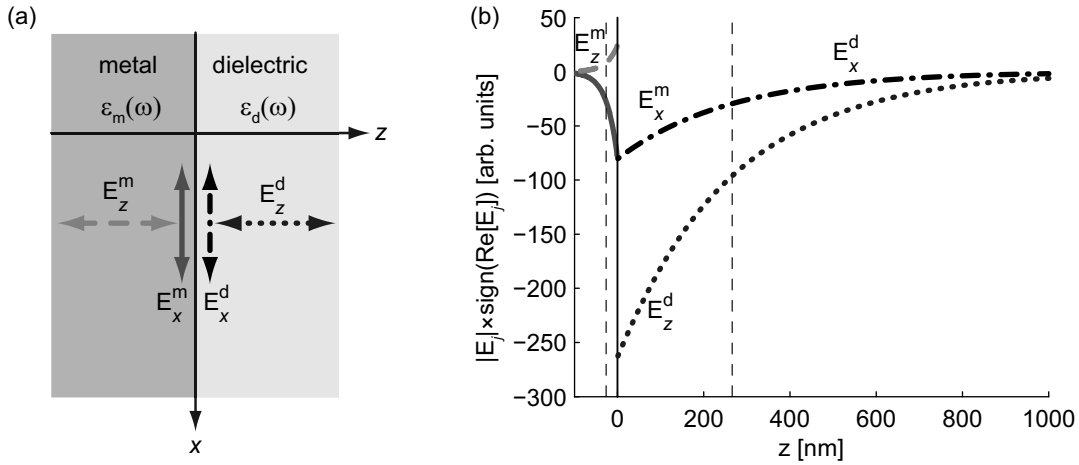

Figure 2.4: (a) Two-dimensional geometry of the interface between a metal (dark gray) and a dielectric (light gray). The double arrows indicate the orientation of different electric field components. (b) Shown are sign-sensitive magnitudes of the electric field components $[|E_j| \cdot \mathrm{sign}(\mathrm{Re}\,[E_j])]$ as a function of distance to a gold–silica interface (vertical line, $z = 0$) at the free space wavelength of $\lambda_0 = 800\,\mathrm{nm}$ ($\widehat{=}\ 1.55\,\mathrm{eV}\ \widehat{=}\ 374 \cdot 10^{12}\mathrm{Hz}\ \widehat{=}\ 2.35\,\mathrm{rad/fs}$). The values were calculated using Eqs. (2.55) and (2.56) with $\varepsilon_{\mathrm{Au}}(2.35\,\mathrm{rad/fs}) = -24.0 + 1.5\mathrm{i}$ [Johnson72] and $\varepsilon_{\mathrm{SiO_2}}(2.35\,\mathrm{rad/fs}) = 2.25$ [RI13]. As indicated in (a), the black-dotted, black dashed-dotted, light-gray dashed, and dark gray curves show the exponential decay of the field components E_z^{d}, E_x^{d}, E_z^{m}, and E_x^{m}, respectively. The field decay length normal to the interface is $L_z^{\mathrm{m}} = 1/\,\mathrm{Re}[k_{\mathrm{m}}] = 25\,\mathrm{nm}$ in gold and $L_z^{\mathrm{d}} = 1/\,\mathrm{Re}[k_{\mathrm{d}}] = 265\,\mathrm{nm}$ in silica (vertical dashed lines).

made of gold and are situated on microscope glass cover slips (Section 4.3 and Chapter 5), an interface between gold and fused silica is chosen as the exemplary system and the vacuum wavelength is $\lambda_0 = 800\,\mathrm{nm}$, which is the center wavelength of the excitation spectrum used in this work. The field components were calculated using Eqs. (2.55) and (2.56). A lot of information is already at hand in this representation. First of all, the energy is mostly located in the dielectric as can be inferred from the relative amplitudes for $z > 0$ (in the dielectric) and $z < 0$ (in the metal). Furthermore, in the dielectric half space, the normal component (E_z^{d}, black dotted) is dominating. Therefore, mostly a "photonic" TEM mode is present. On the other hand, in the metal the parallel component (E_x^{m}, dark gray) has the larger amplitude, implying that the collective electron (plasma) oscillation is mainly longitudinal, i.e., along the propagation direction. Thus, the combined surface plasmon polariton is a hybrid mode and any excitation light must provide the lateral electric field component. Therefore, only p-polarized light can be used for excitation at a planar interface (see also Section 2.4.4). Second, both components in one material follow the same exponential decay away from the interface. As indicated by the vertical dashed lines in Fig. 2.4b, the 1/e field decay length in the metal is $L_z^{\mathrm{m}} = 1/\,\mathrm{Re}[k_{\mathrm{m}}] = 25\,\mathrm{nm}$, whereas it is $L_z^{\mathrm{d}} = 1/\,\mathrm{Re}[k_{\mathrm{d}}] = 265\,\mathrm{nm}$ in the dielectric. Note that the intensity decay length is calculated as $L_z = 1/(2\,\mathrm{Re}[k])$. The fact that the decay length normal to the interface in the metal is shorter than in the dielectric is always true and is already visible in Eqs. (2.51) and (2.52) together with Eq. (2.54), assuming a positive dielectric constant ($\varepsilon_{\mathrm{d}} > 0$), i.e., $k_{\mathrm{m}} > k_{\mathrm{d}}$ always holds. However, the decay lengths and, thus, also the degree of field confinement depend on the propagation constant of the

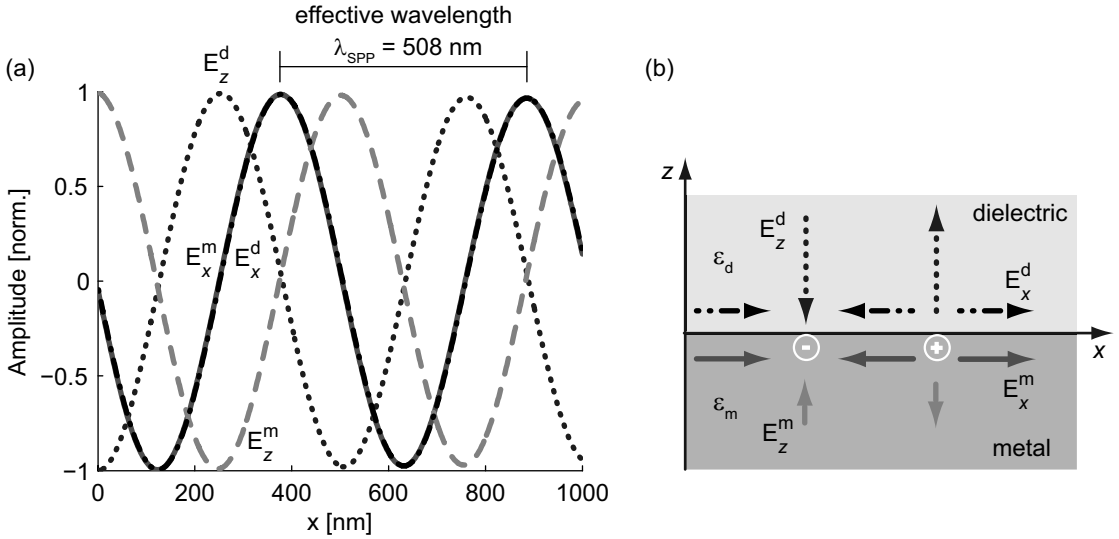

Figure 2.5: (a) Normalized amplitudes of the four field components as a function of lateral x coordinate, the propagation direction. The same geometry and calculation details as in Fig. 2.4 apply. The effective index of refraction of this geometry for the plasmon mode can be defined via $n_{\text{eff}} = k_{\text{SPP}}/k_0$ and is 1.57 in the present case (cf. with index of dielectric $n_{\text{Si}0_2} = 1.5$). (b) Sketch of the geometry with momentary field directions, relative amplitudes, and charge accumulation in the metal.

plasmon, as will be discussed later (Section 2.4.2).

Furthermore, Fig. 2.4b shows that the z components in each half space point into opposite directions. Figure 2.5a shows the normalized amplitudes in planes 10 nm away from the interface as a function of lateral x direction. From the black-dotted (E_z^{d}) and light-gray dashed (E_z^{m}) curves it can be deduced that there is a phase shift of 180° between these two components. An oscillatory behavior, i.e., propagation along the interface, can be seen in all four components. The oscillation period, i.e., the effective wavelength, $\lambda_{\text{SPP}} = 2\pi/\,\text{Re}[k_{\text{SPP}}] = 508\,\text{nm}$ naturally is the same for all components. The comparison of this effective wavelength with the wavelength of light in silica ($\lambda_{\text{Si}0_2} = 533\,\text{nm}$) for the same vacuum wavelength ($\lambda_0 = 800\,\text{nm}$) illustrates the reduction for the plasmonic wave. In other words, the propagation constant for the plasmon is increased. From its definition [Eq. (2.53)] it can further be concluded that a change of each interface constituent—metal or dielectric—alter the propagation constant and thus characteristics of the propagating optical near field.

In Figure 2.5a, the black dashed-dotted (E_x^{d}) and dark gray (E_x^{m}) curves are overlayed, i.e., no dephasing of the longitudinal components appears (in the shown region). The phase difference between the longitudinal ($E_x^{\text{d,m}}$) and normal ($E_z^{\text{d,m}}$) components in each medium is ±90°, because the energy alternates between them. The plasmon amplitude propagation length for the shown case is $L_x = 1/\,\text{Im}[k_{\text{SPP}}] = 25\,\mu\text{m}$. Thus, no damping is visible for the propagation distance of 1000 nm. This propagation length is mainly determined by the (positive) imaginary part of the metal permittivity [cf. Eq. (2.53)] that is responsible for ohmic losses. Therefore, the loss mainly arises from the lateral electric field component in the metal (E_x^{m}). If non-ideal systems are treated, additional loss channels, e.g., radiative

losses via surface roughness, come into play.

Figure 2.5b combines all the information gathered so far into a sketch of momentary field directions and relative amplitudes at the interface. It also indicates that charges are accumulated in certain regions of the metal.

Dispersion Relation and Propagation Velocities

The discussed characteristics so far were for a single wavelength only, even though the dispersion relation that connects propagation constant and frequency [Eq. (2.53)] was already at hand. Usually, the refractive index of a dielectric, e.g., fused silica, is almost constant from the visible to the infrared region of the electromagnetic spectrum, whereas the permittivity of metals has a strong dependency on frequency and is, in the optical regime, governed by the response of free and bound electrons [Hecht06, Maier07]. However, for the discussion presented here both dependencies are included, i.e., the permittivities' real and imaginary parts of metals are modeled as explained in Appendix A.1 and for the dielectric function of fused silica the Sellmeier dispersion formula with appropriate coefficients is used [Bass95]. All data is calculated in a broad frequency range around the center frequency of the laser used in this work ($\omega_0 = 2.35\,\mathrm{rad/fs}$).

The dispersion relation for photons in vacuum reads $\omega = ck_0$ and, thus, is a straight line (often called light line in vacuum) in a plot of frequency versus the real part of the propagation constant (Fig. 2.6, black dotted). In a dielectric, $\omega = c(\varepsilon_\mathrm{d})^{-1/2}k$ holds and the dispersion relation has a smaller slope (Fig. 2.6, black dashed dotted). In the case of planar-interface plasmons the relation reads $\omega = c(\frac{\varepsilon_\mathrm{m}\varepsilon_\mathrm{d}}{\varepsilon_\mathrm{m}+\varepsilon_\mathrm{d}})^{-1/2}k_\mathrm{SPP}$ and is plotted for a gold–air (dark-gray dashed), a silver–air (light-gray dashed), a gold–silica (dark gray), and a silver–silica interface (light gray) in Fig. 2.6. From the comparison with the respective light lines (black dotted and black dashed dotted) it can be deduced that the already mentioned increase of propagation constant is true for the complete frequency range that is shown, with a tendency of higher increase towards higher frequencies. In other words, the propagation constant of a plasmon is always equal or larger than that of a photon in the adjacent dielectric [$k_\mathrm{SPP}(\omega) \geq k(\omega)$]. This has consequences for the confinement of energy to the interface (cf. Section 2.4.2) and for excitation schemes (cf. Section 2.4.4). However, the difference of propagation constants becomes smaller towards lower frequencies. This fact can be explained by the permittivity of the metals. Compared with the visible frequency region, the permittivity has an even larger negative real part at lower frequencies (cf. Fig. A.1). Therefore, metals behave more like ideal conductors in the low frequency region, i.e., the electromagnetic field hardly penetrates into the metal and, thus, scarcely couples to the conductor's electron plasma. Consequently, the modes are almost plane waves with $k_\mathrm{SPP}(\omega) = k(\omega)$ and extend infinitely into the dielectric half space, transverse to the propagation direction. This can be generalized: Whenever the dispersion relation of a plasmon approaches that of the light line, the plasmon mode is hardly confined to the surface and resembles a photonic mode. For other plasmonic waveguide structures this also happens for certain geometric parameters and must not be confused with a cut-off (cf. Sections 2.4.2 and 2.4.3). If a mode is cut off, the propagation constant is purely imaginary [Novotny94] and the mode does not propagate [cf. Eqs. (2.55) and (2.56)].

Other interesting properties of plasmons, in particular in the context of this work, can also

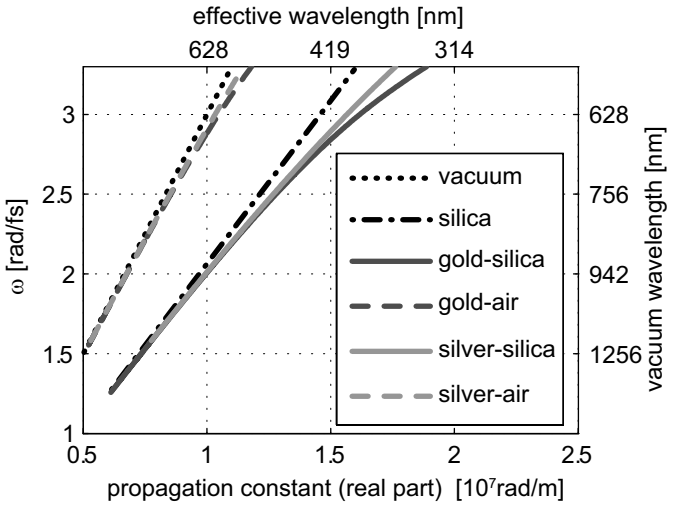

Figure 2.6: Computed dispersion relations using Eq. (2.53) for various planar interfaces. The light lines in vacuum (black dotted) and silica (black dashed dotted) are shown together with the curves of surface plasmons on a gold–air (dark-gray dashed), a silver–air (light-gray dashed), a gold–silica (dark gray), and a silver–silica interface (light gray). Depending on the curve, the lower abscissa labeling means $\mathrm{Re}[k_0]$, $\mathrm{Re}[k]$ or $\mathrm{Re}[k_{\mathrm{SPP}}]$.

be deduced from the dispersion relation: the phase and group velocities. The phase velocity describes the speed at which phase fronts of a single-frequency oscillation propagate in space and is defined as $v_{\mathrm{p}} \equiv \frac{\omega_0}{k_0}$ [Hecht02]. The propagation speed of a pulse, which is composed of several frequency components [cf. Eq. (2.8)], is given by the group velocity that is defined by $v_{\mathrm{g}} \equiv \frac{\mathrm{d}\omega}{\mathrm{d}k}|_{\omega_0}$ [Hecht02]. Hence, the group velocity is relevant for information transport and is given by the slope of the dispersion relation. For photons in a medium these relations can be rewritten as

$$v_{\mathrm{p}}^{\mathrm{Photon}} = \frac{c}{\sqrt{\varepsilon_{\mathrm{d}}}} = \frac{\omega}{k}, \tag{2.60}$$

$$v_{\mathrm{g}}^{\mathrm{Photon}} = \frac{\omega}{k} - ck\frac{\partial(\varepsilon_{\mathrm{d}}^{-1/2})}{\partial k}. \tag{2.61}$$

Thus, depending on the spectral characteristic of the dielectric permittivity, the group velocity can be slightly different than the phase velocity (but not larger than c).

For planar-interface plasmons, the velocities can be written as

$$v_{\mathrm{p}}^{\mathrm{Plasmon}} = \frac{c}{\sqrt{\frac{\varepsilon_{\mathrm{m}}\varepsilon_{\mathrm{d}}}{\varepsilon_{\mathrm{m}}+\varepsilon_{\mathrm{d}}}}} = \frac{\omega}{k_{\mathrm{SPP}}}, \tag{2.62}$$

$$v_{\mathrm{g}}^{\mathrm{Plasmon}} = \frac{\omega}{k_{\mathrm{SPP}}} + ck_{\mathrm{SPP}}\frac{\partial\left(\left(\frac{\varepsilon_{\mathrm{m}}\varepsilon_{\mathrm{d}}}{\varepsilon_{\mathrm{m}}+\varepsilon_{\mathrm{d}}}\right)^{-1/2}\right)}{\partial k}. \tag{2.63}$$

Since the propagation constant k_{SPP} of a plasmon is larger than that of a photon in the corresponding dielectric (k), the phase velocity of a plasmon is always smaller than that of a photon. For the group velocities the relation obviously depends on the spectral characteristics of both the metallic and dielectric permittivity. In systems more complex than a single planar interface the dispersion relation also becomes more complex and the group velocity depends on geometry details as well (see next Section). In general, however, the group velocity for plasmons is smaller than for photons in the adjacent dielectric, as can be deduced from the slopes of the curves in Fig. 2.6. For a vacuum wavelength of 800 nm, the group

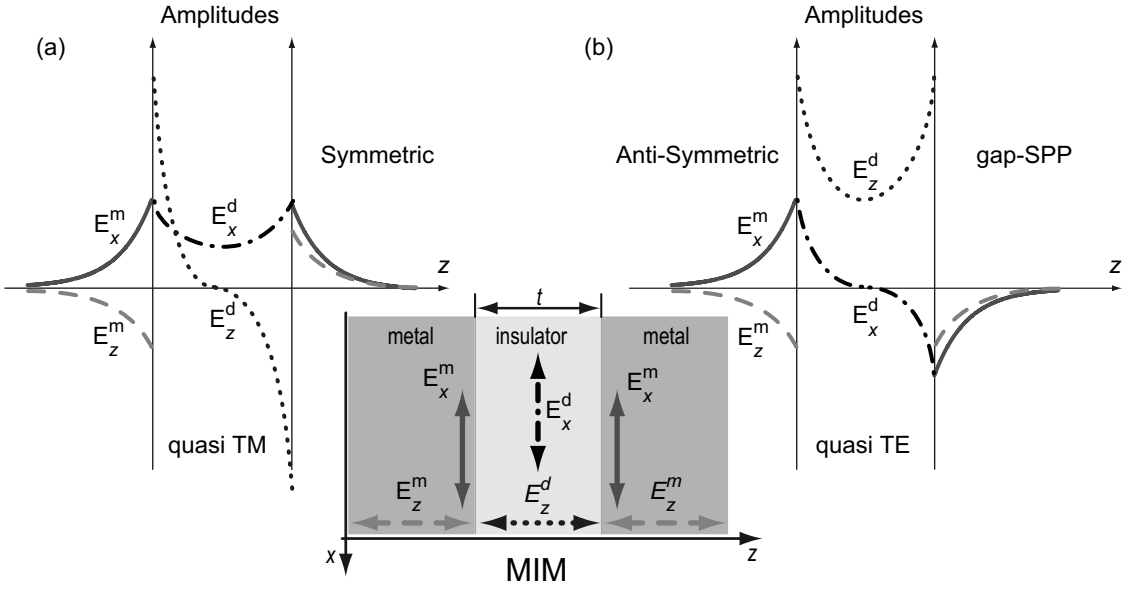

Figure 2.7: Schematic representation of electric field vector components' amplitudes for a MIM (metal–insulator–metal) double interface. (a) Shows the symmetric combination of the parallel component (E_x) and (b) illustrates the anti-symmetric combination. In the symmetric case the mode is called quasi-TM because the component of the electric field perpendicular to the interfaces (E_z) has a node in the dielectric gap (black dotted). For the anti-symmetric combination, the parallel component in the gap (black dashed dotted) has a node, whereas the perpendicular component (E_z) always points in the same direction within the dielectric gap (black dotted). Thus, the mode is called quasi-TE or gap-SPP. In the inset all components at the two interfaces are indicated together with the layer thickness t.

velocities of the plasmons at the gold–silica and silver–silica interfaces (slopes of dark-gray and light-gray curve, respectively) are $v_g^{\text{Plasmon,gold-silica}} = 1.73 \cdot 10^8 \text{m/s}$ and $v_g^{\text{Plasmon,silver-silica}} = 1.79 \cdot 10^8 \text{m/s}$, compared to the velocity of a photon in silica (slope of black dashed-dotted line) of $v_g^{\text{Photon,silica}} = 2.04 \cdot 10^8 \text{m/s}$.

2.4.2 Three-Layer Structures

After introducing basic field characteristics and the dispersion relation of plasmons at a single planar interface, the discussion now advances to symmetric structures with two planar interfaces. There are two possibilities for three layers: metal–insulator–metal (MIM) and insulator–metal–insulator (IMI) structures. If the separation t between the two interfaces is large, i.e., larger than the perpendicular decay lengths (L_z) in the respective materials, each interface supports an independent mode. However, if the separation becomes smaller (in the few-nanometer region), both identical modes couple and, just as for the combination of atomic orbitals in a molecule, a symmetric and anti-symmetric combination of the two independent modes is possible. As a result the propagation constants of the new modes are different.

In the following, symmetric structures and their mode combinations are discussed in detail. However, it should be noted that in this section only special cases of the fundamental bound

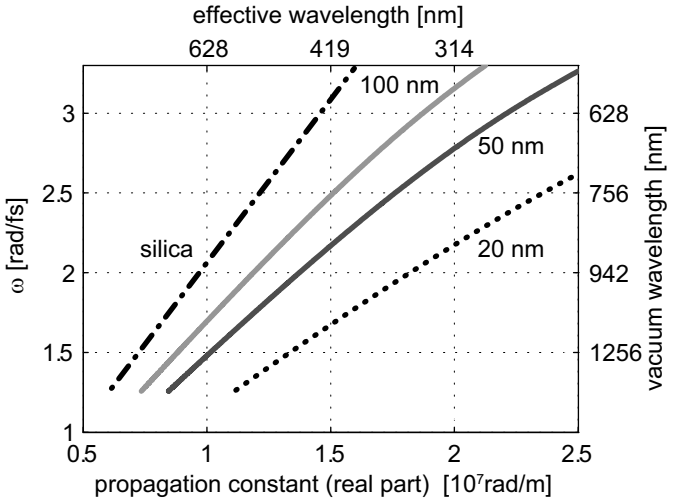

Figure 2.8: Computed MIM dispersion relations using Eq. (2.64). Shown is the light line in silica (black dashed dotted, cf. Fig. 2.6) together with the curves for a gap-SPP in a gold–silica–gold structure with layer thicknesses $t_1 = 100\,\text{nm}$ (light gray), $t_2 = 50\,\text{nm}$ (dark gray), and $t_3 = 20\,\text{nm}$ (black dotted).

modes are discussed. Other modes do exist. For instance leaky, i.e., radiating modes in IMI structures or oscillatory modes in MIM structures with a sufficient thickness of the dielectric core. Furthermore, different modes exist for non-symmetric structures, i.e., if the sub- and superstrate differ [Prade91]. If analytic solutions, e.g., for the dispersion relations, cannot be provided, simulations are often used to characterize modes or field distributions for a given geometry. Most commonly used algorithms, e.g., the finite-element or the finite-difference method (cf. Appendix A.1), find numerical solutions of Maxwell's equations by discretizing the simulation area into a fine mesh of unit cells [Chiang94].

Metal–Insulator–Metal (MIM)

Schematic representations of the field components' amplitudes in a MIM structure are shown in Figs. 2.7a and 2.7b for the symmetric and anti-symmetric combination of the parallel field components (E_x), respectively. The symmetric combination in E_x is anti-symmetric in E_z, i.e., the perpendicular field component has a node between the two interfaces (Fig. 2.7a, black dotted). Since the main electric field components in the dielectric are, therefore, along the interface and, hence, along the propagation direction, this combination is called the quasi-TM mode. On the other hand, the anti-symmetric combination in E_x features a node of the parallel field component (Fig. 2.7b, black dashed dotted). Thus, the perpendicular field component in the dielectric (E_z^{d}) always points in the same direction and this combination is called the quasi-TE mode. Interestingly, this mode has no cut-off for a vanishing core layer thickness ($\lim_{t\to 0}$), i.e., contrary to the quasi-TM mode, the quasi-TE mode propagates for all layer thicknesses [Prade91]. This mode is also called gap-SPP, because most of the fields are indeed located in the dielectric gap between both metal layers [Han13].

For the double interface it is possible to apply the same mathematics as for the single interface. However, only implicit expressions for the dispersion relations are possible [Maier07]. For the gap-SPP, an approximation of the dispersion relation can be given, where t is the dielectric layer thickness (cf. Fig. 2.7) [Han13]:

$$k_{\text{g-SPP}} \approx \frac{\omega}{c}\sqrt{\varepsilon_{\text{d}} + \frac{2\varepsilon_{\text{d}}\sqrt{\varepsilon_{\text{d}} - \varepsilon_{\text{m}}}}{(\omega/c)(-\varepsilon_{\text{m}})t}}. \tag{2.64}$$

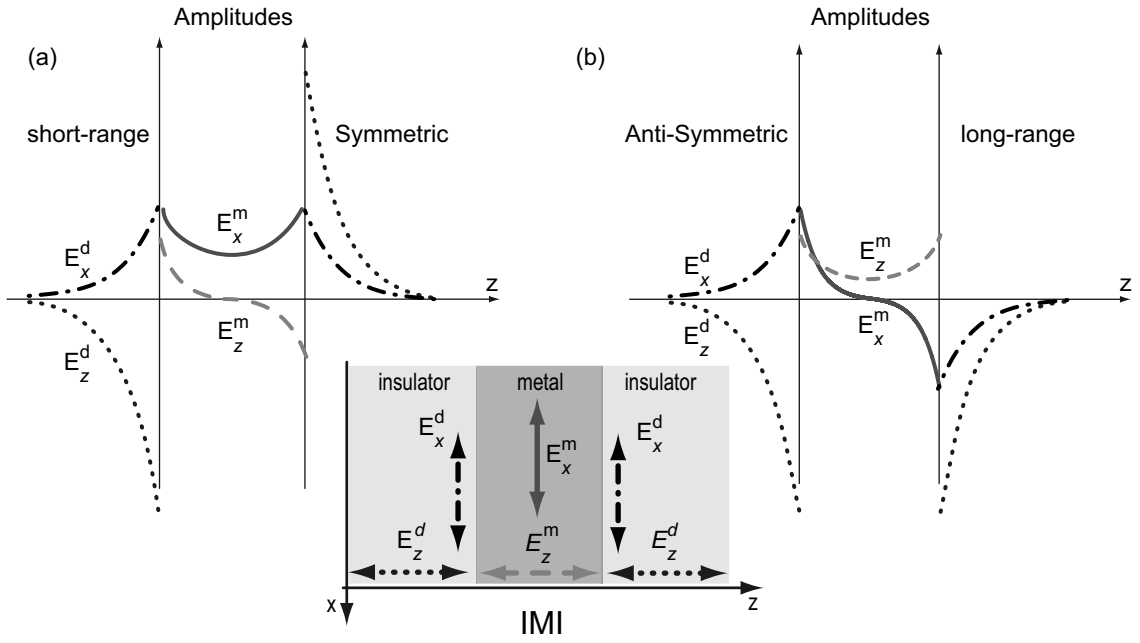

Figure 2.9: Schematic representation of electric field vector components' amplitudes for a IMI (insulator–metal–insulator) double interface. (a) Shows the symmetric combination of the parallel component (E_x) and (b) illustrates the anti-symmetric combination. In the symmetric case, the fields are tightly bound to the metal film, whereas an almost pure photonic mode exists for the anti-symmetric combination (parallel component in the metal has a node, fields are forced outside of the metal). In the inset all components at the two interfaces are indicated.

As already mentioned, the dependence of the plasmon propagation constant on the permittivities is more complex than for a single interface [cf. Eq. (2.53)]. In Fig. 2.8 the dispersion relations of gap-SPPs in a gold–silica–gold structure are plotted for layer thicknesses of $t_1 = 100\,\mathrm{nm}$ (light gray), $t_2 = 50\,\mathrm{nm}$ (dark gray) and $t_3 = 20\,\mathrm{nm}$ (black dotted) together with the light line in silica (black dashed dotted). The propagation constants of the g-SPP modes are larger than for a SPP on a gold–silica interface (cf. Fig. 2.6) and increase with decreasing silica-layer thickness. Indeed, $\lim_{t\to 0} \mathrm{Re}[k_{\mathrm{g-SPP}}] = \infty$ holds [Han13]. The increased plasmon propagation constant directly implies a high confinement of the fields, as can be seen by looking at Eqs. (2.51) and (2.52): The decay length away from the interfaces ($L_z^{\mathrm{m,d}} = 1/k_{\mathrm{m,d}}$) becomes smaller as the gap of the MIM structure decreases. Unfortunately, for the imaginary part of the propagation constant the same relation holds: $\lim_{t\to 0} \mathrm{Im}[k_{\mathrm{g-SPP}}] = \infty$ [Han13]. Therefore, high confinement always is accompanied by high losses ($L_x = 1/\,\mathrm{Im}[k_{\mathrm{SPP}}]$). This is a general trade-off in plasmonics, which might be solved with amplification techniques, see, e.g., [Liu13]. Regarding the group velocities, the same trend as before remains: The more the fields are confined in the transverse direction, i.e., the larger the propagation constant is, the slower is the lateral propagation, as can be inferred from the slopes of the curves in Fig. 2.8, e.g., at 800 nm vacuum wavelength.

Insulator–Metal–Insulator (IMI)

In the case of insulator–metal–insulator structures the same combinations of single-surface modes as in the MIM situation are possible. In the symmetric case (Fig. 2.9a) the new mode is called short-range SPP because the propagation constant increases infinitely in its real and imaginary part in the limit of very thin metal films [Maier07]. Therefore, the fields are tightly bound to the metal film. Again, the strong confinement is at the expense of high losses because the lateral field in the metal has no node (E_x^{m}, dark gray). This means ohmic damping of the longitudinal electron plasma oscillation is strong.

For the anti-symmetric combination (Fig. 2.9b), the mode is called long-range SPP: In the limit of very thin metal films the dispersion relation approaches the light line in the dielectric [Han13]. Thus, an almost pure photonic mode is formed that exhibits low losses but also poor confinement (cf. discussion of Fig. 2.6). In other words, the plasmon is forced out of the metal because the parallel component (E_x^{m}, dark gray) has a node between both interfaces. In the dielectric, the perpendicular components (E_z^{d}, black dotted) of both side of the metal film are in phase, which is close to the situation of a plane wave supported by the dielectric.

2.4.3 Single Nanowires

In the systems treated so far, the fields are only confined in the direction perpendicular to a two-dimensional interface. The propagation is discussed for one direction but can, in principle, take place in the complete plane. Hence, the systems are two-dimensional plasmonic waveguides. In order to allow propagation into one dimension only, one can think of rolling up a single metal–dielectric interface into a thin cylinder [Takahara97]. This results, e.g., in a metallic nanowire in a homogeneous dielectric surrounding.

For this system, it is sensible to solve the Helmholtz equation [Eq. (2.40)] in cylindrical coordinates. By obeying the periodicity in the azimuth angle, the solutions turn out to be proportional to modified Bessel functions and, hence, different orders of bound modes are possible. Furthermore, the solutions depend on the diameter of the nanowire [Novotny94, Takahara97]. The lowest order mode (TM_0, $m = 0$) is purely transverse-magnetic and implies lateral electron plasma oscillations along the nanowire axis. In Fig. 2.10a the simulated $m = 0$ mode profile is plotted for a silver nanowire with diameter $d = 100\,\mathrm{nm}$ embedded in fused silica, i.e., glass. The intensity has no azimuthal distribution and is bound to the nanowire as can be seen from its nonlinear decay away from the surface. Just as short-range SPPs in an IMI structure (cf. Section 2.4.2) the TM_0 nanowire mode shows no cut-off for decreasing diameters and the propagation constant diverges [Han13]. Hence, the nanowire is an almost ideal one-dimensional waveguide for the fundamental $m = 0$ mode. However, the propagation length is much shorter than for a planar-interface plasmon ($L = 1/\operatorname{Im}[k_{\mathrm{TM}_0}] = 6\,\mu\mathrm{m}$ at $\lambda_0 = 800\,\mathrm{nm}$ and $d = 100\,\mathrm{nm}$, cf. with $34\,\mu\mathrm{m}$ on a planar silver–silica surface) and decreases with smaller diameters since most of the power is then located in the metal.

Figures 2.10b,c show the simulated profiles of the modes $m = \pm 1$, respectively (nanowire in glass, $d = 100\,\mathrm{nm}$). The intensities have azimuthal distributions but still are symmetric in a plane through the center of the nanowire. In contrast to the $m = 0$ mode, higher order modes do show a cut-off for decreasing diameters. The cut-off diameter of each mode depends on the metal, the surrounding and the wavelength. As discussed in Section 2.4.1, the cut-off

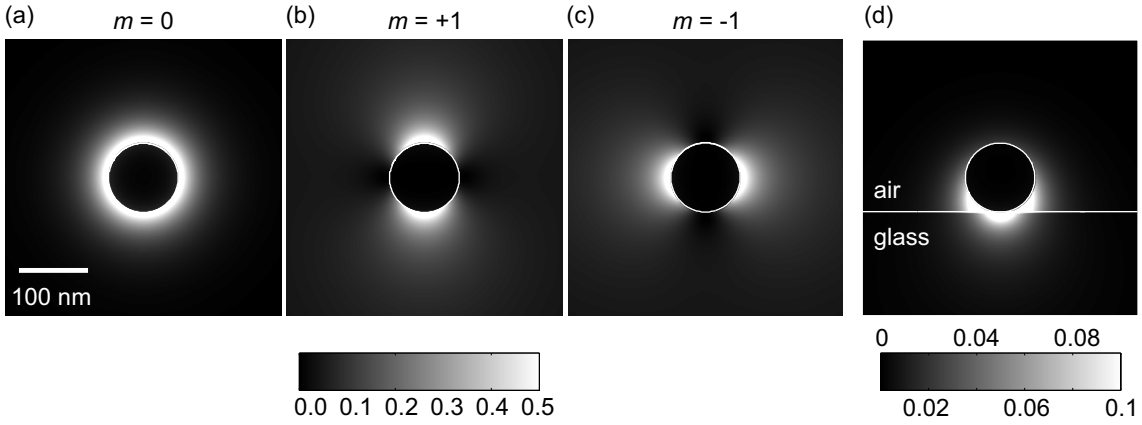

Figure 2.10: Simulated mode profiles (cf. Appendix A.1) for $\lambda_0 = 800\,\text{nm}$ on infinitely long silver nanowires (white circular outlines). Depicted is the near-field intensity ($|E_x|^2 + |E_y|^2 + |E_z|^2$). The $m = 0$, $m = +1$, and $m = -1$ modes of a $d = 100\,\text{nm}$ nanowire embedded in glass are shown in panels (a), (b), and (c) respectively. In panel (d) the nanowire is situated on top of a glass substrate. In this situation, the mode is mostly confined within the gap between the nanowire and the substrate and located in the substrate. Since the intensity in all panels is normalized to the mesh cell with the highest intensity, the different scaling further emphasize the strong localization of the mode in the case with substrate. Thanks to Gary Razinskas for the simulations.

criterion in simulations is also the transition from a complex-valued to a purely imaginary propagation constant. For silver nanowires embedded in a homogeneous glass surrounding and a vacuum wavelength of $\lambda_0 = 633\,\text{nm}$ the minimal diameters for the modes $m = \pm 1, \pm 2$ are ca. 50 nm and 400 nm, respectively [Zhang11]. For silver nanowires embedded in glass and $\lambda_0 = 800\,\text{nm}$ simulations show that the minimal diameters are ca. 100 nm and 620 nm, respectively.

For an inhomogeneous surrounding, e.g., a silver nanowire situated on a substrate, a configuration used in Section 4.2, symmetry breaking yields different modes such that, e.g., the lowest-order bound mode has quasi-TM character. Similar to the homogeneous case, higher order modes show a minimal cut-off diameter for the inhomogeneous surrounding. In the case of an air–glass interface, the dispersion relation of the fundamental mode crosses the light line in glass for decreasing frequencies (or increasing diameters) and, thus, evolves into a photonic mode (cf. discussion of Fig. 2.6). Therefore, the simulated profile of this mode for a vacuum wavelength of $\lambda_0 = 800\,\text{nm}$ is depicted in Fig. 2.10d for a nanowire with $d = 100\,\text{nm}$, the maximal diameter. Most of the intensity is confined within the gap between nanowire and substrate and located in the substrate. For the nanowire on a substrate the simple inverse relation between propagation constant and mode localization [cf. Eqs. (2.51) and (2.52)] breaks down: Despite of the strong localization (Fig. 2.10d), the real part of the propagation constant of the fundamental mode is smaller than the corresponding value for a nanowire in a homogeneous glass surrounding with less localization (Fig. 2.10a).

This can also be deduced from the dispersion relations shown in Fig. 2.11 by comparing the rectangles (glass substrate) and crosses (homogeneous glass surrounding). The dispersion relation of the nanowire on a substrate is situated in between the case of air (circles) and glass surrounding. Consequently, the same holds for the group velocities, i.e., the slopes of

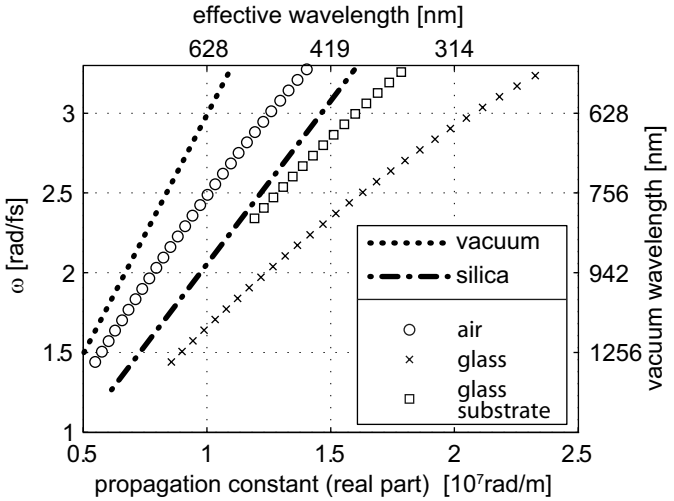

Figure 2.11: Simulated dispersion relations (Appendix A.1). The light lines in vacuum (dotted) and silica (dashed dotted) are shown together with lowest-order modes on silver nanowires ($d = 100\,\mathrm{nm}$) in different surroundings. Open circles, crosses, and rectangles represent data in air, glass, and on a glass substrate, respectively. Thanks to Gary Razinskas for the simulations.

dispersion relations. Experimental results on the environment-dependent group velocity are presented in Section 4.2. However, the group velocity also strongly depends on the nanowire diameter. As has been shown theoretically, the plasmon slows down upon propagation towards the tip of an tapered nanowire (adiabatically decreasing diameter) [Stockman04]. Experiments on the diameter dependent group velocity are also presented in Section 4.2.

As a last aspect in this section, it has to be noted that, here, characteristics of plasmonic modes on single nanowires are discussed for circular cross sections. However, most of the characteristics also hold for other shapes of the nanowire cross section (cf. Section 4.3.1). For instance, a rectangular nanowire on a substrate also features high field localization at the edges that are attached to the interface and the group velocity also depends on the cross-sectional area.

2.4.4 Excitation Schemes

Everything discussed so far in Section 2.4 is based on modes, i.e., solutions of the wave equation in the absence of excitation. As already mentioned, the propagation constant of a plasmon is always larger than that of a three-dimensional light beam in the respective dielectric medium (cf. Figs. 2.6, 2.8, and 2.11). Due to this mismatch of momentum, direct excitation of plasmons with light is usually not possible. However, some techniques that provide the lacking momentum exist and are discussed briefly in the following.

Prism and Grating Coupling for Two-Dimensional Propagation

For excitation of plasmons at the planar interface between a metal and a dielectric with low dielectric index the fact that light in a high-index dielectric always has a larger wave vector (cf. light lines in Figs. 2.6 and 2.11) can be exploited. The in-plane momentum of light in the high-index dielectric $k_x = k\sqrt{\varepsilon_\mathrm{d}}\sin\theta$, where θ is the angle to the surface normal under which the beam is impinging, can be matched to the plasmon momentum k_SPP by varying θ. In the planar-interface case, p-polarized light has to be used because a longitudinal electric field component along the propagation direction must be provided to drive the electron plasma oscillation of the fundamental mode (cf. Section 2.4.1). Usually a

prism in total internal reflection mode is used as high-index dielectric and depending on the details the configuration is named Otto or Kretschmann [Hecht06]. In both cases excitation of plasmons is detected via a dip in the reflectivity at angles above the critical angle θ_c of total internal reflection. However, plasmons that are excited using prism coupling are inherently leaky, i.e., upon propagation they also radiate to the far field via the same mechanism of momentum matching.

The in-plane momentum mismatch can also be overcome with the help of gratings. Additional momentum can be provided by a grating imprinted, e.g., in the metal surface. Depending on the lattice constant a, momentum matching takes place whenever $k_{\mathrm{SPP}} = k \sin\theta \pm m \cdot 2\pi/a$ holds, with m being an integer [Maier07]. Also, scattering defects on a surface, e.g., discontinuities of subwavelength size, can provide the missing momentum components. They can act as local couplers that can be addressed with focused light. The defects can also be produced on purpose, e.g., as lithographically designed protrusions in form of discs or ridges [Ditlbacher02] or as slit-like perforations in metal films [Schouten05]. However, for a single defect the excitation efficiency is usually quite low.

Mode Matching for One-Dimensional Propagation

A method closely related to the excitation of plasmons via defects on a surface is the launching of lateral guided modes in structures that have subwavelength transverse dimensions. For modes existing on metallic nanowires in a dielectric surrounding (cf. Section 2.4.3) local symmetry breaking at a nanowire end is sufficient to allow excitation with strongly focused light impinging normally to the nanowire axis [Han13]. In addition to the local symmetry breaking, two aspects play a role for this method. First, for high-NA objectives, the angular spread of incoming angles is quite large (cf. Section 2.3), which offers lateral propagation constants not available in unfocused or weakly focused beams. Second, the transverse subwavelength dimensional nanowire can also be regarded as a defect that provides large momentum components as well. In Chapter 3, Section 4.2, and Section 4.3.1 strongly focused light is used to excite propagating modes on nanowires. In these cases, the input polarization with respect to the nanowire [Zhang11] as well as the end facet shape of the nanowire [Li10] determine the excitation efficiencies of different modes. Typically, optimal excitation of the fundamental mode is obtained for a polarization parallel to the nanowire. This also implies maximum emission intensity at the far end of the nanowire [Li10].

Furthermore, optical antennas [Mühlschlegel05, Agio13] can provide a link between the field profile of the focused excitation beam and the modal profile of a waveguide structure, thereby enabling efficient launching of guided plasmons. In this case, the antenna impedance has to match the waveguide impedance to transfer power to a specific mode [Alù08, Huang09, Wen09], just as in classical transmission line theory. Optical antennas are used in Section 4.3.2 and Chapter 5 to enhance the coupling of high-NA focused laser light with so-called two-wires transmission lines.

3 Spectral-Interference Microscopy

After introducing some theoretical background on femtosecond laser pulses and propagating optical near fields as well as discussing experimental methods in the last chapter, the technique that was developed in this dissertation for characterizing plasmonic nanostructures is presented and explained in detail in the current chapter. The basic idea of the experimental design (Section 3.2) is to combine the two methods described in the previous chapter: confocal microscopy and spectral interferometry. To investigate propagating plasmons with this spectral-interference microscope a special kind of data acquisition and data evaluation is necessary (Section 3.3). Furthermore, careful analysis of geometrical path differences within the microscope is necessary to reveal time delays of signals that would hinder the correct determination of plasmon group velocities (Section 3.4). Finally, the accuracy of the technique is discussed (Section 3.5).

The work presented in the current chapter was supported by the work group of Bert Hecht[1]. Regular discussion meetings advanced the project and scanning electron microscope (SEM) characterization of silver nanowires was performed by members of this group.

Parts of this chapter have been published in [Rewitz12a] and [Rewitz12b], as detailed on page iv.

3.1 Motivation

The fundamental plasmonic waveguide structures introduced in Sections 2.4.2 and 2.4.3 offer subwavelength confinement of guided light fields, while miniaturization and packaging density of integrated optics purely based on dielectrics is limited by the wavelength-scale modal profiles of conventionally guided modes [Yariv89]. Therefore, and because plasmonic waveguide structures can be enhanced and modified to devise well-defined functional plasmonic elements [Ozbay06, Gramotnev10], they are very interesting in terms of signal processing. In fact, integrated plasmonic circuitry is discussed as a future optical data processing chip-scale technology [Zia06, Guo13] and many scientific works address this issue, see, e.g., [Fu12, Pan13]. The building blocks of integrated plasmonic circuits include optical antennas for an efficient interconversion of far-field and near-field modes [Mühlschlegel05, Huang09, Wen09, Agio13] as well as plasmonic waveguides with particular functions such as splitting [Bozhevolnyi06, Reiserer10], filtering [Bozhevolnyi06] and switching [Reiserer10, Wei11a, Wei11b].

So far, much work related to the characterization of information transport properties of suitable nanostructures relies on simulations and local near-field measurements, thus providing some insight into characteristic optical properties. However, to accurately assess the

[1]Nano-Optics and Biophotonics Group, Experimentelle Physik 5, Universität Würzburg, Am Hubland, 97074 Würzburg, Germany

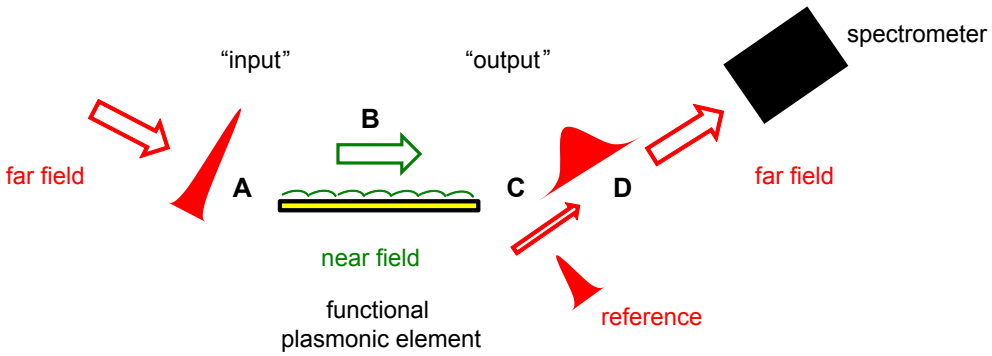

Figure 3.1: Scenario of optically integrated plasmonic circuits and response function characterization via spectral interferometry. A pulsed far-field light source excites propagating plasmons (A) that are processed by a functional plasmonic element (B). After propagation the pulses are converted back into a far-field detectable signals (C) and full characterization (amplitude and phase) is facilitated via spectral interferometry (D) (cf. Section 2.2). Figure taken from [Rewitz12a]. © (2012) Optical Society of America.

overall function and performance of plasmonic elements, it is important to investigate relevant parameters such as the speed of plasmon propagation in a work environment. In Fig. 3.1 such a setting is sketched. It includes a pulsed far-field light source that locally excites guided plasmons (A), a functional plasmonic element that processes the guided waves (B), and an outcoupling region where guided plasmons are converted back into far-field propagating photons (C).

An approach to this setting without using high spatial resolution or pulsed excitation has been the spectral analysis of white light transmitted through plasmonic metal films with slit–groove pairs yielding the group velocity of two-dimensional surface plasmons [Temnov07]. Furthermore, interference of plasmons in nanowires acting as resonators has been detected at the distal and the input end of these nanowires to determine plasmon losses and group velocities [Ditlbacher05, Allione08]. However, both methods rely on self-interference of plasmons and, hence, are limited, e.g., with respect to the geometry of the nanostructure.

In contrast, the heterodyne technique of spectral interferometry (cf. Section 2.2) employs a reference pulse together with spectrally resolved detection for full characterization (amplitude and phase) of electric fields, e.g., transmitted through a periodic nanoslit/-hole array using weakly focused fields [Ropers06]. In a related heterodyne technique the interference is detected without spectral resolution and the delay time between signal and reference pulse has to be scanned. This technique has been used previously to characterize propagation of plasmon pulses on the surface of a nanostructured metallic film [Rokitski05]. A combination of this technique with near-field microscopy has been implemented to characterize the propagation of pulsed near fields in photonic [Balistreri01] and plasmonic waveguides [Sandtke08].

In this chapter, a technique is presented where a confocal microscope is combined with spectral interferometry. The excitation and detection positions can be chosen independently, which enables optical excitation of a certain structure at one spot while monitoring its emission at another spot. Thus, the setup is capable of measuring spectral response functions

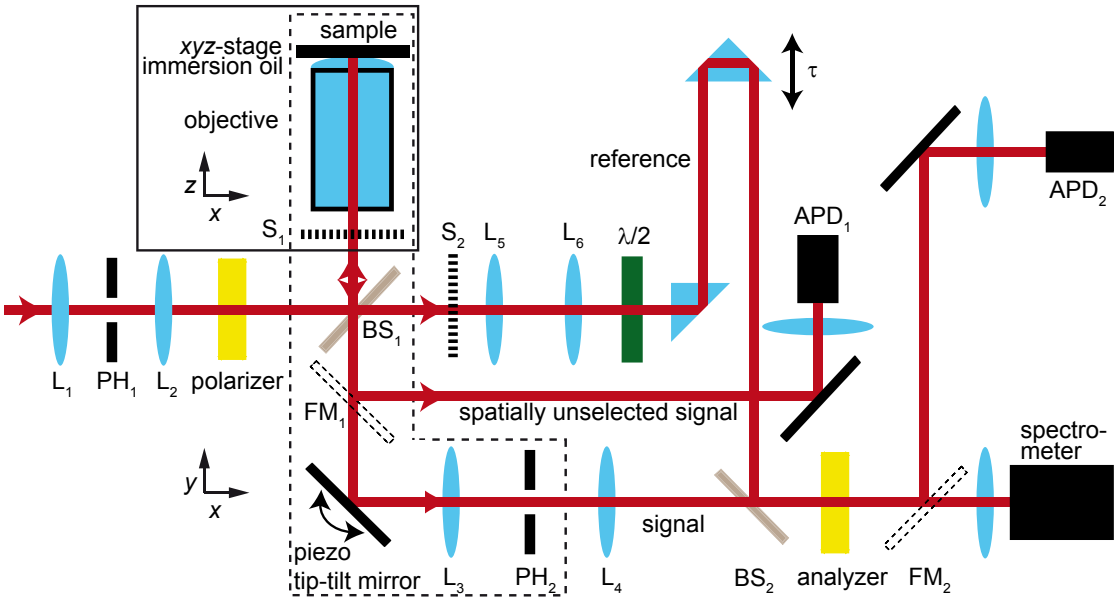

Figure 3.2: Scheme of the spectral-interference microscope setup. BS = beam splitter, S = shutter, L = lens, PH = pinhole, FM = flip mirror, APD = avalanche photodiode. The linearly polarized excitation beam is split into a part for excitation and a reference. Signals from the sample plane are redirected by a piezo tip-tilt mirror to pass the confocal pinhole (PH_2). The reference beam is dispersion compensated by traversing two prisms before being recombined with the signal for spectrally resolved heterodyne detection. The part in the dashed frame is discussed in Fig. 3.6. Figure adapted from [Rewitz12a]. © (2012) Optical Society of America.

with spatial resolution. This allows, e.g., to characterize the group velocities of propagating plasmons in optically integrated nanostructures (Fig. 3.1).

3.2 Experimental Setup

The laser source used in all experiments in this work is a home-built Ti:Sapphire oscillator with a peak wavelength of $\lambda_0 = 800\,\text{nm}$ and a spectral full-width at half-maximum (FWHM) of typically $\Delta\lambda = 46\,\text{nm}$. Details on the properties and alignment of this particular laser system can be found in [Voll97, Schramm00, Keitzl11, Goetz12]. The spectral-interference microscope is based on the setup used to explain spectral interferometry (cf. Fig. 2.1) and an early version is also described in [Reiserer09].

As shown in the scheme of the spectral-interference microscope setup (Fig. 3.2), the incoming femtosecond laser pulses first pass a Keplerian telescope (L_1:$f = 35\,\text{mm}$ and L_2:$f = 75\,\text{mm}$) with a pinhole (PH_1; $d = 15\,\mu\text{m}$) in the common focal plane. This combination expands the beam diameter to ensure overfilling of the microscope objective's back aperture (cf. Section 2.3) and enables reproducible coupling of the laser beam to the setup on a daily basis, which is achieved by maximizing the transmitted power. A subsequent polarizer ensures that the excitation polarization is linear. The first beam splitter BS_1 reflects 8% of the incoming *s*-polarized light towards an immersion-oil objective (Nikon Plan Apo, $100\times/1.40$) in order to excite nanostructures in the sample plane. An *xyz*-piezo stage (P-517.3CL, PI,

Germany) moves the sample relative to the excitation beam—thereby defining the excitation position and adjusting the focus.

The same objective is also used to collect light emitted from arbitrary positions of the sample plane within its field of view. Most of the collected signal is transmitted through BS_1 ($T_p = 99\%$ and $T_s = 92\%$) and is redirected via a piezo tip-tilt mirror (S-334.2SL, PI, Germany) towards a second telescope–pinhole combination (L_3:$f = 200\,\mathrm{mm}$ and L_4:$f = 50\,\mathrm{mm}$, PH_2:$d = 30\,\mu\mathrm{m}$). Applying the confocal principle (cf. Section 2.3), this combination allows selection of particular (diffraction-limit sized) spots from the field of view, independent on the excitation position. To facilitate differentiation between excitation spot reflection or scattering and emitted light from the nanostructure, an analyzer can be oriented to select the polarization component of the emission signal that is orthogonal to the excitation polarization, thus realizing a crossed-polarizer scheme. Via a flippable mirror (FM_1) the signal can also be directed to an avalanche photo diode (APD_1, Perkin Elmer, SPCM-CD 2801) without passing the pinhole and the analyzer, i.e., the reflection and emission from the sample plane is then detected without extra spatial or polarization selection. This allows easy acquisition of images when the sample is raster scanned with the *xyz*-piezo stage (cf. Fig. 3.4a, "excitation scan"). A different avalanche photo diode (APD_2, Perkin Elmer, SPCM-AQR-13) is used as detector when the piezo tip-tilt mirror is scanned while the excitation position is fixed (e.g., Figs. 3.4b and 3.4c, "emission scans"). Details of the data acquisition are discussed in the next section.

The part of the excitation beam transmitted by BS_1 is used as reference. It also passes a telescope (L_5:$f = 220\,\mathrm{mm}$ and L_6:$f = 50\,\mathrm{mm}$) in order to match the signal-beam diameter. A combination of $\lambda/2$-plate and the analyzer acts as a variable attenuator for the reference beam intensity and ensures the same detection polarization for the reference and signal beams, which is important for spectral interferometry. The optimal reference intensity can be calculated for each measurement separately, see [Goetz12]. The reference beam then traverses two NBK-7 prisms in total-internal-reflection mode in order to introduce approximately the same second-order dispersion [cf. Eq. (2.19)] as caused by the microscope objective. This improves the signal–to–noise ratio of the amplitude and phase reconstruction process, which is described in the next section.

Signal and reference beams are recombined at the second beam splitter (BS_2; equivalent to BS_1), which exhibits high transmission for the signal beam. The second flippable mirror (FM_2) allows switching between APD_2 and a spectrometer [spectrograph (Princeton Instruments, Acton SpectraPro 2500i) and charge-coupled device (e2v, CCD42-10 in Princeton Instruments, Acton Pixis2kB)] as detector. The spectrometer is used to record spectral interferograms at specific positions within "emission scans" (e.g., Figs. 3.5a and 3.5b). Signal and reference path lengths are chosen to be equal. One of the prisms is mounted on a micrometer translation stage, which makes it possible to adjust the time delay τ between signal and reference pulse.

3.3 Experimental Procedure

To demonstrate the capabilities of the spectral-interference microscope and introduce the basics in data acquisition and evaluation, chemically grown silver nanowires (PlasmaChem

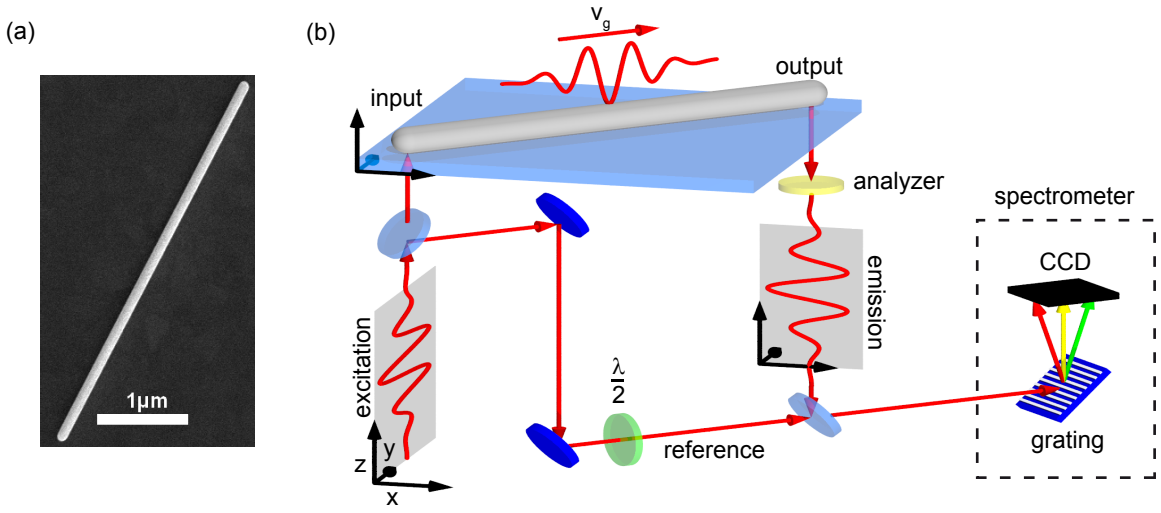

Figure 3.3: (a) Scanning electron micrograph of a representative silver nanowire with diameter $d = 115\,\text{nm}$ and length $l = 4.5\,\mu\text{m}$. (b) Principle of the plasmon propagation experiment. A propagating plasmon pulse is excited with an y-polarized femtosecond laser pulse at one end of a silver nanowire (input). The nanowire is oriented to include a -45° angle with the y axis. After propagating along the nanowire the plasmon pulse is radiated into a free-space propagating pulse at the other end (output). The analyzer (yellow disk) selects the x component of the emission signal and, thus, suppresses reflected or scattered light. The emission signal is then superimposed with the reference beam and the resulting interferometric signal is detected by a spectrometer. The $\frac{\lambda}{2}$-plate (green disk) rotates the polarization of the reference parallel to the analyzer axis. Figures adapted from [Rewitz12b]. © (2011) American Chemical Society.

GmbH, Berlin, Germany) are used. The nanowires have been drop-casted on indium tin oxide (ITO)-covered microscope cover slips. The transparent and conductive ITO layer with a thickness of 200 nm is required to avoid charging effects in the SEM. Figure 3.3a shows a representative SEM image of such a nanowire. After evaporation of the solvent (H_2O) and SEM characterization the nanowires were embedded in index-matching immersion oil (Type B, Cargille-Sacher Laboratories Inc., NJ, USA) in order to suppress reflections from the interface between cover slip and ambient air.

Data Acquisition

The silver nanowire plasmon propagation experiment is sketched in Fig. 3.3b. It is a more detailed example of the general scheme for response function characterization of functional plasmonic elements shown in Fig. 3.1. Here, the linearly y-polarized femtosecond laser pulse excites a plasmon at one end of a silver nanowire (input). The plasmon pulse propagates with a certain group velocity v_g along the nanowire and is re-emitted as a free-space propagating light pulse at the other end of the nanowire (output). The emitted field is characterized by collinear superposition with the reference pulse and spectrally resolved detection. As discussed in Section 2.4.4, optimal excitation of the fundamental plasmon mode in silver nanowires is obtained for a polarization parallel to the nanowire. However, in the present case the nanowire's long axis is deliberately oriented with a ca. -45° and +45° angle to

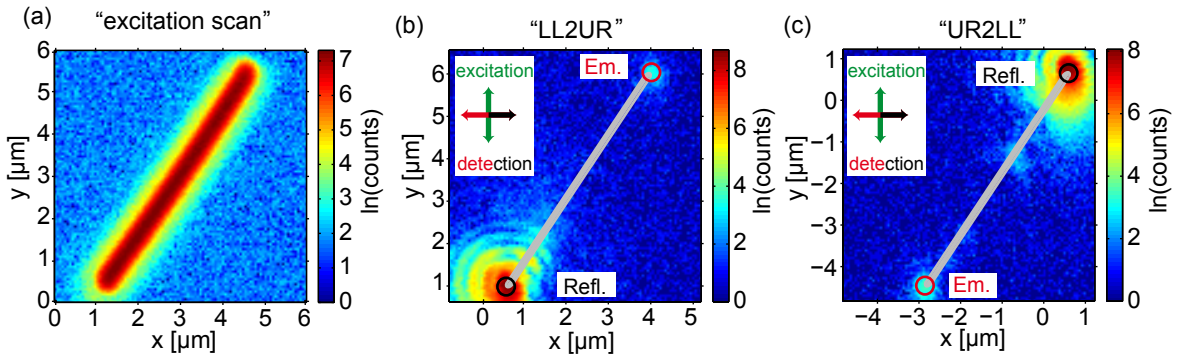

Figure 3.4: Example images of plasmon propagation experiments. All images show spatial maps of measured time-integrated intensities. (a) An "excitation scan" that is used to locate a nanowire is shown. (b) An "emission scan" that is recorded by scanning the piezo tip-tilt mirror is depicted. The reflection of the excitation spot at the lower end of the nanowire ("Refl.", black circle) and the emission at the upper end of the nanowire ("Em.", red circle) are visible. Both signals can be completely characterized via spectral interferometry, see Fig. 3.5. The gray nanowire is sketched for convenience. Since the plasmon propagates from the lower left (LL) to the upper right (UR), this measurement is termed "LL2UR-propagation". (c) The analog experiment for a "UR2LL-propagation" is shown. The insets in (b) and (c) show the excitation and detection polarizations. The axes of (b) and (c) are labeled with respect to the center of the position-dependent pulse arrival time (PD-PAT), which is explained in Section 3.4. Here, the labeling shows that the excitation position ("Refl.") is the same in measurements (b) and (c) and the nanowire is shifted with respect to this position, as explained in the main text. Figures taken from [Rewitz12a]. © (2012) Optical Society of America.

the excitation and detection polarization, respectively. This configuration allows to apply the crossed-polarizer scheme, which suppresses reflected light, without severe loss of signal strength.

In order to perform an "excitation scan" the sample is raster scanned in the x–y plane and the time-integrated intensity of the reflected signal is recorded without any extra spatial or polarization selection using APD_1 (cf. Fig. 3.2). As a result scan images as shown in Fig. 3.4a are acquired in which the silver nanowires appear as bright elongated structures due to the increased reflection of light in its immediate vicinity. In these images the excitation pulse is linearly polarized along the y axis. The transmission axis of the analyzer is oriented along the x axis for realization of the crossed-polarizer scheme in "emission scans".

With the nanowire in the described orientation, there are two options for a plasmon propagation experiment: Either the lower left end of the nanowire is excited and plasmons propagate towards the upper right end ("LL2UR"), where they can be converted back into far-field detectable signals, or the plasmons can be launched at the upper right end and the emission can be detected at the lower left end ("UR2LL"). In either case the respective input end of the nanowire is placed at the position of the excitation focus. With this excitation position fixed, the piezo tip-tilt mirror in the detection path (cf. Fig. 3.2) is used to obtain a spatially resolved map of the time-integrated sample emission ("emission scan") as shown in, e.g.,

Fig. 3.4b ("LL2UR"). In such a map, the direct reflection is readily visible at the excitation position ("Refl.", black circle in the lower left part of Fig. 3.4b). No leakage radiation can be detected along the nanowire since it has very little surface roughness (cf. Section 2.4). The radiative decay of plasmons at the output end can, however, be observed as a bright spot, which is well separated from the reflection spot for sufficiently long nanowires ($\gtrsim 1.5\,\mu$m). This emission can be seen in the upper right part of Fig. 3.4b ("Em.", red circle). The fact that the directly reflected spot is visible at all in the crossed-polarizer scheme is due to high-NA depolarization effects [Hecht06] and is exploited to obtain the reference starting time of the plasmon pulse as indicated in Fig. 3.5g. The emission intensity can be optimized by fine positioning the nanowire end with respect to the excitation position using an automatic routine. Figure 3.4c shows the same experiment for the reverse plasmon propagation direction ("UR2LL").

Spectral interferometry detection is performed by overlapping the reflected and the emitted pulses after propagation (the signals in the black and red circles of Figs. 3.4b and 3.4c, respectively) individually with the reference pulse. Both positions are measured consecutively and the heterodyne signal is recorded with the spectrometer. Even though the amplifying heterodyne detection technique is used, higher excitation intensities than for measurements with the avalanche photo diodes are usually required since the signal is dispersed over many CCD pixels and the used grating is blazed for 500 nm. The spectral interferograms corresponding to the experiment shown in Fig. 3.4b are depicted in Fig. 3.5a (reflection, black) and Fig. 3.5b (emission, red). As can be inferred from the modulation of the red line over the complete spectrum, all spectral components of the laser pulse are transmitted through the nanowire.

Data Evaluation

To apply the Fourier-transform scheme for amplitude and phase retrieval (cf. Section 2.2), only the separately measured reference intensity $I_{\mathrm{ref}}(\lambda)$ is subtracted from the spectral interferograms and then a first fast Fourier transform is applied. Measurement of the reference intensity $I_{\mathrm{ref}}(\lambda)$ is facilitated with computer controlled shutters (by closing shutter S_1 in Fig. 3.2). Because of the dispersion compensation in the reference beam, the second-order spectral phases of signal and reference pulse are almost equal. As explained in Section 2.2, this yields narrow and, therefore, high peaks for the oscillatory part after this first fast Fourier transform (cf. shaded areas in Figs. 3.5c and 3.5d). Hence, a relatively short delay time between signal and reference pulse ($\tau \approx 600$ fs), which is well below the Nyquist limit of the detector, can be used and the signal–to–noise ratio is improved compared to a measurement without dispersion compensation in the reference beam. The oscillatory parts are then isolated with Fourier windows (shaded areas in Figs. 3.5c and 3.5d) and inversely fast Fourier transformed before being resampled in ω-space. This yields complex-valued numbers $S_i^+(\omega)$ [cf. Eq. (2.29)], with $i =$ Refl. and $i =$ Em., from which the spectral signal intensities $I_i(\omega) = |S_i^+(\omega)|^2/I_{\mathrm{ref}}(\omega)$ (which can also be measured separately by closing shutter S_2 in Fig. 3.2) and the difference phases with respect to the reference pulse phase

$$\varphi_{\mathrm{diff},i}(\omega) = \varphi_i(\omega) - \varphi_{\mathrm{ref}}(\omega) = -\arg S_i^+(\omega) \tag{3.1}$$

of both signals are calculated as can be seen in Fig. 3.5e and Fig. 3.5f.

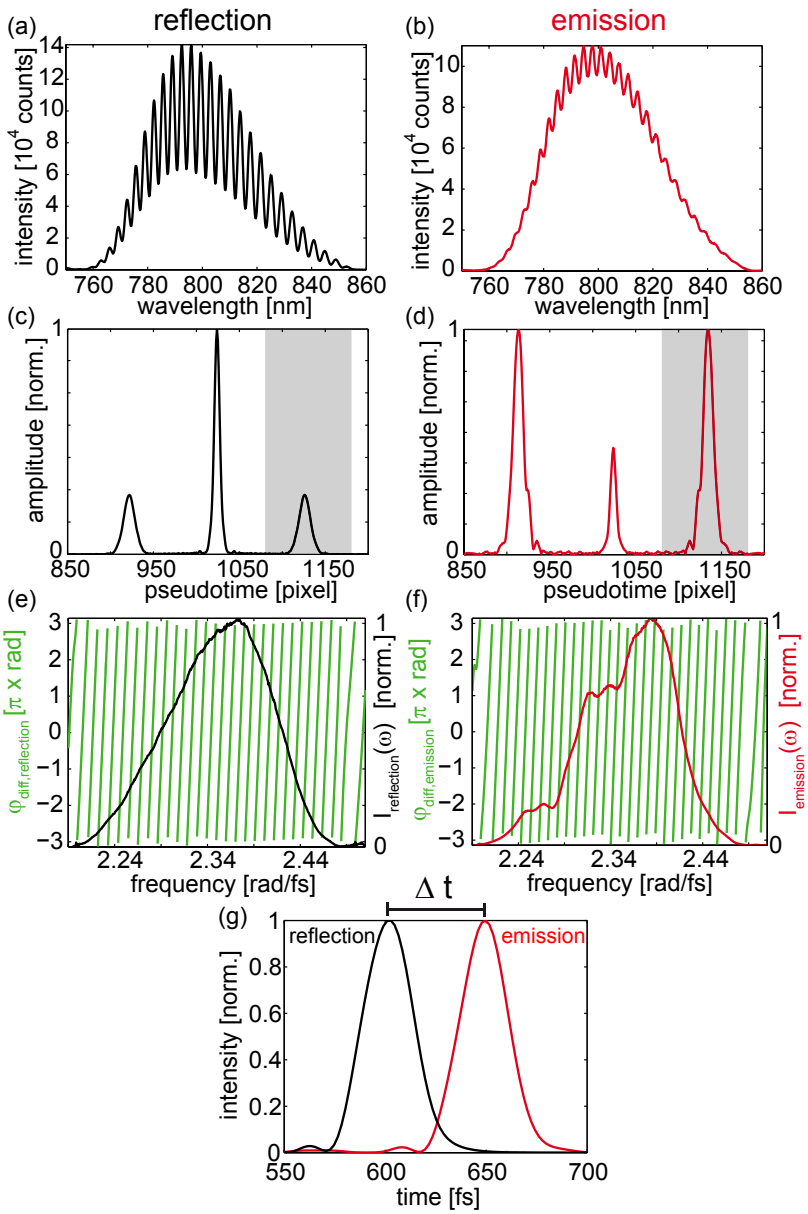

Figure 3.5: Data evaluation process. The left (right) column shows data from the reflection (emission) position. (a,b) Spectral interferograms recorded at the respective positions of Fig. 3.4b (black and red circle) are shown. (c,d) The amplitudes after the first fast Fourier transform are depicted. Since the spectrometer detector provides 2048 pixels for the wavelength-space sampling, the non-oscillatory part is centered around pixel number 1024. The shaded area depicts the Fourier window that is used for the second (inverse) fast Fourier transform. From this transformation the reconstructed intensity $I_i(\omega)$ and difference phase $\varphi_{\mathrm{diff},i}(\omega) = \varphi_i(\omega) - \varphi_{\mathrm{ref}}(\omega)$ can be deduced (e,f). Employing a third fast Fourier transform using the data of (e) and (f) yields the temporal envelopes depicted in (g). The separation time Δt is deduced from the maxima and has to be corrected for the position-dependent pulse arrival time (PD-PAT, see Section 3.4) to yield the plasmon propagation time t_{prop}. Figures taken from [Rewitz12a]. © (2012) Optical Society of America.

The spectral-phase response function of the plasmonic element can then be calculated by subtracting the retrieved phase of the reflected pulse from that of the emitted pulse, thereby eliminating the reference pulse phase:

$$\varphi_{\text{response}}(\omega) = \varphi_{\text{diff,Em.}}(\omega) - \varphi_{\text{diff,Refl.}}(\omega) \tag{3.2}$$

In the case of silver nanowires, this spectral-phase response function does not seem very interesting at first glance since it is mostly linear. As can be seen from Figs. 3.5e and 3.5f, both phases $\varphi_{\text{diff},i}(\omega)$ have a strong linear slope according to $\tau \approx 600\,\text{fs}$ but show little curvature. However, the linear slope of the response function indicates the difference in arrival time of the reflected and the emitted signal. For a detailed analysis of this separation time taking the linear term of a polynomial fit is too error-prone because multiple parameters that influence the result have to be chosen by hand (e.g., polynomial order or fitting region). Instead, a third and final fast Fourier transform is employed using the measured signal amplitude $\sqrt{I_i(\omega)}$ and the reconstructed spectral difference phase $\varphi_{\text{diff},i}(\omega)$, both zero padded at high frequencies, of the reflection and the emission signal to obtain the temporal envelopes shown in Fig. 3.5g. The arrival time of the reflection pulse at ca. 600 fs (black) indicates the adjusted delay of the signal pulse with respect to the reference pulse. Because of plasmon propagation, the emission (red) arrives at a time Δt later. This time can easily be evaluated by subtracting the temporal positions of the maxima of both envelopes. In the case of multiple reflections of the propagating plasmon wave inside the nanowire multiple signal pulses are expected. These pulses will show up as additional (though much lower) peaks in the temporal envelopes and will not affect the data evaluation because only the global maximum is evaluated.

Miscellaneous

There are two reasons for the triple fast Fourier transform evaluation. First, reconstruction of $I_i(\omega)$ and $\varphi_{\text{diff},i}(\omega)$ is necessary to calculate the spatial-spectral response function of a plasmonic element [cf. Eq. (3.2)]. Second, it is not possible to retrieve exact timing information from the first fast Fourier transform, which starts in λ-space and, hence, does not yield time-domain information. Therefore, the abscissae in Figs. 3.5c and 3.5d are termed "pseudotime". It would be necessary to resample the spectral interferogram in the ω-space to directly yield time-domain information. This introduces errors due to interpolation of the highly modulated data [Dorrer00], while resampling the filtered data after the second Fourier transform does not introduce significant interpolation errors.

Due to the fact that the plasmon propagation time for the investigated micrometer-long structures is in the range of tens of femtoseconds it is important to carefully consider time offsets that may be acquired within the setup due to different optical paths. As shown in the next section, path differences due to the different detection positions in the sample plane (cf. "Refl." and "Em." circles in Figs. 3.4b and 3.4c) translate into a position-dependent pulse arrival time (PD-PAT) at the detectors and can indeed not be neglected. Consequently, the separation Δt of the maxima in Fig. 3.5g have to be corrected by the PD-PAT to yield the plasmon propagation time t_{prop}. This correction is discussed in the next section.

3.4 Position-Dependent Pulse Arrival Time (PD-PAT)

Time delays due to geometrical path differences that are acquired in the spectral-interference microscope because of the different detection positions in the sample plane (cf. "Refl." and "Em." circles in Figs. 3.4b and 3.4c) translate into a position-dependent pulse arrival time (PD-PAT).

Definition

The time delays that occur in the present setup can be accounted for by a ray-tracing model as depicted in Fig. 3.6. The figure shows an idealized and simplified two-dimensional scheme of the setup's part enclosed in the dashed frame of Fig. 3.2 and is also similar to Fig. 2.2a. Signals (green and red lines) emerge from the sample plane, pass the objective, are redirected by the piezo tip-tilt mirror (black dashed for tilting position 1 and black solid for tilting position 2) and subsequently focused onto the pinhole (PH_2). As explained in Section 2.3, by scanning the piezo tip-tilt mirror around its center (M), different sample plane positions are selected by the pinhole. The green path (1) indicates a signal emerging from the center of the sample plane. In that case, the beam path coincides with the optical axis of the objective and is reflected at the center of the piezo tip-tilt mirror. After this reflection the beam path coincides with the optical axis of lens L_3 and the signal is focused onto the pinhole in the image plane. In this setting of the piezo tip-tilt mirror (dashed black) the mirror normal and the optical axis of the objective form a 45° angle ("zero position"). On the other hand, the red path (2) indicates a signal that emerges a distance r away from the center of the sample plane. The angle α is connected to this distance via $\alpha = \arctan(r/f_{\text{obj}})$, with $f_{\text{obj}} = 2\,\text{mm}$ being the focal length of the objective. This can be simplified to $\alpha = r/f_{\text{obj}}$, since very small angles are considered ($\pm 10\,\mu\text{m} \mathrel{\widehat{=}} \pm 0.005\,\text{rad}$). With the piezo tip-tilt mirror in its "zero position" this signal (2) would not be imaged onto the pinhole (cf. Section 2.3). However, by tilting the piezo tip-tilt mirror about an angle of $\alpha/2$ around its center as indicated (solid black) the signal is deflected such that it passes the pinhole.

The optical path length difference between 2 and 1 (from the sample plane to the reference plane) can be obtained via trigonometry and yields (see Appendix A.2 for a derivation and approximations)

$$\overline{2} - \overline{1} = -(L_{\text{obj}} n_{\text{obj}} + D)\frac{\alpha^2}{2} = -\frac{A}{2}\left(\frac{r}{f_{\text{obj}}}\right)^2, \tag{3.3}$$

with n_{obj} being the objective's (average) refractive index. The distances L_{obj} and D are defined in Fig. 3.6. On the right hand side of the second equivalent sign the PD-PAT Amplitude $A = L_{\text{obj}} n_{\text{obj}} + D$ was introduced. The negative sign in Eq. (3.3) indicates that path 2 is shorter than path 1. Since the problem is rotationally symmetric, i.e., only the distance r to the sample center within the sample plane is important, signals from an outer rim in the sample plane arrive earlier at a detector behind the pinhole than signals that emerge from the center.

The field of view, i.e., the part of the sample that is imaged onto the detector, is defined by the objective. The center of the field of view is defined by the optical axis of the objective. For an ideally aligned excitation beam that propagates along this optical axis the position of the excitation focus is identical with this field of view center. Furthermore, in the idealized

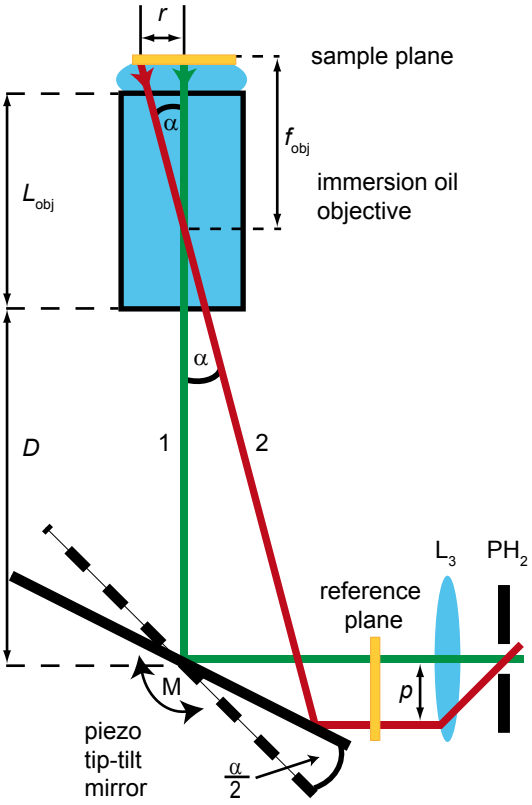

Figure 3.6: Ray-tracing model for the position-dependent pulse arrival time (PD-PAT). By scanning the piezo tip-tilt mirror different sample positions are mapped onto the pinhole (PH_2). For the black dashed position, signal 1 (green path) emerging from the center of the sample plane is focused onto the pinhole. Tilting the mirror by $\alpha/2$ (black solid position) redirects signal 2 (red path) through the pinhole. Figure adapted from [Rewitz12a]. © (2012) Optical Society of America.

description of the PD-PAT origin above it is assumed that the center of rotation of the piezo tip-tilt mirror lies on the optical axis of the objective (green path 1). If this is not the case, and the center of rotation is shifted a distance Δm in a plane perpendicular to the optical axis, the PD-PAT center position is displaced by the amount Δx relatively to the field of view center. In this case the focus excitation/reflection position and the PD-PAT center are not identical. In the spectral-interference microscope setup, a distance of $\Delta m = 1\,\text{mm}$ roughly corresponds to a shift of $\Delta x = 5\,\mu\text{m}$. In order to take this alignment factor into account, the PD-PAT value in the sample plane is modeled as

$$T_{\text{PD-PAT}}(x,y) = -\frac{A}{2c}\left(\frac{(x+\Delta x)^2+(y+\Delta y)^2}{f_{\text{obj}}^2}\right), \tag{3.4}$$

with $(\Delta x^2+\Delta y^2)^{1/2}$ being the shift of the field of view center relative to the PD-PAT center, and c the speed of light in vacuum. In "emission scan" images (e.g., Figs. 3.4b, 3.4c, and 3.7) the axes are labeled with respect to the PD-PAT center, i.e., the position (0,0) in these images is the PD-PAT center.

Experimental calibration of Eq. (3.4) determines the three parameters A, Δx, and Δy. The amplitude $A = L_{\text{obj}} n_{\text{obj}} + D$ can be measured directly at the setup [see Fig. 3.6, $L_{\text{obj}} = 5.5\,\text{cm}$, $n_{\text{obj}} = 1.51$, and D=$(39.7 \pm 0.5)\,\text{cm}$]. This yields a value of $A = (48.0 \pm 0.5)\,\text{cm}$. In contrast, the PD-PAT center position does not necessarily coincide with the excitation/reflection position and the relative shift (Δx, and Δy) has to be determined with a different method, which is outlined in Appendix A.3. The development of this method was a challenging task.

However, with all three parameters at hand $T_{\mathrm{PD-PAT}}(x, y)$ can be calculated for all positions within the sample plane and the PD-PAT correction can be applied to the separation time Δt from the plasmon propagation experiment (cf. Figs. 3.4 and 3.5). This is done by calculating a correction time t_{corr} from the PD-PAT values at the reflection and emission positions $[t_{\mathrm{corr}} = T_{\mathrm{PD-PAT}}(x_{\mathrm{Refl.}}, y_{\mathrm{Refl.}}) - T_{\mathrm{PD-PAT}}(x_{\mathrm{Em.}}, y_{\mathrm{Em.}})]$. The corrected propagation time is then defined as

$$t_{\mathrm{prop}} = \Delta t + t_{\mathrm{corr}}. \tag{3.5}$$

For the calculation of the plasmon velocity

$$v = l/t_{\mathrm{prop}} \tag{3.6}$$

the separation of the reflection and emission position is the wire length l.

Demonstration and Verification

In order to demonstrate, visualize, and verify the PD-PAT model, the sample plane has to be illuminated in a quite large area (e.g., $20 \times 20\,\mu\mathrm{m}^2$). Extensive studies [Keitzl11] revealed that the best option for this purpose is a convex lens inserted in front of the polarizer (cf. Fig. 3.2). The focal length and position of this lens is chosen to focus the excitation beam in the back focal plane of the objective (cf. Fig. 2.2b). This yields a large focal spot in the sample plane. The reflection of this large focal spot is then imaged onto the pinhole plane (PH_2). Some annotations regarding this configuration can be found in Appendix A.4. The sample for this experiment is a plain microscope cover slip and the analyzer is set to the same orientation as the polarizer since the direct reflection of the glass–air interface is of interest. By applying the data evaluation method (cf. Fig. 3.5) to every position within the sample plane (here, "reflection" = center of scanned area, "emission" = all other positions), the measured position-dependent pulse arrival time (PD-PAT) can be visualized as shown in Fig. 3.7a. Note that compared to Figs. 3.4b and 3.4c the scan area now is $20 \times 20\,\mu\mathrm{m}^2$ and the color code represents relative arrival time rather than intensity.

As expected from the model [Eq. (3.4)], a rotationally symmetric dependence is visible and signals emerging further away from the center of the scanned area arrive earlier at the detector. Fitting the measured data with Eq. (3.4) results in an amplitude of $A = 47\,\mathrm{cm}$ with a confidence interval of 1 cm, which agrees with the value used for calculating $T_{\mathrm{PD-PAT}}(x, y)$ $[A = (48.0 \pm 0.5)\,\mathrm{cm}]$. Furthermore, the difference of the measured and fitted time-correction data has a standard deviation of about 1 fs, indicating that no additional parameters have to be considered in Eqs. (3.3) or (3.4).

In this demonstration experiment, the lateral positioning of the additional lens in front of the polarizer modifies the beam path towards the objective and determines the center position of the measured PD-PAT [the position of the minimum pulse delay in Fig. 3.7a is not centered at (0,0)]. Therefore, this center position has to be determined in a different fashion as discussed in Appendix A.3. Then, the PD-PAT can be calculated with Eq. (3.4). The result is shown in Fig. 3.7b for the same area as measured in Fig. 3.7a. For the calculation the parameters $A = 48.0\,\mathrm{cm}$, $\Delta x = 0.68\,\mu\mathrm{m}$, and $\Delta y = 1.13\,\mu\mathrm{m}$ are used. As a consequence, the position of minimum pulse delay is centered at (0,0). Comparing

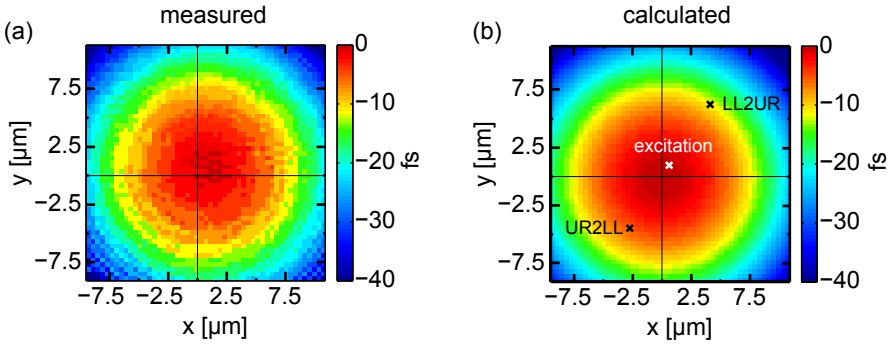

Figure 3.7: Visualizations of the PD-PAT. Note that the area size is $20 \times 20\,\mu\text{m}^2$ and the color code represents relative arrival time. (a) The measured data that is acquired by illuminating the complete area is depicted. (b) The calculated data according to Eq. (3.4) is shown. The parameters $A = 48.0\,\text{cm}$, $\Delta x = 0.68\,\mu\text{m}$, and $\Delta y = 1.13\,\mu\text{m}$ are used. The measured and calculated data agree very well, thereby verifying the PD-PAT model and indicating the stability of the spectral-interference microscope. In order to connect this visualization to the plasmon propagation experiment shown in Fig. 3.4, the reflection and emission positions from that figure are marked here with white and black crosses, respectively. Figure adapted from [Rewitz12a]. © (2012) Optical Society of America.

the measured (Fig. 3.7a) and calculated (Fig. 3.7b) data reveals the very good agreement. In Fig. 3.7b the reflection and emission positions of the plasmon propagation experiment (cf. Fig. 3.4) are marked with white and black crosses, respectively. As can be seen, the PD-PAT center (0,0) does not coincide with the excitation/reflection position and different corrections have to be applied for both measurement directions.

3.5 Error Analysis

As discussed in the previous two sections, group velocities of plasmons propagating along nanostructures can be experimentally determined with the spectral-interference microscope by a rather complex procedure, which combines data acquisition, data evaluation, and PD-PAT correction. In the current section, the accuracy of results is discussed by considering the errors of several steps in this procedure.

First of all it should be mentioned that measurements of nanostructures that show strongly distorted emission spots together with low emission intensities have to be discarded. For these nanostructures, which surprisingly often show no defects in scanning electron micrographs, either the launching, the propagation or the radiative decay of plasmons does not work properly. The distortion argument is qualitative but for the ratio of emission intensity and optimal reference intensity a lower threshold of $3 \cdot 10^{-3}$ should be used. The errors of determined plasmon group velocities can be calculated according to formal error propagation, as discussed in detail in the following.

Recording several (e.g., nine) spectral interferograms at both positions ("Refl." and "Em." in Figs. 3.4b and 3.4c) for each measurement results in an average separation time $\langle \Delta t \rangle$. The standard error of this ensemble is usually below 1 fs and can be taken as the absolute

error of the mean separation time [$\Delta(\Delta t)$]. However, empirical studies showed that details of the measurement procedure (e.g., time difference between reflection and emission measurement) and details of the data evaluation procedure (e.g., position and size of the Fourier windows) influence the mean separation time. An analysis of these influences can be found in [Goetz12] together with a comprehensive and systematic how-to guideline for the lab in order to minimize errors. From this analysis, it can be concluded that it is more sensible to use the estimated value of 2 or 3 fs as absolute error for all measured separation times instead of the value determined separately for each measurement.

Formal error propagation treatment of the PD-PAT formula [Eq. (3.4)] yields the absolute error of the PD-PAT value. Here, a position inaccuracy of $\Delta x_i = \Delta y_i = 0.1\,\mu$m is assumed. The parameters of Eq. (3.4) are determined (see also Appendix A.3) to have errors of $\Delta(\Delta x) = \Delta(\Delta y) = 0.3\,\mu$m, and $\Delta A = 1$ cm. The total error of the correction time depends on the separation l of the reflection and emission position (cf. Figs. 3.4b,c) and is around $\Delta t_{\text{corr}} \approx 1$ fs for $l = 5\,\mu$m. Thus, the accuracy of the setup-inherent signal-delay calibration is better than that of the measured separation times and the error of the propagation time can be taken as $\Delta t_{\text{prop}} = 3$ fs [cf. Eq. (3.5)]. Due to thermal and mechanic influences, the PD-PAT should be re-calibrated regularly in order to obtain best results [Goetz12].

For calculation of the plasmon group velocity [Eq. (3.6)], the inaccuracy of the propagation length l, which is defined as the separation of the reflection and emission position, is assumed to be $\Delta l = 0.15\,\mu$m. It is not sensible to use more accurate values determined by scanning electron microscopy because the position from which the timing information is derived in "emission scans" can only be evaluated with this precision.

For typical parameters ($l = 5\,\mu$m, $v = 1 \cdot 10^8$m/s) the complete procedure yields final calculated errors of plasmon group velocities of $\Delta v = 0.07 \cdot 10^8$m/s. Since the largest contributions to this inaccuracy stem from the random errors of the measured separation time [$\Delta(\Delta t)$] and length (Δl), it can easily be reduced by averaging multiple measurements, e.g., both measurement directions ("LL2UR" and "UR2LL").

Apart from the geometrical correction (PD-PAT), no additional phase or amplitude effects of the setup have to be considered since the relative change between reflection and emission signals is determined and such effects cancel out automatically. Regarding the reference starting time, apart from the reflection at the input end any reflection of the nanostructure as well as other reflections exactly in the sample plane (cf. Section 4.3) can also be used: The important information is the temporal position at which the input pulse reaches the sample plane. In the case of silver nanowires, the reflection signal is due to a non-resonant (instantaneous) scattering process at the input end. The complex-valued reflection coefficient of this process is constant within the laser pulse spectrum. Therefore, the temporal position of this reflection is the correct starting time of the silver nanowire plasmon mode. An unlikely photon–plasmon conversion time is discussed in Section 4.2. Furthermore, possible phase offsets (i.e., zero-order Taylor coefficients) that may occur upon reflection do not matter for the determination of plasmon group velocity or dispersion of the plasmon mode upon propagation. As a last aspect, it can be verified that the nanostructures are indeed attached to the planar substrate surface by comparing the temporal position of reflected signals at different positions along the nanostructure, e.g., from both ends and the center.

3.6 Summary and Conclusion

In this chapter, an optical technique for characterization of functional plasmonic elements was introduced. It combines confocal microscopy that facilitates independent excitation/detection positioning with spectral interferometry using ultrashort pulses. The technique enables characterization of propagation properties of plasmons and is not limited to nanowires but can be applied to a large variety of nanostructures that support propagating plasmons (cf. Chapters 4 and 5). Since the method provides full amplitude and phase information of the propagated signal, the spatial and spectral response functions of plasmonic functional elements such as splitters, multiplexers, switches or logic gates can be determined. With this far-field microscopy approach, the scenario of optically integrated plasmonic circuits—as depicted in Fig. 3.1—is implemented.

In order to retrieve timing information of the plasmon pulses, time delays due to geometrical path differences within the setup are important. A model for the position-dependent pulse arrival time (PD-PAT) together with experimental calibration is used to achieve an accuracy of about 1 fs in time corrections. This facilitates the determination of group velocities of propagating plasmons. For other applications or further developments of the technique, position dependent amplitude or higher-order phase contributions of the setup might be interesting.

The setup can also be used to investigate non-linear effects on plasmon propagation as a result of ultrashort pulses exciting appropriate nanostructures. Moreover, as shown in Chapter 5, the technique can also be applied to control optical excitations in nanostructures. The far-field laser pulse can be shaped in order to focus the plasmonic energy in space and time as already shown theoretically [Sukharev06, Tuchscherer09].

In future applications, the presented technique might be combined with nonlinear spectroscopy schemes, such as transient grating or coherent 2D spectroscopy [Mukamel99], to determine the third order response function with a spatial resolution down to the diffraction limit.

4 Characterization of Plasmon Group Velocities

In the previous chapter, the spectral-interference microscope was introduced. It has the capability of measuring spatial-spectral response functions of plasmonic structures, including the group velocities of propagating plasmons in optically integrated nanostructures. In the current chapter, the technique is applied to characterize the group velocity and dispersion of plasmon propagation in different nanostructures. In the first part, the geometry dependence of bottom-up, i.e., chemically grown, silver nanowires is characterized and the dependence on the local nanowire environment is demonstrated (Section 4.2). In the second part, two types of top-down, i.e., focused-ion-beam (FIB) milling produced, gold nanostructures are introduced and characterized: single nanowires and two-wire transmission lines (Section 4.3). The findings of this section are of relevance for the design and implementation of nanoplasmonic signal processing and in view of control applications, as shown in Chapter 5.

The work presented in the current chapter resulted from a close collaboration with the work group of Bert Hecht[1]. Regular discussion meetings advanced the project and all presented near-field simulations were done in this group. Furthermore, the production of gold nanostructures as well as scanning electron microscope (SEM) characterization of all nanostructures were performed by members of this group.

Parts of Sections 4.1 and 4.2 have been published in [Rewitz12b].

4.1 Motivation

As already mentioned in Section 3.1, plasmonic waveguides are very interesting in view of applications in the field of integrated optical communication. For signal processing, the propagation of ultrashort pulses representing bits of information is of fundamental importance and needs to be characterized in detail. Of particular interest for the design and implementation of plasmonic nanocircuits is the speed of propagation, i.e., the plasmon group velocity, and the dispersion. The plasmon group velocity for nanowires, i.e., the slope of the plasmon dispersion relation, is expected to depend strongly on the nanowire geometry [Novotny94, Takahara97]. This encompasses peculiar effects such as the vanishing group velocity in adiabatic focusing [Stockman04, Gramotnev05]. Similar behavior is not known for electronic integrated circuits and can lead to characteristic signal delays in information processing systems and in future background-free near-field spectroscopy techniques with ultrafast temporal resolution [Berweger12].

[1] Nano-Optics and Biophotonics Group, Experimentelle Physik 5, Universität Würzburg, Am Hubland, 97074 Würzburg, Germany

Usually, nanowires are used in single mode operation. However, an enhanced functionality of nanooptical circuits could be derived from the control of propagating plasmons based on the interference of multiple near-field modes [Sukharev06, Tuchscherer09]. In this context, the group velocity of multiple well-defined modes existing on appropriate nanostructures is also of high relevance.

4.2 Bottom-Up Silver Nanowires: Dependency on Geometry and Local Environment

Chemically grown silver nanowires are candidates for building blocks of future plasmonic nanocircuits and have been studied extensively in this context [Ditlbacher05, Sanders06, Fang10, Yan09, Wei11a] and in the context of controlling plasmon propagation [Cao10, Cheng10]. They also have been used to study fundamental properties of plasmons [Akimov07, Kolesov09].

In the following, an experimental size-dependent characterization of light that is emitted at one nanowire end due to the conversion of propagating plasmons, which have been excited by a laser pulse at the other nanowire end, is carried out. See Fig. 3.3 for a representative scanning electron image of a nanowire and a sketch of the experiment.

Dependency on Geometry

The commercially available silver nanowires were prepared and characterized in the spectral-interference microscope exactly as explained in Section 3.3. In particular this means that they were situated on indium tin oxide (ITO)-covered microscope cover slips and immersed in index-matched oil. The experimental procedure (cf. Section 3.3) was applied to investigate a set of nanowires with various lengths and diameters determined by scanning electron microscopy. The range of investigated nanowire diameters was $d = 70 - 260\,\mathrm{nm}$, whereas the lengths varied from $l = 1.9\,\mu\mathrm{m}$ to $l = 6.2\,\mu\mathrm{m}$. As expected, the plasmon group velocity shows no systematic dependence on the nanowire length. However, since the data set spans a large range of diameters, a pronounced dependence of the plasmon group velocity on the nanowire diameter is observed (blue crosses in Fig. 4.1). In particular, a drastic decrease of the group velocity for nanowire diameters below $d = 100\,\mathrm{nm}$ as well as a saturation for larger diameters is visible. In the presented data, the velocity varies from 44% (for the largest diameter) to 22% (for the smallest diameter) of the velocity of light in vacuum. This dependence is expected from theory [Stockman04], but has not been experimentally determined before. An intuitive interpretation of the group velocity saturation for increasing nanowire diameters is that the fundamental mode is effectively located within the gap between the metal nanowire and the substrate (cf. inset in Fig. 4.1) and larger diameters do not alter the mode significantly. In contrast, for small nanowire cross sections the intensity distribution of the mode, and thus the dispersion relation, is strongly affected by a change of the diameter.

For comparison, the dispersion relation was also simulated for a two-dimensional system (see Appendix A.1 for simulation details and used refractive indices). Due to the well-known reactivity of silver at ambient conditions [Elechiguerra05] the possibility of corrosion was included. This was modeled by replacing a thin outer shell of the nanowire by silver sulfide

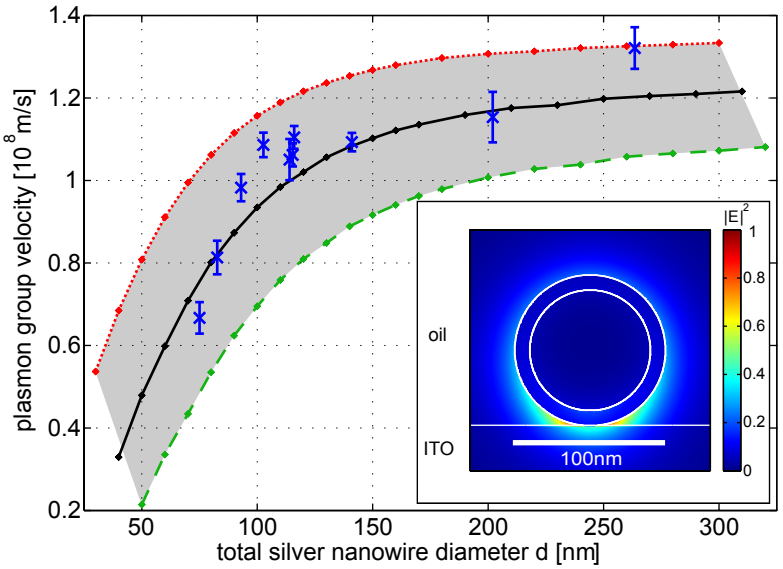

Figure 4.1: Plasmon group velocity as a function of the total silver nanowire diameter. Blue crosses indicate experimental results (error bars are calculated individually for each nanowire using the average separation time $\langle \Delta t \rangle$ and different measurement directions are averaged, cf. Section 3.5). Simulation results are represented by diamonds connected by lines. Results of simulations without corrosion layer, a 5 nm, and a 10 nm corrosion layer of silver sulfide are indicated with red dotted, black and green dashed lines, respectively. Inset: Fundamental plasmon mode profile for a silver nanowire in immersion oil on a 200 nm thick ITO layer on top of glass. The nanowire diameter is $d = 100$ nm including a 10 nm silver sulfide corrosion layer. Since the index mismatch between oil and ITO is small (cf. Appendix A.1) and because of the corrosion layer, the mode localization in the gap is less than in Fig. 2.10d (note the different scaling), which shows a nanowire in air on a glass substrate. Figure adapted from [Rewitz12b]. © (2011) American Chemical Society.

or silver oxide. The inset of Fig. 4.1 shows the simulated geometry and the modal profile of the fundamental propagating plasmon mode. Even though the nanowire is embedded in immersion oil, the environment is inhomogeneous since the refractive indices of oil and ITO differ (the oil matches the refractive index of the glass substrate). Therefore, the fundamental mode has quasi-TM character (cf. Section 2.4.3). The plasmon group velocity was obtained as the slope of the simulated dispersion relation of this fundamental mode at the laser pulse center wavelength of $\lambda_0 = 800$ nm.

The red dotted line in Fig. 4.1 indicates the simulated group velocities for pure silver nanowires, i.e., without a corrosion layer. The trend of the experimental results (blue crosses) is confirmed: Below $d = 100$ nm the plasmon velocity decreases strongly. However, the experimental data seem to systematically deviate towards lower group velocities. This behavior can be attributed to the influence of a thin silver sulfide corrosion layer as depicted in Fig. 4.1: The shaded area covers changes in the group velocity for up to 10 nm thick shells. The black and the dashed green lines indicate simulated group velocities for 5 nm and 10 nm thick silver sulfide shells, respectively. A silver oxide shell has a similar, although slightly less pronounced, effect due to its lower refractive index (cf. Appendix A.1). There are also other factors that could conceivably affect the plasmon mode and its properties. However, further

careful analysis of geometrical aberration influences, such as ellipticity or a (more realistic) pentagonal cross section of the nanowire [Ni05], ITO layer thickness and refractive index as well as uncertainties in the permittivity of silver [Laroche07], shows that a shell with a high refractive index is the only simulation parameter that yields good agreement of simulation and the experimental data.

The fundamental quasi-TM mode has been chosen for the simulation because it is expected to be the only mode with a sufficient propagation length to reach the output end of a nanowire. As discussed in Section 2.4.3, for sufficiently small nanowire diameters all other (higher-order) modes run into cut-off, i.e., they are damped out so quickly (purely imaginary propagation constant) that they do not propagate far enough to be experimentally detected. Much more costly full three-dimensional simulations (cf. Appendix A.1) of pulse propagation in a silver nanowire ($d = 100\,\mathrm{nm}$) that include the excitation geometry (polarization and focal-spot size) confirm that only the fundamental mode is excited and verify the group velocities determined by the two-dimensional simulations. The mode overlap of this mode with mode patterns obtained from the two-dimensional simulations is roughly 95%. Therefore, the assumption is confirmed that for the largest part of the data set indeed only one (fundamental) propagating mode is observed. However, for large nanowire diameters ($d \geq 200\,\mathrm{nm}$) simulations indicate the occurrence of a second mode with an even slightly higher group velocity and a larger propagation length than the fundamental mode. Such a mode with the intensity mostly localized at the upper side of the nanowire has been observed by others as well [Shegai11] and might explain the shift to higher propagation velocities of the experimental data point at $d = 263\,\mathrm{nm}$.

The three-dimensional simulations also confirmed that, as expected, any photon–plasmon conversion time is shorter than 1 fs, i.e., no linear spectral phase effects due to insertion or extraction at the nanowire ends have to be considered separately. Furthermore, incorporating such a (hypothetical) constant conversion time t_{conv} in the data evaluation and calculating the group velocity as $v = l/(t_{\mathrm{prop}} - t_{\mathrm{conv}})$, cf. Eq. (3.6), results in diameter dependent propagation velocities that do not follow the simulated trends (lines in Fig. 4.1).

In addition to measuring the group velocity, which is connected to the first-order Taylor coefficient of the spectral phase [Eq. (2.19)], the spectral-interference technique also allows to analyze higher-order phase terms, i.e., the dispersion of propagating plasmon pulses. However, as already discussed briefly in Section 3.3, in the case of silver nanowires the dispersion is very low, i.e., the plasmon pulse is not significantly broadened in the time domain while it propagates along the nanowire. An upper limit of the experimentally determined dispersion per propagation length is $50\,\mathrm{fs^2 rad^{-1} \mu m^{-1}}$ for all investigated nanowires. This is in good agreement with values obtained from the second derivative of the simulated dispersion relation.

Dependency on Local Environment

In order to experimentally determine the dependency on the local environment, the plasmon group velocity of a nanowire with a nominal diameter of $d = 100\,\mathrm{nm}$ was measured in two different surroundings: before and after adding the index-matched oil. In contrast to the previous experiments, the microscope cover slip used for this sample was not covered with an ITO layer. Therefore, in the case with oil immersion, the simulation incorporated a

	$v_{\mathrm{glass-air}}$ [10^8 m/s]	v_{glass} [10^8 m/s]
experiment	1.42 ± 0.03	1.14 ± 0.02
simulation	1.45	1.00

Table 4.1: Dependency of the plasmon group velocity on the local nanowire environment. Two cases, a nanowire on a glass substrate in air ($v_{\mathrm{glass-air}}$) and in an homogeneous glass surrounding (v_{glass}), are compared. The nominal diameter of the nanowire according to the manufacturer was $d = 100\,\mathrm{nm}$. The simulation geometry models the same diameter including a 5 nm silver sulfide corrosion layer. Since no ITO layer is present, the simulated value for v_{glass} differs from the one in Fig. 4.1.

homogeneous local environment with the refractive index of glass (fused silica). On the other hand, in the inhomogeneous case without oil, air was assumed in the upper half space. In fact, the fundamental mode profile and dispersion relation differ for both cases, as discussed in Section 2.4.3. Nevertheless, for each case the mode can be launched and characterized with the spectral-interference microscope.

The results are shown in Tab. 4.1. Experimental and simulated values agree reasonably well and emphasize the strong dependence of the plasmon group velocity on the local nanowire environment. The plasmon propagation is approximately 25% faster if the upper half space consists of air compared to the case of index-matched oil. This is in complete accordance with the simulated dispersion relations of Fig. 2.11. The inhomogeneous case with substrate (rectangles) is situated in between the homogeneous cases of air (open circles) and glass (crosses) surrounding, and the slopes of the dispersion relations at $\lambda_0 = 800\,\mathrm{nm}$, i.e. the group velocities, follow this trend. Even though the intensity in the inhomogeneous case is partly located in the substrate and in the air (cf. Fig. 2.10d), the dispersion relations confirm that only one single pulsed mode propagates along the nanowire (although one could think that each contribution propagates at a different speed). This is also confirmed by the experiments since only one dominant peak in the temporal emission envelope is detected.

4.3 Top-Down Gold Nanostructures

Since the silver nanowires are chemically grown, their size distribution cannot be controlled very well. Thus, the nanowires with varying diameter used in the last section had to be located by a search within a dispersed ensemble. Furthermore, each nanowire had a different length and structural uncertainties as the shape of the end facets influence the excitation and emission characteristics (cf. Section 2.4.4). Even though networks of these bottom-up silver nanowires have been used as first implementations of plasmon routers [Fang10] and logic gates [Wei11a, Wei11b], the variety of possible circuit designs naturally is limited. In contrast, top-down methods such as focused-ion-beam (FIB) milling have the advantage that almost arbitrary structures can be patterned into metallic films. However, evaporated metal films usually are multicrystalline and, hence, structural details and plasmon propagation are limited by grain boundaries. To overcome this limit, the work group of Bert Hecht[2] has developed

[2]Nano-Optics and Biophotonics Group, Experimentelle Physik 5, Universität Würzburg, Am Hubland, 97074 Würzburg, Germany

a technique to produce FIB-milled nanostructures for plasmonic nanocircuitry from single-crystalline gold flakes [Huang10]. The large ($> 100\,\mu m^2$) but thin ($< 80\,nm$) chemically grown gold flakes are immobilized on a desired substrate and the plasmonic structures are then patterned into the flakes by cutting away undesired gold with a focused gallium-ion beam. This fabrication technique results in "high-definition ultrasmooth gold nanostructures with superior optical properties and reproducible nanosized features over micrometer-length scales." [Huang10] In Chapter 5, a nanoscale directional coupler that was produced with this technique is used for control experiments. The structures investigated in this section—single nanowires and two-wire transmission lines—were produced by Peter Geisler[2] and Enno Krauss[2] from gold flakes deposited on microscope cover slips. After immobilization of the flakes, a 10 nm thick gold layer was evaporated on the cover slip to obtain electric contact of the sample and the SEM.

For the characterization of gold structures in the spectral-interference microscope, a slightly different data acquisition process compared to the one described in Section 3.3 is employed. First, the reference starting time is obtained from a reflection at an unstructured gold flake surface. This procedure is more reliable than using the reflection at the input end of a nanostructure since the spot profile of a gold flake reflection is independent on structural details of the plasmonic element. Hence, the spot is always undistorted, which often allows a more accurate definition of the excitation position and reference starting time compared to an input reflection (cf. Section 3.5). For silver nanowires such a reflection is not available. Second, the crossed-polarizer scheme is not used. Contrary to earlier expectations, it is not necessary to use the analyzer with its transmission axis oriented perpendicular to the input polarization in order to distinguish between the input reflection and the output emission. The spatial separation of both spots is sufficient for the discrimination. However, the analyzer has be used to define a common linear polarization between reference and signal for spectral interferometry. In the following, the analyzer is oriented parallel to the input polarization if not stated otherwise.

4.3.1 Single Nanowires: Dependency on Geometry

Since the gold nanostructures were used for the first time in pulsed propagation experiments, the primary goal was to verify the performance of the structures in the spectral-interference microscope (cf. Fig. 3.1) and determine the plasmon group velocities for single gold nanowires, the simplest possible geometry. A scanning electron micrograph of a gold nanowire sample is shown in Fig. 4.2a. As described above, the nanowires were cut out of a gold flake of which the remainders are visible at the borders of the image (gold shows up bright). Two sets of nanowires with different lengths are visible. In each set three different nanowire widths are available. The longer nanowires have a functionalization in form of a transverse cut at the left end, which should act as a simple input antenna for excitation light polarized along the nanowire.

Experimentally determined plasmon group velocities of gold single nanowires as a function of nanowire width are indicated with blue crosses in Fig. 4.2b. Since the crossed-polarizer scheme was not used, the excitation polarization was set parallel to the long axis of the nanowires in order to maximize the output emission and excite exclusively the fundamental quasi-TM mode (cf. Section 2.4.4). The gold single nanowires were used to study influences

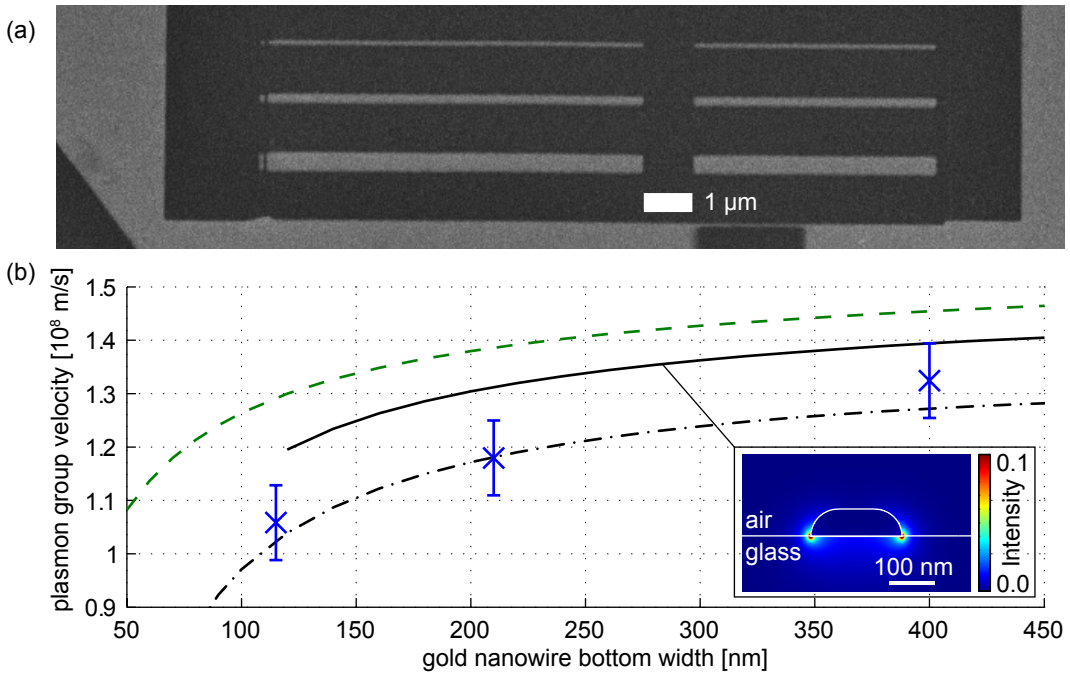

Figure 4.2: (a) Scanning electron micrograph of an example gold single nanowire sample. The nanowires were produced by focused-ion-beam (FIB) milling of a single-crystalline gold flake [Huang10]. Remainders of the flake are visible at the borders of the image. In spectral-interference microscopy measurements, the reference starting time of plasmons is determined by a reflection of the focal spot at such a flat gold surface. (b) Plasmon group velocity as a function of the gold nanowire bottom width. Blue crosses indicate experimental results (error bars indicate the typical value of $\Delta v = 0.07 \cdot 10^8 \mathrm{m/s}$, cf. Section 3.5). Simulation results (cf. Appendix A.1) for rectangular, trapezoidal, and the most realistic cross section with rounded upper corners (see inset) are represented by green dashed, black dashed dotted, and black lines, respectively.

of experimental procedure details, cf. [Goetz12] and Section 3.5. Therefore, several (partly different) plasmon group velocities were measured for each nanowire. Nevertheless, the values shown in Fig. 4.2b result from averaging over all available measurements of each nanowire and both nanowire lengths. The averaging over several measurements of one nanowire is motivated by a clear presentation of data and justified by the pronounced differences in width-dependent results, which is discussed in the following. Averaging over different lengths is justified by the fact that the functionalization of the longer nanowires has no impact on the group velocity (within the experimental error).

As expected from the silver nanowire results (cf. Fig. 4.1), also for the gold nanowires the velocity decreases with a reduced cross section and seems to saturate for larger widths. This can be also seen from the simulated results (cf. Appendix A.1) of the fundamental propagating mode (lines in Fig. 4.2b). The green dashed line illustrates results for a rectangular cross section of the gold nanowires. However, the cutting process in focused-ion-beam milling is not perfect. Detailed scanning electron and atomic force micrographs revealed that the top of the structures often is smaller than the bottom, which is attached to the substrate, because the beam waist of the focused ion beam is located at the substrate–gold interface.

Therefore, the black dashed-dotted line in Fig. 4.2b shows simulation results of a trapezoidal cross section (top width 80 nm smaller than bottom width) and the black line indicates the simulated dependence for the most realistic profile with rounded upper corners (radii of 60 nm, see inset). Similarly to the corrosion layer in the silver nanowire case (Section 4.2), these modifications of the simulation parameters yield reasonable agreement of simulation and experimental data.

In summary, single mode plasmon propagation in top-down gold nanowires was successfully investigated. In the next section, full advantage of the fabrication process is taken to produce more complex waveguides that support two modes and feature an input antenna as well as a so-called mode detector.

4.3.2 Two-Wire Transmission Lines: In Situ Analysis of Multimode Plasmons

A logical extension of the single-nanowire (Section 2.4.3) and the MIM/IMI concept (Section 2.4.2) is a two-wire transmission line (TWTL) consisting of two parallel metallic nanowires with a nanometer-sized dielectric gap between them [Krenz10, Schnell11]. Figure 4.3a shows a representative scanning electron micrograph of a 5 μm long TWTL with a linear dipole antenna at the left input end (circle) and a so-called mode detector at the right output end (ellipse). Both features are explained below. In analogy to the MIM and IMI structures, the hybridization of both single-wire fundamental modes gives rise to a symmetric (quasi-TM) and an antisymmetric (quasi-TE) eigenmode [Hung12, Geisler13]. Thus, TWTLs combine true subwavelength one-dimensional guiding of propagating optical near-fields with multimode operation. Single nanowires with similar dimensions only support one mode and the possible field confinement and enhancement is not as strong as in TWTLs. The symmetric eigenmode of a TWTL features a symmetric charge distribution across the gap and the near-field intensity is mostly located at the outer edges of the two nanowires (Fig. 4.3b). Hence, this eigenmode is similar to the fundamental mode of a single large-width nanowire without a gap. In contrast, the opposite charges across the gap for the antisymmetric eigenmode yield a near-field intensity that is highly confined within the gap (Fig. 4.3c). This eigenmode features a lower effective wavelength, a shorter propagation length, and a smaller plasmon group velocity compared to the symmetric eigenmode, which is consistent with the higher field confinement [Geisler13]. In experiments presented so far, only the antisymmetric mode is considered [Ly-Gagnon12, Krenz10, Schnell11].

For TWTLs, the efficiency of light in- and outcoupling can be tailored with optical antennas (cf. Section 2.4.4). In Fig. 4.3a a linear dipole antenna is attached to the left input end of the TWTL (circle). In fact, the Hecht group has shown within the collaboration mentioned at the beginning of this chapter that quantitative selective excitation of pure eigenmodes can be achieved by engineering the input-antenna geometry and using polarized excitation light focused on the center of the input antenna [Geisler13]. For a polarization parallel (perpendicular) to the transmission line the symmetric (antisymmetric) eigenmode is launched, as indicated in Figs. 4.3b,c. As a consequence, any other excitation polarization state creates a superposition of both eigenmodes.

In order to spatially separate the emission spot of each eigenmode, the TWTL in Fig. 4.3a features a so-called mode detector at its right output end (ellipse): The gap terminates

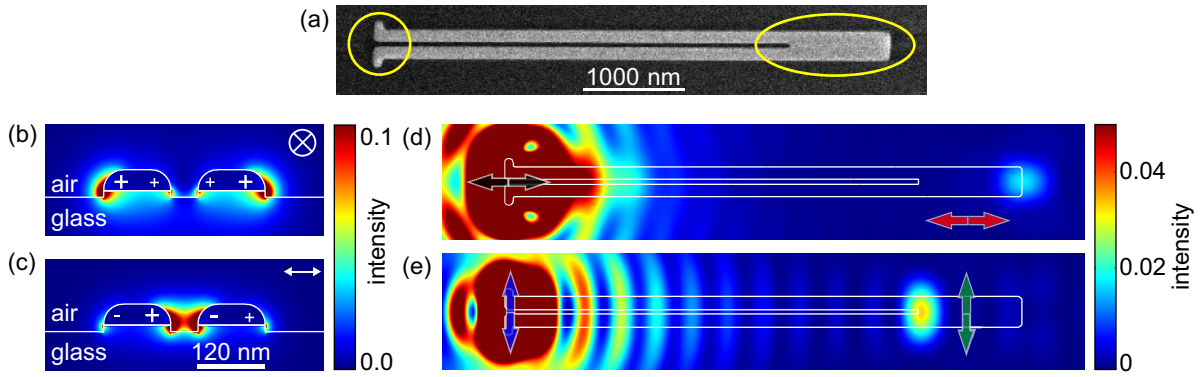

Figure 4.3: Two-wire transmission line eigenmodes and mode detector emission properties. (a) Scanning electron micrograph of a TWTL produced by focused-ion-beam milling. An input antenna is attached to the left side (circle) and a mode detector terminates the structure on the right side (ellipse). (b,c) The modal profiles (cf. Appendix A.1) for the symmetric (b) and antisymmetric (c) eigenmode of an infinitely long TWTL situated on glass elevations above a glass substrate are shown (the elevations are another approach to account for fabrication details, cf. Section 4.3.1). Instantaneous charge distributions are symbolized by "+" and "-" signs. (d,e) Simulated time-averaged far-field projections (cf. Appendix A.1) with a superimposed TWTL outline (white). Shown are the cases for a pure symmetric (d) and antisymmetric (e) mode propagating along the TWTL. The pure modes are excited by illumination of the incoupling antenna with focused light polarized parallel (d, black arrow) and perpendicular (e, blue arrow) to the transmission line. The emission of each mode is polarized along the input polarization (red and green arrow). The intensity scale is normalized to the reflected intensity at the glass–air interface. Figures adapted from [Geisler13]. © (2013) American Physical Society.

1 μm before the structure ends. Since the symmetric eigenmode has an intensity node in the gap, an ending of this gap does not affect it and it is reflected and radiated at a complete termination of the structure (far end). On the contrary, the antisymmetric eigenmode with its intensity maximum in the gap is reflected and radiated at the end of the gap. The spatially separated emission of each eigenmode can be seen in the simulated far-field images of Figs. 4.3d,e in which a focused laser beam polarized parallel (Fig. 4.3d, black arrow) and perpendicular (Fig. 4.3e, blue arrow) to the transmission line excites the symmetric and antisymmetric eigenmode, which are subsequently radiated at the far end and the gap termination, respectively. Importantly, the emission from the mode detector has the same polarization as the input as indicated by the red and green arrow for the symmetric and antisymmetric mode emission, respectively.

Experimental verification of the aspects mentioned above was accomplished by exciting such a TWTL with laser pulses that were linearly polarized at 45° with respect to the transmission line axis. For the correct input antenna size, this ensures excitation of a multimode plasmon pulse with equal intensity in both eigenmode contributions [Geisler13]. Since the linear excitation polarization in the spectral-interference microscope is fixed along the y axis in "emission scans" (cf. Figs. 3.4b,c), the structure is oriented along the cross diagonal in Fig. 4.4a (white outline) to implement the 45° excitation polarization. As expected, both emission spots in the mode detector area, which is located in the lower right corner (yellow

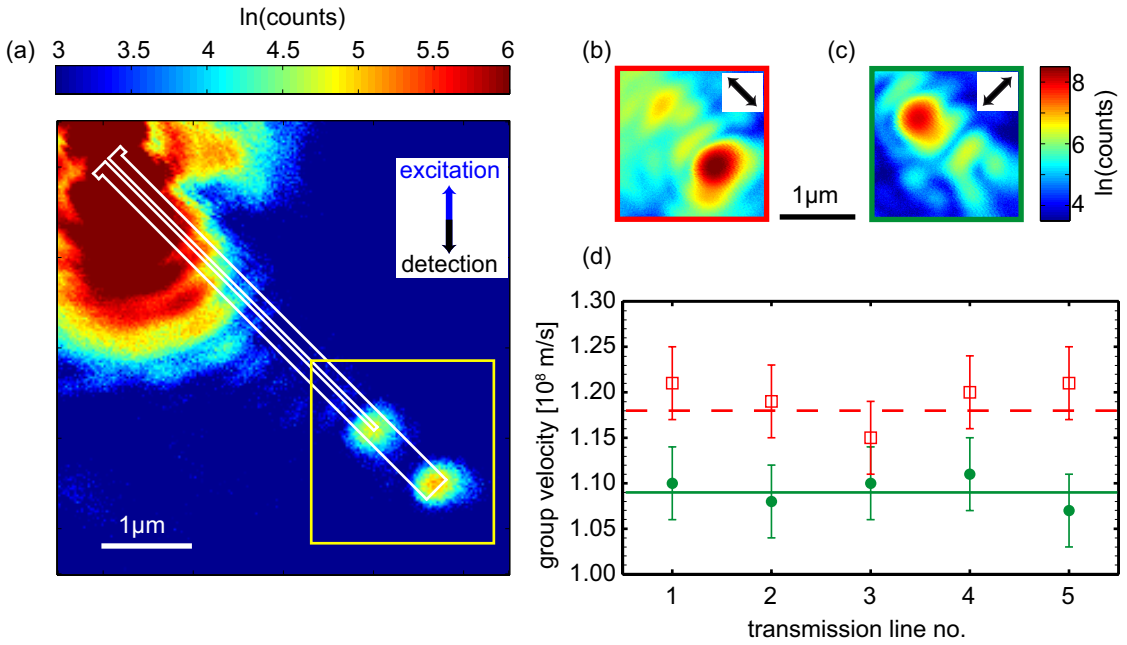

Figure 4.4: Multimode plasmon-pulse propagation experiment. (a) Shows an "emission scan" of a TWTL (white outline) excited with 45° polarized pulses at the input antenna (upper left). Since both modes are excited and the analyzer is oriented parallel to the excitation polarization (inset), both outputs of the mode detector (yellow rectangle) light up in the time-integrated intensity map. In contrast, only the far end lights up if the analyzer is oriented parallel to the transmission line (b, symmetric mode emission), whereas gap-end emission can be seen for an analyzer orientation perpendicular to the TWTL (c, antisymmetric mode emission). (d) Shows results of group velocity measurements for a set of five TWTLs with varying input-antenna lengths. Red squares (green circles) indicate the symmetric (antisymmetric) mode contributions (multiple measurements of each mode on each TWTL were averaged to improve accuracy). The results agree quantitatively with simulated values (dashed red line for symmetric mode, green line for antisymmetric mode). Panels (a-c) based on [Goetz12], panel (d) adapted from [Geisler13]. © (2013) American Physical Society.

square) of the time-averaged intensity map, light up with about equal intensities if the analyzer axis is oriented parallel to the input polarization (see inset). However, if the analyzer axis is rotated parallel to the transmission line, mainly emission from the far end of the structure is observed (Fig. 4.4b, high resolution image of mode detector area), which confirms that emission of the symmetric eigenmode is detected. On the other hand, for an analyzer orientation perpendicular to the TWTL (Fig. 4.4c, high resolution image of mode detector area) light emission is mostly observed at the gap termination, thereby indicating detection of the antisymmetric eigenmode emission.

Each contribution of the multimode plasmon pulse propagates with a certain group velocity along the transmission line. In time-averaged "emission scans", any temporal separation of emissions cannot be resolved. In order to illustrate the power of both—the nanostructure design and the spectral-interference microscope—group velocities of the symmetric and antisymmetric contribution of the multimode plasmon pulse have been determined selectively. To minimize the error in spectral phase reconstruction, the emission at each output was op-

timized by fine positioning the input antenna with respect to the excitation focus (using an automated routine) and subsequently recording the spectral interferometry signal at the optimized output. Nevertheless, both outputs were emitting intensity, thereby confirming that for each measurement position a multimode plasmon pulse was excited. The slightly different optimal excitation position for each eigenmode is attributed to fabrication imperfections of the nanostructure.

The results from multimode-plasmon group-velocity measurements of five TWTLs are illustrated in Fig. 4.4d with red open squares and green circles for the symmetric and antisymmetric mode contribution, respectively. Each transmission line has a different input-antenna length, which changes the excitation efficiency of each eigenmode. As expected, no systematic dependence of the group velocities on the antenna length is observed. However, the difference between the symmetric and antisymmetric mode is clearly resolved. The symmetric mode is 8 % faster than the antisymmetric mode. Furthermore, quantitative agreement between the experimental results within the error margin and simulated data is obtained, as can be inferred from the red dashed and green line that represent the simulated antisymmetric and symmetric plasmon group velocities for realistic structure geometries (cf. Fig. 4.3), respectively.

In summary, multimode plasmon pulse operation on two-wire transmission lines has been experimentally implemented and group velocities of different eigenmode contributions have been measured quantitatively. In the next step, the phase relation of these eigenmodes is employed to control plasmon propagation.

5 Control of Near-Field Propagation in a Nanocircuit

Up to here, this dissertation dealt with far-field characterization of propagating optical near fields. In Chapter 3 the experimental technique of spectral-interference microscopy was introduced and Chapter 4 included the *in situ* analysis of multimode plasmon pulses on two-wire transmission-lines. In the current chapter, both—the experimental technique and the nanostructures—are developed further in order to achieve control of propagating optical near fields. First, enhancements of the setup necessary for control experiments are discussed (Section 5.2). Next, the design of a nanoscale directional coupler is introduced and simulated manipulation of near-field propagation is shown (Section 5.3). Then, experimental results on single pulse routing and spatiotemporal control are presented (Section 5.4). On top of that, alternating routing is performed (Section 5.5), before the potential of polarization-shaped laser pulses is illustrated (Section 5.6).

The work presented in the current chapter resulted from the same collaboration that is described in Chapter 4. Again, the Hecht group provided near-field simulation data and gold nanostructures. Furthermore, the experimental idea was conceived in the regular meetings and all data was discussed.

Parts of this chapter have been published in [Rewitz14].

5.1 Introduction

In the field of plasmonics, nanooptical elements with well-defined built-in passive functionality [Ozbay06, Gramotnev10] such as splitting or filtering [Bozhevolnyi06] have been presented. Furthermore, active coherent control of femtosecond optical energy localization in nanoscale random structures and V-shapes [Stockman02] as well as coherent control of plasmon routing has been proposed [Sukharev06, Tuchscherer09]. Control of nonpropagating near-fields was achieved experimentally [Aeschlimann07, Aeschlimann10].

In all these coherent (nanooptical) control schemes a far-field laser pulse—determined by its spectral amplitude, phase, and polarization—excites a particular superposition of near-field modes, which then evolves into a desired state, e.g., a local field enhanced by orders of magnitude [Stockman02]. Mathematically, the local electric field in the frequency domain

$$\vec{E}_{\text{local}}(\vec{r},\omega) = \mathbf{A}(\vec{r},\omega)\vec{E}_{\text{ext}}(\omega) \tag{5.1}$$

depends on both, the tensorial linear response function of the (nano-)system $\mathbf{A}(\vec{r},\omega)$ and the external field $\vec{E}_{\text{ext}}(\omega)$ [Tuchscherer09]. Usually, the response function is fixed and control is exerted by manipulating the above mentioned coherent properties of the excitation light to influence the interference of the available near-field modes [Rewitz09, Tuchscherer12]. This

often yields very complex excitation pulse shapes $\vec{E}_{\text{ext}}(t)$ in the time domain [cf. Eq. (2.10)], which have to be determined with closed-loop learning algorithms in the experimental implementations [Aeschlimann07, Aeschlimann10].

In the current chapter, a different approach is employed to coherently control propagating optical near fields. Not the optimal $\vec{E}_{\text{ext}}(t)$ is tried to be obtained for a given system but rather the system response $\mathbf{A}(\vec{r},\omega)$ is designed so that a given control field yields the desired result. Routing of plasmons is then based on the controlled interference of multiple well-known propagating modes that exist in the designed system, similar to concepts used in dielectric waveguides for diffraction-limited routing of optical energy [Liu05]. In contrast to closed-loop experiments that use networks of chemically grown silver nanowires [Fang10, Li11, Wei11a, Wei11b, Singh12, Wei12] or slot-less gold nanostructures [Könenkamp12] for the manipulation of plasmon propagation, quantitative selective excitation of at least two well-defined propagating eigenmodes, as discussed in the preceding chapter, is a fundamental requirement for this controlled interference.

In the next sections, it is shown that it is possible to design, simulate, fabricate, and experimentally characterize a plasmonic nanoscale directional coupler, i.e., a nanocircuit with a single input port and two output ports, in which efficient ultrafast coherent control of propagating optical fields that are confined below the diffraction limit is achieved with the simplest possible control field. Due to the intuitive design of the nanocircuit, which is based on a two-wire transmission line with input antenna and mode detector (cf. Section 4.3.2), varying the linear polarization of the excitation light is sufficient to route plasmons and, thus, the use of closed-loop learning algorithms is avoided.

In contrast to classical electronic circuits, where a symmetric bifurcation inevitably causes an equal splitting of any input current pulse towards the two output ports, a fundamentally different behavior is induced in the plasmonic nanoscale directional coupler by exploiting the existence of multiple eigenmodes and coherence—both not accessible in classical electronics. Therefore, the potential and importance of optical control in the design and operation of plasmonic nanocircuitry is demonstrated.

5.2 Setup Enhancements

As mentioned briefly at the end of the last chapter and in the previous section, control in the nanoscale directional coupler relies on active polarization and phase manipulation of the input field. Therefore, the experimental setup was enhanced by a Mach–Zehnder delay line (Fig. 5.1, dashed frame) to produce two collinearly propagating pulses. The polarization in one arm of the delay line is rotated by 90° using a half-wave plate (green) in combination with an x polarizer (yellow). The optical path length in the other arm can be controlled with a piezo stage to adjust the temporal separation $\Delta\tau$ between both pulses. It was carefully checked that both pulses have the same focal size, focal position, and excitation power in the sample plane. Hence, two orthogonally polarized excitation pulses, termed x-polarized and y-polarized, according to the orientation in "emission scans", with an arbitrary temporal separation can be generated. This includes the possibility of temporal overlap, yielding more complex temporal polarization patterns. In the temporal overlap region the polarization state depends on the relative phase $\Delta\Phi$ between the two pulses. If the relative phase is, e.g., scanned from $\Delta\Phi = 0$

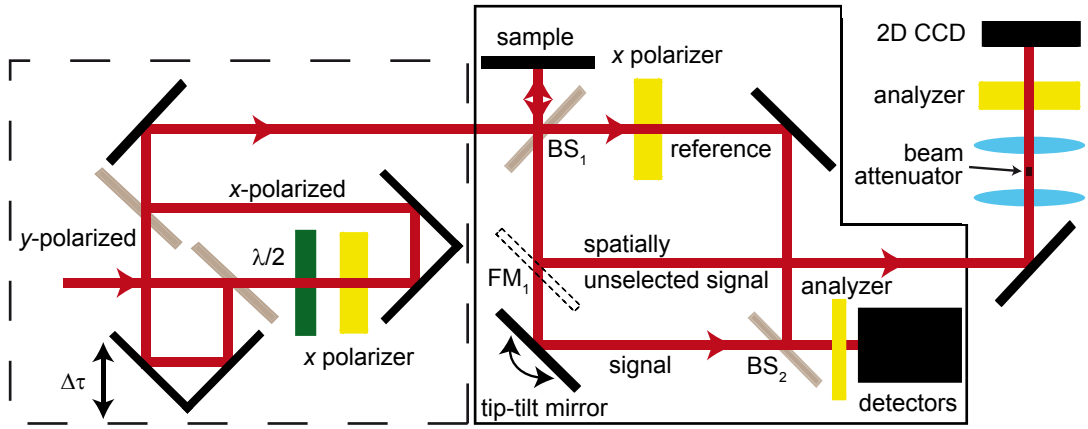

Figure 5.1: Setup enhancements for control experiments. In one arm of the Mach–Zehnder delay line (dashed frame), the polarization of the pulse is rotated by a half-wave plate (green). Together with an x polarizer (yellow), matching of both pulses' excitation power in the sample plane is possible. The optical path length of the other arm can be adjusted with a piezo stage to manipulate the separation $\Delta\tau$ of both excitation pulses. The spectral-interference microscope (solid frame) is sketched with important elements only. See Fig. 3.2 for a detailed schematic. Compared to this schematic the first beam splitter (BS_1) is exchanged and transmits 20% (50%) of the intensity in x (y) polarization. An x polarizer is located behind this beam splitter to ensure the existence of only one reference pulse, which is derived from the arm of the Mach–Zehnder delay line with constant optical path length. On the detection side (outside of frames), a two-dimensional charge-coupled-device (CCD) camera can be employed to image the sample in one shot. In this case, the spatially unselected signal of the spectral-interference microscope is used and a precisely situated beam attenuator in the focal plane of a Keplerian telescope suppresses strong reflections and scattering of the excitation spot.

to $\pi/2$, the resulting polarization state changes from linear (at 45°) over elliptical (with the principle axis still at 45°), to circular. Using the delay line, the separation of the two pulses can be controlled with 0.1 fs accuracy (experimentally determined via spectral-interference measurements). This corresponds to a relative path-length difference of 30 nm, or a relative phase of $\Delta\Phi = 0.075\pi$ at 800 nm wavelength. Therefore, precise manipulation of the relative phase between both pulses, i.e., the polarization state of the excitation field is feasible. Compared to polarization pulse shaping based on a zero-dispersion compressor and spatial light modulator [Brixner01b], the Mach–Zehnder setup avoids complications originating from space–time coupling [Wefers96, Frei09, Brinks11] that become especially relevant with high-NA focusing and excitation position sensitivity. The experimentally observed control effects (Sections 5.4 to 5.6) are, therefore, indeed due to spectral phase properties only and not due to spatially modified excitation.

In addition to the "emission scan" option that uses the piezo tip-tilt mirror for image formation (Section 3.3), the setup was further enhanced by a two-dimensional charge-coupled-device (CCD) camera in order to image the sample without the need of raster scanning. When using this visualization option, the piezo tip-tilt mirror is bypassed (Fig. 5.1, spatially unselected signal) and the image is relayed via a Keplerian telescope. This telescope adjusts the image size on the CCD chip and allows to insert a circular beam attenuator (optical

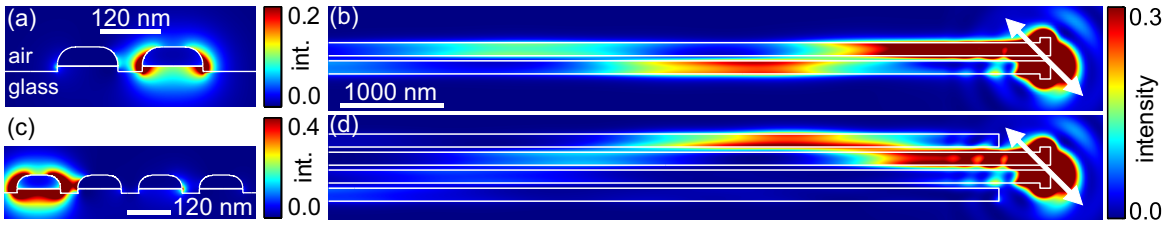

Figure 5.2: (a,c) Calculated modal profiles and (b,d) time-averaged near-field intensity distributions, cf. Appendix A.1. (a) The superposition of both eigenmodes of a two-wire transmission line yields an asymmetric profile. (b) For $+45°$ polarized light (white arrow) focused at the optimized incoupling antenna, such a superposition of the symmetric and antisymmetric eigenmode is created. As both modes travel along the transmission line their relative phase changes and the interference gives rise to a beating pattern along the propagation direction. (c) Similar to the two-wire case in (a), the modal profile of a four-wire transmission line, which supports four eigenmodes, can also be asymmetric. (d) For a four-wire transmission with identical excitation as in (b) a similar beating pattern as in the two-wire case can be observed: Starting from the input antenna, the near-field intensity first oscillates to the topmost (high intensity) and then to the lowest wire (damped intensity). The near fields in (b,d) are recorded in a plane 10 nm below the glass–air interface on which the nanostructures are situated. Panels (b) and (d) adapted from [Rewitz14].

density of 2) in the focal plane that suppresses most of the strong reflection and scattering of the excitation spot at the input end of the nanostructure.

In all experiments an analyzer with its transmission axis oriented perpendicularly to the symmetry axis of the designed nanostructure is used. Thus, only the dominating emission of the antisymmetric mode at the output ports is detected (cf. Fig. 4.3e and next section).

5.3 The Nanoscale Directional Coupler: Design, Simulation and Fabrication

The nanocircuit used in this chapter is based on the two-wire transmission line that was introduced in Section 4.3.2. As discussed in this section, pure eigenmodes of such a two-wire transmission line can be excited with equal amplitude if an appropriate incoupling antenna is attached to it and is illuminated by a well-positioned linearly polarized laser spot. For a focused laser beam positioned on the center of the incoupling antenna, the symmetric mode is excited if the polarization is parallel to the transmission line, whereas the antisymmetric mode is launched with perpendicular polarization (cf. Figs. 4.3b-e). Consequently, for any other polarization state of the input field a coherent superposition of both eigenmodes is created and the initial phase difference between both eigenmodes depends on the input polarization. For such a superposition, the modal profile can be asymmetric as shown in Fig. 5.2a. Here, both eigenmodes are superimposed with a phase difference of π, which leads to a localization of the near-field intensity at the right wire. Accordingly, the near-field intensity is localized at the left wire if the phase difference is zero.

As both modes propagate along the transmission line, their relative phase changes due to the different effective wavelengths of the symmetric and the antisymmetric eigenmodes ($\lambda_{\mathrm{eff}}^{\mathrm{sym}}$

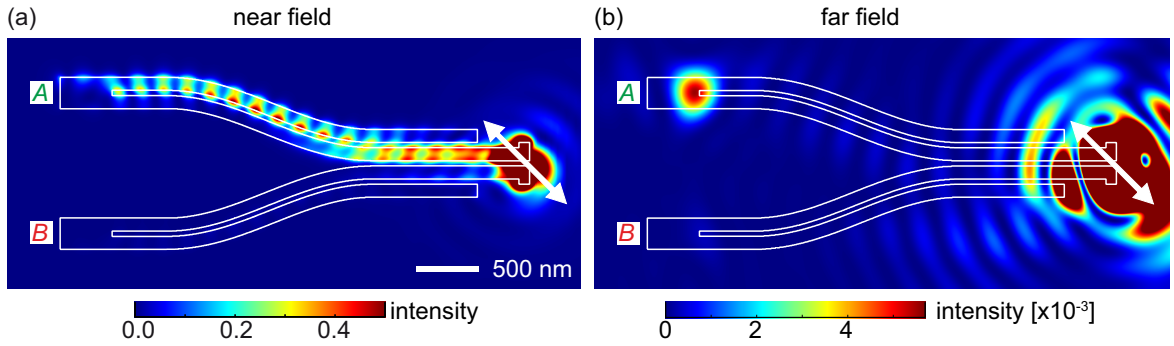

Figure 5.3: The nanoscale directional coupler: near-field and far-field simulations (cf. Appendices A.1 and A.5). (a) The simulated steady-state near-field intensity distribution in a plane 10 nm below the glass–air interface for excitation with +45° input polarization (white arrow) demonstrates routing to the upper branch of the directional coupler. The standing wave pattern is due to reflection at the termination. (b) In the corresponding far-field projection only output port *A* lights up. Figures adapted from [Rewitz14].

$= 517$ nm and $\lambda_{\text{eff}}^{\text{antisym}} = 471$ nm, respectively, for 800 nm vacuum wavelength). Thus, a beating pattern is formed along the propagation direction. Figure 5.2b shows the simulated S-like near-field intensity distribution obtained for a +45° polarized excitation (white arrow) focused on the optimized incoupling antenna at the right end. An alternative approach for the explanation of this beating pattern is to consider the two-wire transmission line as two strongly coupled single-wire waveguides supporting identical modes [Gramotnev08, Kriesch13]. However, for the two-wire transmission line with an optimized incoupling antenna, the phase of the beating pattern and, thereby, the position of field maxima and minima, can be controlled by the polarization of the excitation light. In the following this observation is used for the design of the nanocircuit.

In order to realize a branching region for the two-wire transmission line and to achieve phase-sensitive directional coupling, two additional wires are added on both sides of the two-wire transmission line. These four wires then split up to form a set of two uncoupled parallel two-wire transmission lines, each of them being terminated with a mode detector (cf. Section 4.3.2). This creates a nanoscale directional coupler that supports the same eigenmodes at its single input and two output ports. The four-wire region supports four eigenmodes. Similar to the two-wire case, localization at a single (outermost) wire occurs for a specific phase-sensitive combination of these modes (Fig. 5.2c).

To illustrate the principle of directional control in the designed nanoscale coupler, in Fig. 5.2d the evolution of the beating pattern into the four-wire region is shown for the case of +45° input polarization. After about 2300 nm propagation a maximum appears at the topmost wire. According to the goal of simple rather than complex control fields, this observation is exploited to optimize the geometry of the nanoscale directional coupler such that a 45° linear input polarization results in emission of light at one output port only. Details about this optimization can be found in Appendix A.5.

Figure 5.3a displays the resulting simulated near-field intensity distribution for excitation of such an optimized nanoscale directional coupler with +45° polarized light. Indeed, the near-field intensity is successfully routed to the upper branch. Thus, only output port *A* lights up

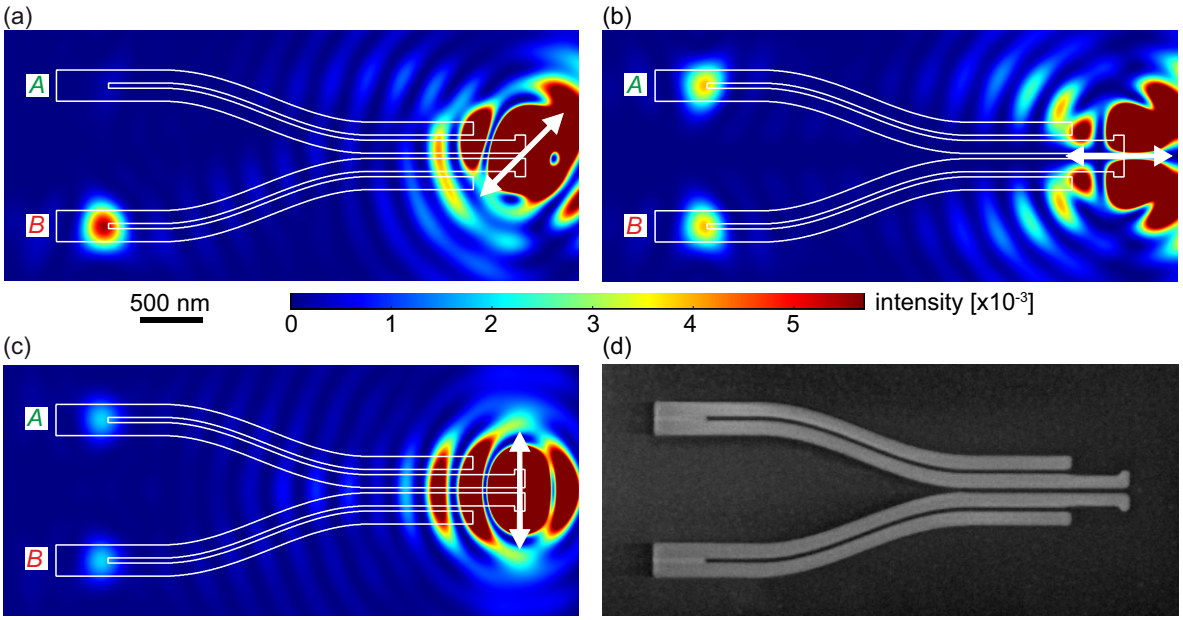

Figure 5.4: (a-c) Simulated far-field projections (cf. Appendices A.1 and A.5). (a) Compared to Fig. 5.3b, the -45° input polarization (white arrow) demonstrates switching of the routed signal to output port *B*. (b,c) For excitation polarizations parallel (b) and orthogonal (c) to the symmetry axis of the directional coupler the energy is split equally at the branching position and identical far-field intensities at both output ports are obtained since pure eigenmodes are excited. (d) A representative scanning electron micrograph shows the complete nanoscale directional coupler fabricated by focused-ion-beam milling [Huang10]. Figures adapted from [Rewitz14].

in the simulated far-field image (Fig. 5.3b). Due to the symmetry of the nanostructure only output port *B* emits light for an input polarization of $-45°$ (Fig. 5.4a). If, on the other hand, the input polarization is parallel or perpendicular to the symmetry axis of the nanostructure, i.e., only a single eigenmode is excited, the plasmonic energy splits up equally to the two branches and both output ports light up simultaneously and with identical intensity (Figs. 5.4b and 5.4c, respectively). Note that beyond the branching region, the modal composition of the propagating optical near field is dominated by the antisymmetric mode (cf. Fig. 5.3a), which is localized in the gap and, therefore, radiates at the gap-end of the nanostructure (cf. Figs. 5.3b and 4.3e).

The spectral behavior of the nanocircuit is discussed in Appendix A.6. As all gold nanostructures described in this dissertation, the nanoscale directional coupler is fabricated by focused-ion-beam (FIB) milling from a single-crystalline gold flake deposited on a microscope glass cover slip [Huang10]. Figure 5.4d shows a representative scanning electron micrograph of the nanocircuit.

5.4 Single-Pulse Routing and Spatiotemporal Control

Single-Pulse Routing

To experimentally demonstrate single-pulse routing for the designed nanoscale directional coupler, the cover slip with the nanocircuit was mounted onto the enhanced spectral-interference microscope so that the symmetry axis coincided with the diagonal of the coordinate system spanned by the two orthogonal polarizations. In this configuration an x-polarized pulse is expected to excite the superposition of eigenmodes that leads to far-field emission only at output port A (Fig. 5.5a). On the other hand, excitation with the y-polarized pulse should route the plasmons to output port B (Fig. 5.5b).

Figures 5.5c and 5.5d show "emission scans" recorded around the output port region of the nanoscale directional coupler. As predicted, only output port A emits light for the x-polarized excitation (Fig. 5.5c), while only output port B lights up for a y-polarized excitation pulse (Fig. 5.5d). To quantify the control performance the spatial contrast, sc, is defined as

$$\mathrm{sc} = \frac{E(A) - E(B)}{E(A) + E(B)}, \tag{5.2}$$

where the emitted energy E in each output port is determined by the background-corrected integral in $1 \times 1\,\mu\mathrm{m}^2$ regions as indicated by the yellow squares in Figs. 5.5c,d. In the experiments, $\mathrm{sc} = 0.79$ and $\mathrm{sc} = -0.88$ are obtained for x- and y-polarized excitation pulses, respectively.

It is important to note that even though in these experiments spectrally broad ultrashort laser pulses are used, for which the beating wavelength (cf. Fig. 5.2b) varies across the spectrum, these spatial contrast values are very close to $\mathrm{sc}_{\mathrm{sim}} = \pm 0.90$ obtained from the simulations for the design wavelength of 800 nm (cf. Appendix A.6).

Therefore, the experiment successfully implements coherent control over plasmon propagation for a system in which the light-matter interaction responsible for the control is spatially separated from the decisive branching region, as first proposed by Sukharev and Seideman [Sukharev06]. As discussed in Section 5.1, the response function $\mathbf{A}(\vec{r}, \omega)$ in coherent control schemes is usually fixed and control is exerted by manipulating the coherent properties of the excitation light, i.e., amplitude, phase, and polarization. For instance, in the prototype quantum control problem for chemical reactions [Assion98], a complex external electric field $\vec{E}_{\mathrm{ext}}(t)$ is required that excites a particular wavepacket, which preferentially evolves from the initial state into a selected final state. In the case studied here, an appropriate coherent control field yields surface plasmon polariton propagation to a selected output port. Therefore, the experiment is a very intuitive classical analogue to quantum control, even though, here, the system response $\mathbf{A}(\vec{r}, \omega)$ was designed such that a given control field (varying linear polarization) yields the desired result (cf. Section 5.3). Thus, the simple pulse shape that leads to control is not a sign of an incoherent control scheme but it is rather a specific feature that was implemented.

Furthermore, it should be noted that although the behavior of the directional coupler appears to be similar to that of a polarizing beam splitter, the physics behind it is different since it involves coherent electron plasma oscillations. The deceptively simple, polarizer-like behavior only occurs due to the specific design of both the incoupling antenna as well as the

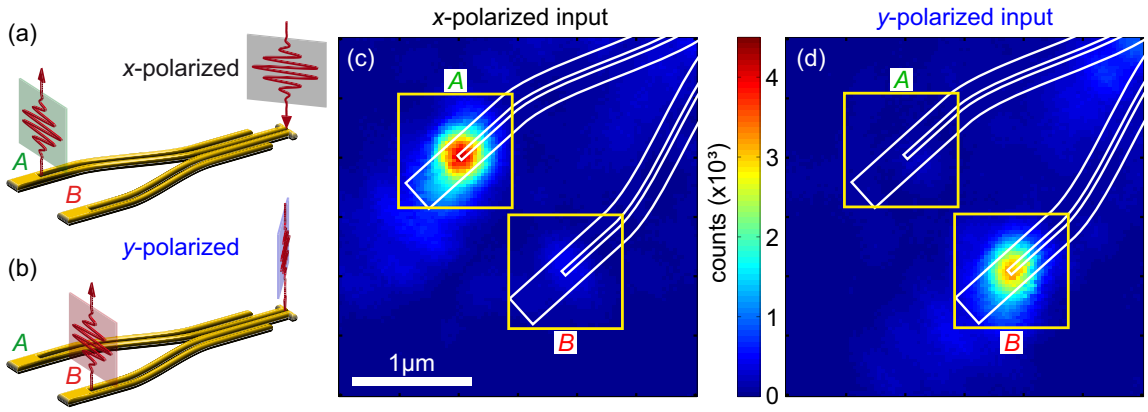

Figure 5.5: Single-pulse routing. (a,b) Sketches show the routing of plasmon pulses for *x*-polarized (a) and *y*-polarized (b) excitation pulses. (c,d) Spatial maps show the measured time-integrated sample emission ("emission scans") upon excitation with the *x*-polarized (c) and *y*-polarized (d) pulse. Due to the orientation of the directional coupler (white outline), the *x*-polarized pulse constitutes the +45° polarization and causes routing to output port *A* (c). The *y*-polarized pulse represents the -45° polarization and results in routing of the plasmon pulse to output port *B* (d). Figures adapted from [Rewitz14].

length of the four-wire coupling region of the nanocircuit. For example, by an appropriate choice of the four-wire coupling region length, routing with right versus left circularly polarized light could be obtained easily. By additionally detuning the antenna, and thereby the weight of both eigenmodes, corresponding elliptical polarization states would be required as input fields.

Spatiotemporal Control

Now, the discussion proceeds to the manipulation of temporal light emission evolution in each output port. So far, the nanostructure was excited either by the *x*- or the *y*-polarized pulse. If pulses of both polarizations are incident with a fixed time delay, both output ports emit light successively (Fig. 5.6a). The result of the experimental implementation is shown in Fig. 5.6b, where the time-integrated spatial map of the output region shows that both output ports of the nanostructure light up.

The time delay between the emission of both outputs is not resolved in such a time-integrated "emission scan", but spectral-interference microscopy (cf. Chapter 3) provides a way to experimentally characterize it. Figure 5.6c shows the reconstructed temporal envelope of the signal in output port *A* (green solid) together with that in output port *B* (red dashed). The temporal signature corresponds to the scheme of Fig. 5.6a and confirms that the light at the two output ports is indeed emitted successively. In the case shown here, the *y*-polarized excitation pulse arrives later than the *x*-polarized excitation pulse at the input port. This can be inferred from the temporal envelopes of the *x*- (black solid) and the *y*-polarized (blue dashed) input pulses (Fig. 5.6d) that were measured using the reflections from an unstructured gold flake (cf. Section 4.3). The temporal separation of their maxima ($\Delta\tau = 210\,\mathrm{fs}$) indicates the starting time difference of the plasmons launched by the respective

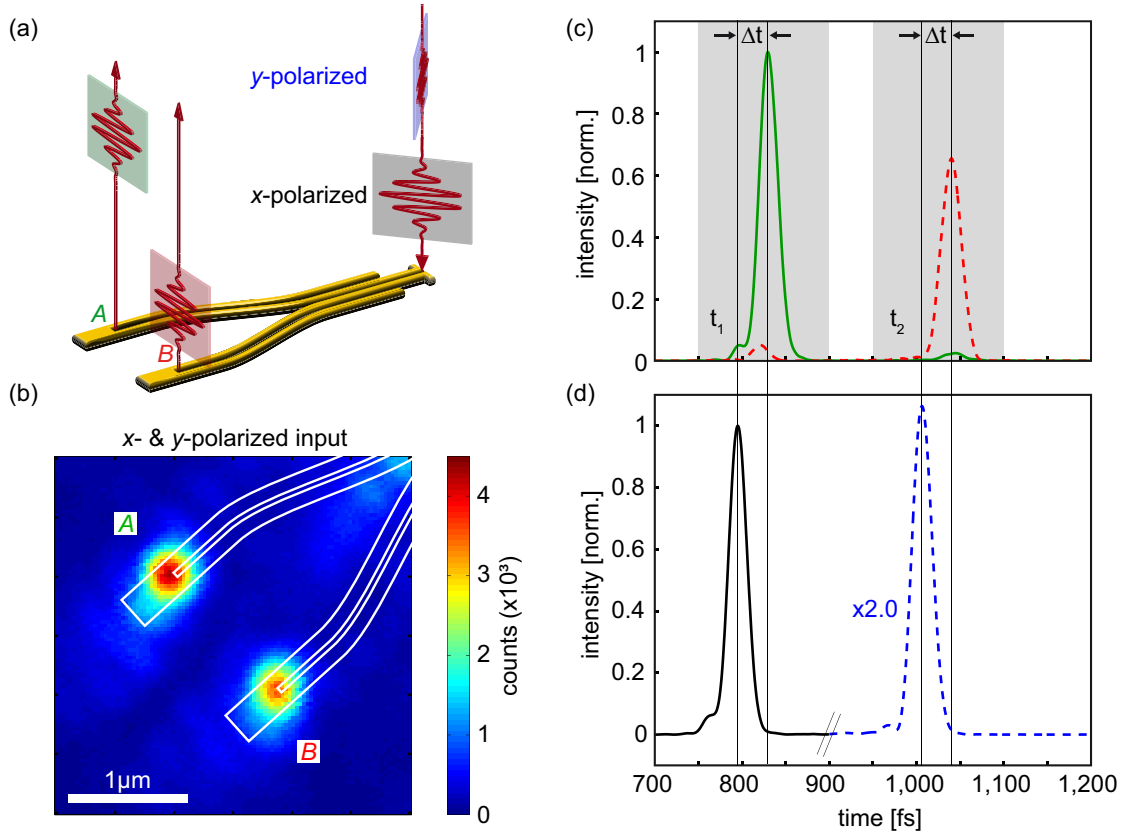

Figure 5.6: Spatiotemporal control. (a) Two orthogonally polarized excitation pulses are incident on the nanostructure with a temporal delay leading to the emission of separate pulses at each output port at different times. (b) The spatial map of measured time-integrated sample emission ("emission scan") shows light emission from both output ports, as expected. (c) The reconstructed temporal envelopes of emission in output port A (green solid) and B (red dashed) indicate the arrival time of each signal pulse. (d) The reconstructed temporal envelope of the input field shows two peaks. The time trace below 900 fs (black solid) represents the x-polarized pulse, whereas the part above 900 fs (blue dashed) is attributed to the y-polarized pulse. The contribution above 900 fs was multiplied by a factor of 2.0 to account for the polarization-dependent transfer function from the sample plane to the detectors (i.e., the ratio of separately measured integrated spectra). In this measurement, the x-polarized pulse was delayed by 800 fs with respect to the reference pulse (cf. Section 3.2). Figures adapted from [Rewitz14].

pulses. Since the plasmons propagate with a certain group velocity from the input port to the output ports (cf. Chapter 4), the signals in output port A (Fig. 5.6c, green solid) and B (Fig. 5.6c, red dashed) both peak at a time $\Delta t = 34$ fs after the maxima of the respective launching pulses. Due to the symmetry of the nanoscale directional coupler the value of Δt is the same for both output ports. The PD-PAT correction for this measurement is $t_{\mathrm{corr}} = 0.5$ fs and, thus, the measured propagation time [$t_{\mathrm{prop}} = \Delta t + t_{\mathrm{corr}}$, Eq. (3.5)] is in good agreement with the simulated value of $t_{\mathrm{prop}}^{\mathrm{sim}} = 30$ fs, considering fabrication uncertainties and the inaccuracy of the measured separation time Δt (cf. Section 3.5).

To quantify the control performance, the temporal contrast, tc, for a given output port is

defined as

$$\mathrm{tc} = \frac{\hat{E}(t_1) - \hat{E}(t_2)}{\hat{E}(t_1) + \hat{E}(t_2)}, \tag{5.3}$$

where the energy $\hat{E}(t_i)$ is the integral under the green solid (output port A) or red dashed (output port B) curve in the respective shaded areas in Fig. 5.6c. The obtained values are $\mathrm{tc} = 0.94$ for output port A and $\mathrm{tc} = -0.86$ for output port B. These values confirm the successful implementation of spatiotemporal control. Note that the temporal separation of the excitation pulses can be adjusted at will so that almost arbitrary temporal sequential routing of plasmon pulses is possible with femtosecond resolution. This would allow ultrafast pump–probe experiments with nanometer resolution [Brixner05].

Sensitivity to Excitation Position

Apart from the input polarization, the excitation efficiency of each eigenmode also depends on the exact position of the focus [Geisler13]. In particular, it is possible to excite the symmetry-forbidden mode for each polarization by displacing the focus by less than half of its size from the antenna gap. The antenna of the nanoscale directional coupler is designed in such a way that both eigenmodes are excited with similar efficiencies (cf. Appendix A.5). In the ideal case this means that equal intensities of the input polarizations yield equal intensities of the eigenmodes if the focus is placed at the antenna gap. Thus, for the experiments on single-pulse routing and spatiotemporal control (Figs. 5.5 and 5.6, respectively), the spatial contrast should be best for an excitation with $\pm 45^\circ$ polarized pulses at this excitation position. However, the fabrication process is not perfect and it is difficult to orient the symmetry axis of the nanocircuit precisely along the diagonal of the images. Therefore, similar to the experiments in Section 4.3.2, an excitation spot position for each polarization was found separately by maximizing the emitted energy E at the respective output port using an automated routine. Then, a position exactly in between was chosen for the shown experiments, which remained constant during the experiments. In particular, it was constant between the measurements in Figs. 5.5c and 5.5d.

5.5 Alternating Routing

So far, the two orthogonally polarized excitation pulses were well separated in time and each linearly polarized laser pulse excited a coherent superposition of near-field modes by itself. Now, the reference frame is changed by reorienting the nanoscale directional coupler so that the x polarization is parallel to its symmetry axis (Fig. 5.7a). In this case, each far-field polarization separately excites the corresponding pure eigenmode (symmetric for the x polarization and antisymmetric for the y polarization). By design this leads to equal splitting of each eigenmode's intensity towards the two output ports of the nanoscale directional coupler. As a result, each polarization causes simultaneous emission at both output ports with equal intensity (cf. Figs. 5.4b,c).

Thus, if the excitation pulses are well separated in time, both output ports emit a corresponding pair of pulses (Fig. 5.7a). In time-integrated measurements this case cannot be distinguished from the case of Fig. 5.6, where each output port emits a single pulse (but

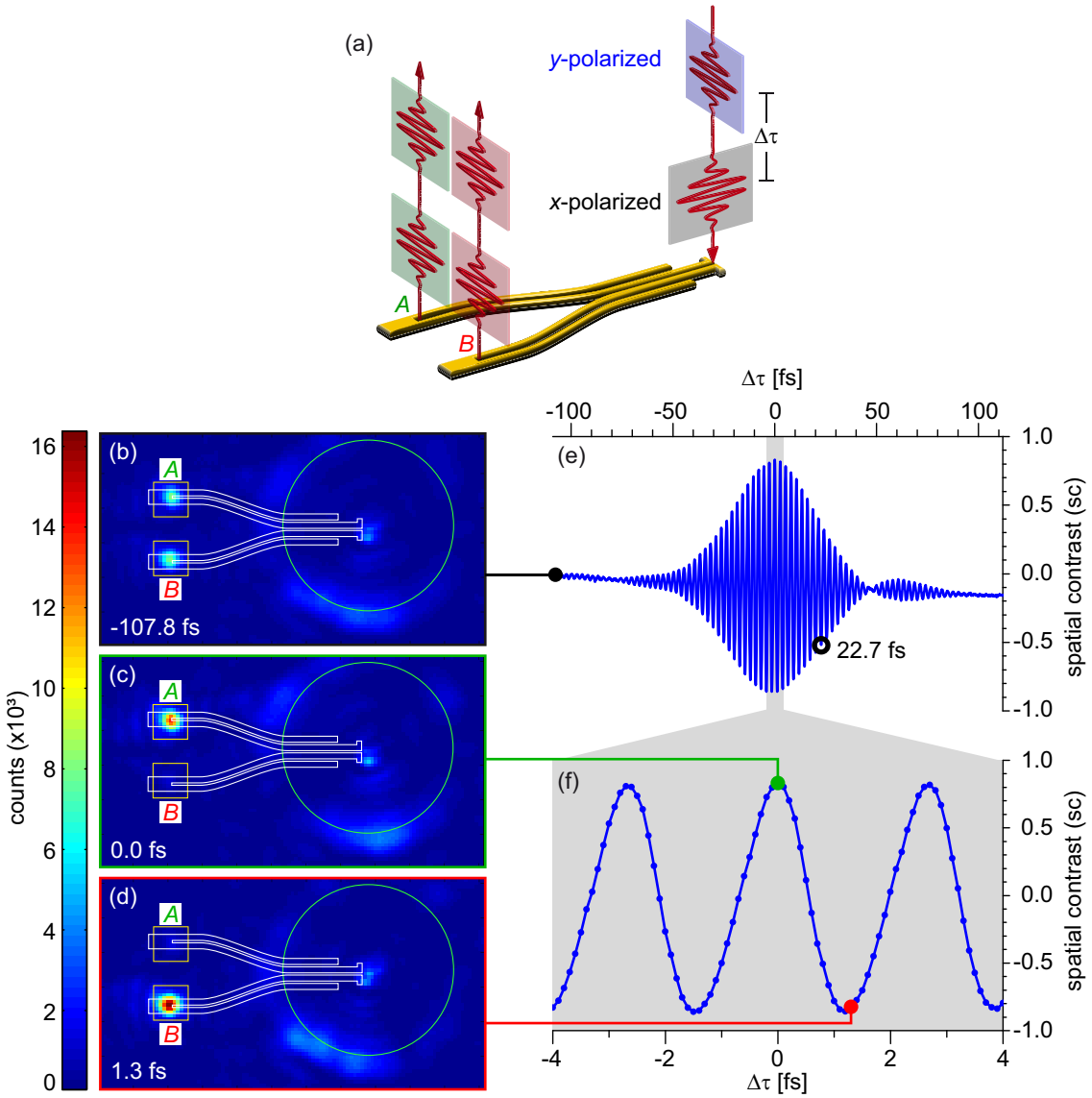

Figure 5.7: Alternating routing. (a) The sketched excitation scheme indicates a changed reference frame in which the x-polarized pulse is parallel to the symmetry axis of the directional coupler. (b,c,d) Spatial maps show the measured time-integrated sample emission (using the two-dimensional CCD, cf. Section 5.2) at different temporal separations $\Delta\tau$ of the two excitation pulses. Superimposed are outlines of the nanostructure (white) and of the circular beam attenuator (green, cf. Section 5.2), which suppresses most of the excitation spot reflection and scattering. (b) For excitation pulses well separated in time ($\Delta\tau = -107.8\,\mathrm{fs}$) both output ports emit about the same intensity. (c) At $\Delta\tau = 0.0\,\mathrm{fs}$ the pulse exits the directional coupler at output port A, while at $\Delta\tau = 1.3\,\mathrm{fs}$ the pulse is routed towards output port B (d). (e,f) The spatial contrast curve [cf. Eq. (5.2)] as a function of the time delay (e) and a zoom into the temporal overlap region (f) are depicted. The position of the spatial contrast maximum was defined as $\Delta\tau = 0.0\,\mathrm{fs}$. Figures adapted from [Rewitz14].

one after the other). For a pulse separation of $\Delta\tau = -107.8\,\mathrm{fs}$, an example experimental result of the configuration described here is shown in Fig. 5.7b. The time-integrated inten-

sity (recorded with the two-dimensional CCD, cf. Section 5.2) is approximately the same in both output ports. This is confirmed by the spatial contrast curve (Fig. 5.7e), which has a value close to zero [sc $= -0.06$, cf. Eq. (5.2)] at this separation of the pulses. Again, the energy E emitted at each output port was determined by the background corrected integral in $1 \times 1\,\mu\mathrm{m}^2$ regions as indicated with the yellow squares in Figs. 5.7b,c,d.

If, on the other hand, both pulses are superimposed in time, the instantaneous polarization of the excitation field varies as a function of the time delay $\Delta\tau$. Using such polarization-shaped laser pulses, it is possible to control and visualize a coherent process of alternating routing by scanning the temporal overlap stepwise and recording the spatial map of time-integrated sample emission for each step. As seen in Fig. 5.7e, the spatial contrast remains constant with decreasing temporal separation of the excitation pulses as long as both pulses are not superimposed in time. However, as soon as temporal overlap occurs, the light emission alternates between both output ports with increasing spatial contrast. Near the perfect temporal overlap (Fig. 5.7f) changing the time delay by $\Delta\tau = 1.3\,\mathrm{fs}$, corresponding to a half of the optical field oscillation cycle, is enough to invert the spatial contrast from sc $\approx +1$ to sc ≈ -1, i.e., to switch the routed signal between both output ports. This switching is illustrated in Figs. 5.7c (emission from A at $\Delta\tau = 0.0\,\mathrm{fs}$) and 5.7d (emission from B at $\Delta\tau = 1.3\,\mathrm{fs}$).

The optimal excitation position for the above described experiment was found by maximizing the emitted energy at both outputs for each polarization separately while maintaining a spatial contrast close to sc $= 0$. This means a trade-off between both polarizations, since each has a different optimal position as discussed before. It can be seen in the spatial contrast curve (Fig. 5.7e) that the chosen position was almost perfect at the beginning of the delay scan [sc$(\Delta\tau = -107.8\,\mathrm{fs}) = -0.06$] but changed slightly during the measurement due to stability issues [sc$(\Delta\tau = 108.2\,\mathrm{fs}) = -0.16$].

In order to understand the shape of the spatial contrast curve as a function of time delay between the two orthogonally polarized laser pulses (Fig. 5.7e) it is instructive to think about the principle of the directional coupler. The projection of the excitation polarization onto $+45^\circ$ and -45° (with respect to the symmetry axis of the nanostructure) is transmitted to output ports A and B, respectively. For the experimental setting used to demonstrate the alternating routing (Fig. 5.7) this means that the intensity measured in each output port during a delay scan basically reproduces a linear field cross correlation of the two excitation pulses. The shape of this cross correlation depends on the spectra and the spectral phase difference between the two plasmonic pulses at the branching of the directional coupler. The Fourier transform of such a field cross correlation gives access to this spectral phase difference. The amplitude of this Fourier transform is the product of both plasmonic pulses' spectral amplitudes. Even though both near-field pulses are excited by essentially the same far-field pulse (cf. Section 5.2), these spectral amplitudes might differ slightly since each eigenmode can have a different eigenspectrum.

In Figure 5.8 the phase difference obtained from the field cross correlation recorded at output port A (green solid) is shown together with the one obtained from simulated data (blue dashed). The simulation models a cross correlation with pulses obtained from a measured spectrum: One pulse was attributed a flat spectral phase, the other one was assigned the spectral phase originating from the dispersion of the half-wave plate and the polarizer in the Mach–Zehnder delay line (cf. Section 5.2). As expected, the main phase contribution

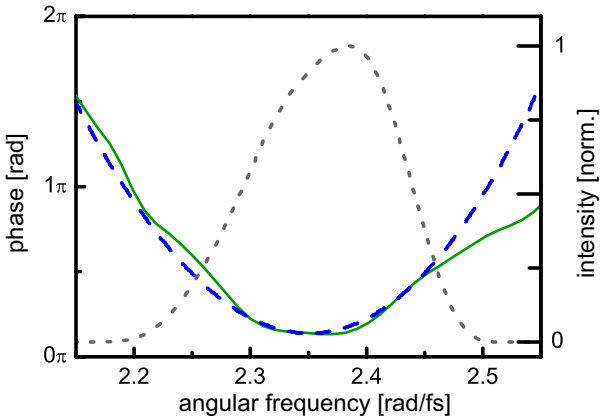

Figure 5.8: Spectral phase differences obtained from Fourier-transform evaluations. The blue-dashed curve was calculated by simulating a cross correlation of the two input pulses. The green solid curve was obtained by evaluating the measured cross correlation at output port A. Both curves show the same quadratic dependence in the relevant region indicated by the laser spectrum (gray dotted). Figure adapted from [Rewitz14].

is a quadratic term (corresponding to the so-called group-velocity dispersion). The fact that the phase from the field cross correlation (green solid) is consistent with the simulated one (blue dashed) confirms (within the measurement error) that no spectral phase difference between the two near-field eigenmodes is introduced by propagation in the directional coupler. Additionally, the overall shape of the spatial contrast curve (Fig. 5.7e) is explained by the evaluated phase difference and asymmetric spectral shapes of the excitation pulses (gray dotted line in Fig. 5.8).

5.6 Potential of Polarization-Shaped Laser Pulses

In the last section, concerning the alternating routing experiment (Fig. 5.7), mainly the extremes of the spatial contrast curve were discussed, i.e., time delays $\Delta\tau$ that correspond to $\pm 45^\circ$ polarized excitation pulses. Now, further potential of complex polarization-shaped pulses [Brixner01b] is illustrated by considering time delays comparable to the bandwidth-limited pulse length.

A quasi-3D representation of such an excitation pulse for the delay of $\Delta\tau = 22.7\,\mathrm{fs}$ (see black open circle in Fig. 5.7e) is shown in Fig. 5.9a. It was simulated using measured spectra and zero spectral phase for the x-polarized pulse as well as a linear spectral phase of $b_1 = 22.7\,\mathrm{fs/rad}$ [cf. Eq. (2.19)] for the y-polarized pulse. The pulse is approximately linearly polarized with orientation evolving from x to -45° and finally to y polarization. Feeding this pulse into the nanoscale directional coupler results in output pulses as shown in Fig. 5.9b: The temporal evolution of the emission in output port B (red dashed) follows the projection of the polarization onto the -45° axis, whereas in output port A (green solid) it follows the projection onto the $+45^\circ$ axis. Consequently, output port A emits a closely spaced double pulse in time. This example illustrates that polarization pulse shaping allows arbitrary output pulse patterns that are only limited by the excitation pulse bandwidth.

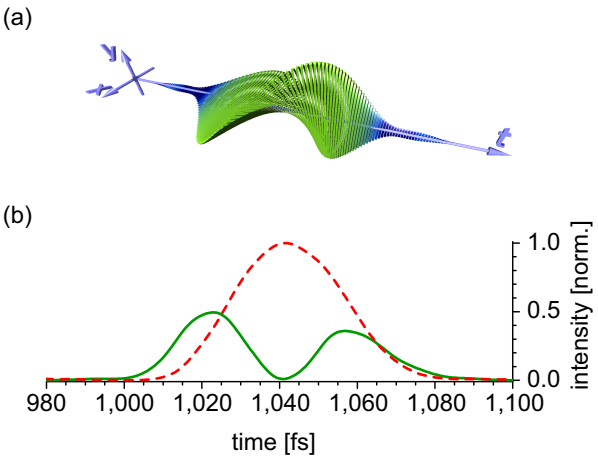

Figure 5.9: Potential of polarization-shaped laser pulses. (a) Depicts a quasi-3D representation of the input field for a pulse separation of $\Delta\tau = 22.7\,\mathrm{fs}$ (see black open circle in Fig. 5.7e). (b) Reconstructed temporal envelopes from measurements at output port A (green solid) and B (red dashed) are shown for the same pulse separation. Figures adapted from [Rewitz14].

5.7 Conclusion and Outlook

In conclusion, successful experimental ultrafast spatial and spatiotemporal control of plasmon propagation in a nanoscale directional coupler was demonstrated and the results show the potential and importance of optical control in the design and operation of plasmonic nanocircuitry. The interference of well-characterized multiple eigenmodes was exploited to deterministically route ultrashort plasmon pulses in a symmetric plasmonic device, thereby inducing a fundamentally different behavior not accessible in classical electronic devices. Due to the optimized design of the nanocircuit, which allows quantitative selective excitation of the eigenmodes, control was achieved using simple linearly polarized ultrashort laser pulses and pulse pairs, thus realizing light guidance [Sukharev06] and femtosecond energy localization at the nanoscale [Stockman02] without the use of learning algorithms. Importantly, switching of the emission between both output ports of the nanoscale directional coupler was achieved without changing the location of illumination, which is highly desirable in on-chip plasmonics. Finally, by characterizing the emitted light pulses it is shown that although the structure was optimized for a specific wavelength, it is sufficiently broadband to enable practically undistorted propagation of femtosecond pulses. This is important for potential applications in data processing.

The findings open an interesting route to femtosecond pump–probe experiments on the nanoscale [Brixner05]. The demonstrated control of spatial–temporal emission characteristics can be further improved using a polarization pulse shaper [Brixner01b] providing access to arbitrary output pulse patterns only limited by the excitation pulse bandwidth. By changing the branching position of the nanoscale directional coupler its function can be adapted, e.g., to achieve switching between both output ports using right and left circularly polarized excitation light. Reciprocity implies that a carefully selected superposition of near-field modes, excited at the two output ports, can drive the linear (input) antenna such that it radiates any far-field polarization state. Moreover, the nanoscale directional coupler can be extended to a nanointerferometer, which might enable probing, e.g., quantum optical properties of single plasmons [Kolesov09] or phase differences in plasmonic systems induced by optical nonlinearities [Davoyan10, Crutcher12].

6 Summary and Outlook

Plasmonics is an interdisciplinary research field that explores the unique properties of surface plasmon polaritons at nanostructured metallic surfaces. These plasmons are electromagnetic modes coupled to the oscillating surface electron density of conductors. They encompass propagating optical near fields concentrated below the diffraction limit. By integrating plasmonic and photonic elements, high bandwidth optical data processing at the footprint size of nowadays nanoscale electronic circuits might be possible in the future. To characterize the performance of integrated plasmonic functional elements, such as splitters, multiplexers, switches, or logic gates, an optical technique with high spatial and ultrafast temporal resolution is required.

In this work, modified confocal microscopy with heterodyne detection was employed to meet these demands. The developed technique combines confocal microscopy with spectral interferometry and employs broadband femtosecond pulses for ultrafast temporal resolution [Rewitz12a]. The excitation and detection positions can be chosen independently, thereby enabling optical excitation of a certain (nano)structure at one spot while monitoring its emission at another spot. Additionally to the characterization of emission pulses, the experimental procedure includes the measurement of a reference reflection in order to extract spatial-spectral response functions that provide the full amplitude and phase information of propagated near-field signals in plasmonic elements.

Experimental knowledge of the structure- and environment-dependent group velocity and dispersion of propagating optical near fields is important for the design of nanooptical circuits, in which signal delays play a major role. By using spectrally broad laser pulses in combination with Fourier-transform evaluation, these characteristics were determined with the developed technique of spectral-interference microscopy. For this purpose, careful analysis of geometrical path differences within the experimental setup is crucial to reveal time delays of signals that are on the order of femtoseconds and would hinder the correct characterization of group velocities. Such time delays—termed position-dependent pulse arrival time (PD-PAT)—were analyzed and quantified using a ray-tracing model together with the experimental calibration of free parameters in a derived formula. Furthermore, the model was verified in a demonstration experiment.

Subsequently, the group velocity and dispersion of propagating optical near fields was characterized for different nanostructures that vary in complexity. In the case of chemically synthesized silver nanowires, i.e., the least complex structures, a pronounced dependence of the group velocity on the nanowire diameter was observed and confirmed with simulations [Rewitz12b]. In the presented data set, the group velocity varies from 22 % to 44 % of the speed of light in vacuum. In particular, a drastic decrease for nanowire diameters below 100 nm was determined, while the group velocity saturates for larger diameters. This dependence is expected from theory but has not been determined experimentally before. Concerning the dependence on the local environment, it was shown that the propagating

optical near field is approximately 25 % slower if the nanowire, which is situated on a glass substrate, is embedded in index-matched oil. Furthermore, the dispersion upon propagation was characterized to be very low. Therefore, the duration of the near-field pulses is not significantly elongated as they propagate along the nanowire. This result is especially relevant for non-linear nanoscale experiments.

Next, top-down fabricated single-crystalline gold nanostructures were investigated. Compared to bottom-up chemical synthesis, the more costly top-down technique allows fabrication of complex nanostructures. To verify the usability of the structures for near-field propagation experiments, gold nanowires were tested and a geometry dependence of the group velocity similar to the silver nanowires was observed. The successful characterization with the spectral-interference microscope confirms the versatility of gold nanostructures. Hence, more complex structures that support multiple well-known modes, a necessity for the coherent control of near-fields [Rewitz09], can be simulated, designed and fabricated.

In this context, so-called two-wire transmission lines with mode detectors were investigated. Simulations indicated that the structures support two propagating modes with different near-field intensity profiles, effective wavelengths and group velocities. In experiments, quantitative selective excitation of the modes was facilitated by positioning a linearly polarized laser focus on appropriate input antennas. Due to the mode detector at the output end, the two modes have spatially separated emission spots. Thus, characterization of multimode contributions with the spectral-interference microscope is possible. For the two-wire transmission lines, experimental determination of mode sensitive group velocities was accomplished [Geisler13]. A difference of 8 % in group velocity was quantified for the two fundamental modes and agreed with simulations.

In the last part of this work, the accumulated knowledge was used to develop a nanoscale directional coupler with one input and two output ports. In this nanooptical circuit, the spatial and temporal evolution of propagating optical near fields was controlled by far-field laser pulses [Rewitz14]. This is a key requirement to expand the functionality of integrated nanooptical circuits and take full advantage of them. Due to the intuitive and optimized design of the coupler, varying the linear polarization of an excitation pulse sufficed to route the optical energy between both output ports. A similar kind of open-loop control has not been presented in the literature so far. For the experimental characterization of the nanoscale directional coupler, the spectral-interference microscope was enhanced so that two orthogonally polarized excitation pulses with an arbitrary temporal separation could be produced. Hence, single-pulse routing and ultrafast spatiotemporal control was demonstrated. The system was stable enough to alternate the routing between both output ports by changing the exact excitation polarization via the delay of the two superimposed ultrashort pulses.

In this dissertation, linear properties of propagating ultrashort near fields were investigated by fully characterizing emitted pulses. Inherent to these nanooptical excitations is a strong field localization, e.g., in the substrate, and a field enhancement. This significantly increases non-linear optical effects, which modify the amplitude and phase of emitted pulses. Therefore, the setup presented in this work also provides a unique opportunity to investigate the influence of non-linear effects on plasmon propagation [Davoyan10, Crutcher12]. In fact, such investigations are currently prepared as part of the continued project.

Moreover, based on the near-field mode properties that were characterized in this work, more complex nanocircuits can be designed to further enhance the light–matter interaction,

e.g., at specific locations within the nanostructures. Quantum optical properties of single surface plasmon polaritons [Kolesov09] might be probed with nanointerferometers that are based on the nanoscale directional coupler presented in this work.

The demonstrated far-field control of propagating optical near fields is a requirement to take full advantage of future integrated plasmonic circuits. Furthermore, it opens an interesting route to ultrafast pump–probe spectroscopy on the nanoscale [Brixner05]. In such experiments, nanoscale energy or charge transfer processes would be investigated by controlling the localization and timing of a pump and a probe pulse with sub-diffraction spatial and femtosecond temporal resolution. In this context, it is interesting to note that the control of spatiotemporal near-field localization in the nanoscale directional coupler, which was detected by characterizing the emission, could be improved with a polarization pulse shaper [Brixner01b]. Polarization-shaped input pulses would provide access to arbitrary output pulses, i.e., spatiotemporal near field patterns that are limited by the excitation pulse bandwidth only.

Zusammenfassung und Ausblick

In dem interdisziplinären Forschungsfeld der Plasmonik werden die einzigartigen Eigenschaften von Oberflächenplasmonen auf nanostrukturierten metallischen Oberflächen untersucht. Diese Plasmonen sind elektromagnetische Moden, die mit der oszillierenden Oberflächenelektronendichte der Leiter gekoppelt sind. Mit ihnen einher gehen propagierende optische Nahfelder, die unterhalb des Beugungslimits konzentriert sind. Durch die Integration von plasmonischen und photonischen Elementen könnte es in Zukunft möglich werden, die hohe Bandbreite der optischen Datenverarbeitung auf den nanometergroßen Abmessungen von heutigen elektronischen Schaltkreisen zu nutzen. Um die Leistung von integrierten plasmonischen funktionalen Elementen wie zum Beispiel Multiplexern, Demultiplexern, Schaltern oder Logikgattern zu charakterisieren, wird eine optische Technik mit hoher räumlicher und ultraschneller zeitlicher Auflösung benötigt.

In der vorliegenden Arbeit wurde eine modifizierte Version von konfokaler Mikroskopie zusammen mit überlagernder Detektion benutzt, um diesen Anforderungen gerecht zu werden. Die entwickelte Technik kombiniert konfokale Mikroskopie mit spektraler Interferometrie und benutzt spektral breitbandige Femtosekunden-Laserpulse, um eine ultraschnelle zeitliche Auflösung zu erreichen [Rewitz12a]. Anrege- und Abfragepositionen können unabhängig voneinander gewählt werden, so dass eine (Nano-)Struktur an einer Stelle optisch angeregt und währenddessen die Emission der Struktur an einer anderen Stelle beobachtet werden kann. Zusätzlich zur Charakterisierung von Emissions-Laserpulsen wurde in jedem Experiment eine referenzierende Reflektion vermessen, um örtlich-spektrale Antwortfunktionen zu extrahieren, welche die vollen Amplituden- und Phaseninformationen der propagierten Nahfeldsignale von plasmonischen Elementen enthalten.

Die experimentelle Charakterisierung der struktur- und umgebungsabhängigen Gruppengeschwindigkeit und der Dispersion von propagierenden optischen Nahfeldern ist für die Entwicklung von nanooptischen Schaltkreisen relevant, in denen Signalverzögerungen eine wichtige Rolle spielen. Durch die Kombination von spektral breiten Laserpulsen mit Fouriertransformationsauswertung wurden diese Eigenschaften mithilfe der entwickelten Spektral-Interferenz-Mikroskopie bestimmt. Dafür ist eine sorgfältige Analyse von geometrischen Weglängenunterschieden innerhalb des experimentellen Aufbaus unerlässlich. Diese Unterschiede führen zu Signalverzögerungen in der Größenordnung von Femtosekunden und würden bei Nichtbeachtung eine korrekte Charakterisierung der Gruppengeschwindigkeiten unmöglich machen. Die Signalverzögerungen, welche "positionsabhängige Pulsankunftszeit" getauft wurden (engl.: position-dependent pulse arrival time, PD-PAT), wurden in der vorliegenden Arbeit analysiert und quantifiziert. Dafür wurde ein auf der geometrischen Optik basierendes Modell benutzt und die freien Parameter einer hergeleiteten Formel experimentell kalibriert. Des Weiteren wurde das Modell in einem Demonstrationsexperiment verifiziert.

Im Anschluss wurde die Gruppengeschwindigkeit und Dispersion von propagierenden optischen Nahfeldern für verschiedene Nanostrukturen, die in ihrer Komplexität variieren, charak-

terisiert. Für chemisch synthetisierte Silber-Nanodrähte, also die einfachste Struktur, wurde eine ausgeprägte Abhängigkeit der Gruppengeschwindigkeit von dem Durchmesser des Nanodrahtes beobachtet und mit Simulationen bestätigt [Rewitz12b]. In dem präsentierten Datensatz variiert die Gruppengeschwindigkeit zwischen 22 % und 44 % der Geschwindigkeit von Licht in Vakuum. Insbesondere wurde ein drastischer Abfall für Nanodraht-Durchmesser unter 100 nm ermittelt während die Geschwindigkeit für größere Durchmesser sättigt. Dieser Zusammenhang wird von der Theorie vorhergesagt aber er wurde vorher noch nie experimentell bestätigt. Für die Abhängigkeit von der lokalen Umgebung wurde gezeigt, dass das propagierende optische Nahfeld circa 25 % langsamer ist, wenn der auf einem Glassubstrat aufliegende Nanodraht in einem Immersionsöl mit dem Brechungsindex von Glas eingebettet ist. Des Weiteren wurde die Dispersion bei der Propagation als sehr gering charakterisiert. Daher verlängern sich Plasmonen-Pulse nicht signifikant während sie entlang des Nanodrahtes propagieren. Dieses Ergebnis ist für nichtlineare Experimente von besonderer Bedeutung.

Im nächsten Schritt wurden Gold-Nanostrukturen untersucht, die durch eine Abwärtsstrukturierung von einkristallinem Gold hergestellt sind. Verglichen mit der chemischen Synthese erlaubt die Abwärtsstrukturierung die Herstellung von komplexen Nanostrukturen. Um die Tauglichkeit der Strukturen für Nahfeld-Propagationsexperimente zu testen, wurden Gold-Nanodrähte untersucht und dabei eine ähnliche Abhängigkeit der Gruppengeschwindigkeit von der Geometrie wie bei Silber-Nanodrähten festgestellt. Diese erfolgreiche Charakterisierung mit dem Spektral-Interferenz-Mikroskop bestätigt die Vielseitigkeit von Gold-Nanostrukturen. Daher können komplexere Strukturen, die mehrere Moden aufweisen, simuliert, entworfen und hergestellt werden. Die Existenz von verschiedenen, klar definierten Moden ist eine Notwendigkeit für die kohärente Kontrolle von Nahfeldern [Rewitz09].

In diesem Zusammenhang wurden so genannte Zweidraht-Wellenleiter mit Modendetektoren untersucht. Simulationen zeigten, dass diese Strukturen zwei propagierende Moden mit unterschiedlichen Nahfeld-Intensitätsprofilen, effektiven Wellenlängen und Gruppengeschwindigkeiten aufweisen. Im Experiment konnte eine quantitativ selektive Anregung dieser Moden durch die Positionierung eines linearpolarisierten Laserfokus auf geeigneten Einkoppelantennen gewährleistet werden. Aufgrund des Modendetektors am anderen Ende der Struktur haben die beiden Moden örtlich separierte Emissionspositionen. Daher ist die Charakterisierung der Beiträge einer Multimoden-Anregung mit dem Spektral-Interferenz-Mikroskop möglich. Bei den Zweidraht-Wellenleitern konnte die Gruppengeschwindigkeit modenaufgelöst experimentell bestimmt werden [Geisler13]. Ein Gruppengeschwindigkeitsunterschied von 8 % zwischen den beiden fundamentalen Moden wurde quantifiziert. Dieser Wert stimmte mit Simulationen überein.

Im letzten Teil dieser Arbeit wurde das vorher angehäufte Wissen genutzt um einen nanoskaligen Richtungskoppler mit einem Eingang und zwei Ausgängen zu entwerfen. In diesem Richtungskoppler wurde die örtliche und zeitliche Entwicklung von propagierenden optischen Nahfeldern durch Fernfeld-Laserpulse kontrolliert [Rewitz14]. Dies ist eine Schlüsselbedingung, um die Funktionalität von integrierten nanooptischen Schaltkreisen auszuweiten und alle ihre Vorteile voll auszunutzen. Wegen des intuitiven und optimierten Aufbaus des Kopplers, genügte es die lineare Polarisation eines Anrege-Laserpulses zu variieren, um zu steuern zu welchem Ausgang die optische Energie geleitet wird. Eine ähnliche Art von Steuerung findet sich nicht in der Literatur. Für die experimentelle Charakterisierung des nanoskaligen Richtungskopplers wurde das Spektral-Interferenz-Mikroskop erweitert, so dass zwei senk-

recht zueinander polarisierte Anrege-Laserpulse mit einer beliebigen zeitlichen Separation produziert werden konnten. Damit wurde dann Einzelpuls-Steuerung und ultraschnelle Ort-Zeit-Kontrolle gezeigt. Des Weiteren war das System stabil genug, um die Emission zwischen beiden Ausgängen zu alternieren, indem die exakte Anregepolarisation über die zeitliche Separation der beiden überlagerten ultrakurzen Laserpulse geändert wurde.

In dieser Dissertation wurden lineare Eigenschaften von propagierenden ultrakurzen Nahfeldern untersucht, indem emittierte Laserpulse vollständig charakterisiert wurden. Mit den nanooptischen Anregungen ist eine starke Feldlokalisierung, zum Beispiel in dem Substrat, und eine Feldüberhöhung verknüpft. Beides verstärkt nichtlineare optische Effekte, welche die Amplitude und Phase von emittierten Laserpulsen verändern. Daher eröffnet die in dieser Arbeit vorgestellte Technik der Spektral-Interferenz-Mikroskopie auch eine einzigartige Möglichkeit den Einfluss von nichtlinearen Effekten auf Plasmonenpropagation zu untersuchen [Davoyan10, Crutcher12]. Tatsächlich werden solche Untersuchungen zurzeit als Fortsetzung des Projekts vorbereitet.

Darüber hinaus können, basierend auf den Eigenschaften der in dieser Arbeit charakterisierten Nahfeldmoden, komplexere Nano-Schaltkreise entworfen werden, welche die Wechselwirkung von Licht und Materie, zum Beispiel an bestimmten Positionen innerhalb der Nanostrukturen, noch mehr verstärken. Quantenoptische Eigenschaften von einzelnen Oberflächenplasmonen [Kolesov09] könnten mit Nano-Interferometern untersucht werden, welche auf dem nanoskaligen Richtungskoppler aufbauen, der in dieser Arbeit präsentiert wurde.

Die veranschaulichte Fernfeld-Kontrolle von propagierenden optischen Nahfeldern ist eine Voraussetzung, um alle Vorteile von zukünftigen integrierten plasmonischen Schaltkreisen voll ausschöpfen zu können. Außerdem eröffnet sie eine interessante Möglichkeit für ultraschnelle Anrege-Abfrage-Spektroskopie auf der Nanoskala [Brixner05]. In solchen Experimenten könnten Energie- oder Ladungstransporte auf der Nanoskala untersucht werden, indem die Lokalisierung und zeitliche Abstimmung von Anrege- und Abfrage-Laserpulsen mit einer beugungsunbegrenzten örtlichen und einer zeitlichen Auflösung auf der Femtosekundenskala kontrolliert werden. In diesem Zusammenhang sollte auch erwähnt werden, dass die Ort-Zeit-Kontrolle von Nahfeldlokalisierung in dem nanoskaligen Richtungskoppler, welche über die Charakterisierung der Emission detektiert wurde, durch die Verwendung eines Polarisationspulsformers [Brixner01b] verbessert werden könnte. Die Verwendung von polarisationsgeformten Laserpulsen als Anregung würde beliebige Emissionspulse ermöglichen. Das heißt, Ort-Zeit-Profile im Nahfeld, die nur von der Anregelaserpuls-Bandbreite limitiert sind, wären möglich.

A Appendices

A.1 Details on Near-Field Simulations

Parts of this Appendix have been published in [Rewitz12b].

All near-field simulations presented in this work were performed by Gary Razinzkas and Peter Geisler within the collaboration described at the beginning of Chapter 4. Dispersion relations, from which the group velocities were derived, as well as mode profiles (Sections 2.4.3, 4.2, and 4.3) were simulated using the full-vectorial finite-difference frequency-domain (FDFD) method (MODE Solutions, Lumerical Solutions Inc., Vancouver, Canada). Near-field intensity maps with corresponding far-field projections [Lumerical12] (Section 5.3) and full three-dimensional simulations (Section 4.2) were obtained with the finite-difference time-domain method (FDTD Solutions, Lumerical Solutions Inc., Vancouver, Canada).

In each simulation, a uniform mesh with discretization of 0.5 nm in each direction usually covered the complete structure and its close surrounding. To avoid spurious absorption of the near fields all boundaries of a simulation box were set to be at least 800 nm away from the structure.

Following refractive indices were used for various dielectrics:
$n_{\mathrm{air}} = 1.0000$, $n_{\mathrm{oil}} = 1.5071$, $n_{\mathrm{glass}} = n_{\mathrm{SiO_2}} = 1.5100$, $n_{\mathrm{ITO}} = 1.8000$ [Laux98], $n_{\mathrm{Ag_2S}} = 2.9$ [Bennett70], $n_{\mathrm{Ag_2O}} = 2.25$ [Pettersson95].

The permittivities of silver and gold were taken from experimental data ([Palik97] and [Johnson72], respectively). In the case of silver the software performs a polynomial fit to yield data points for every wavelength, whereas a fit to an analytic model [Etchegoin06] is used in the case of gold. Figure A.1 visualizes the used data.

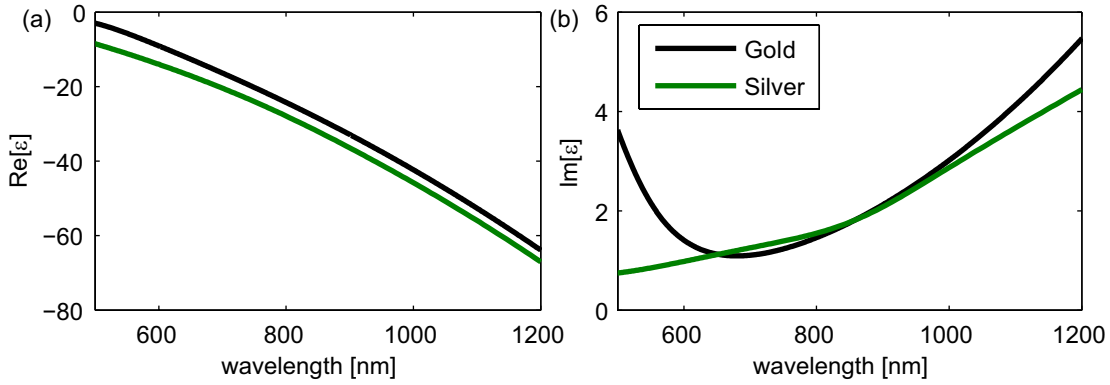

Figure A.1: Permittivity data of silver and gold as used in the simulations. (a) Real part of ε. (b) Imaginary part of ε. Thanks to Gary Razinskas for providing the data.

A.2 Derivation of Optical Path-Length Difference for PD-PAT

This Appendix has been published in [Rewitz12a].

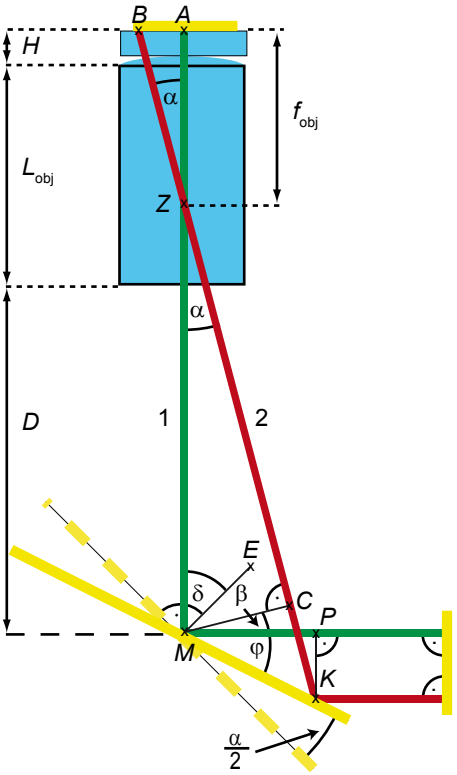

Figure A.2: Detailed schematic of Fig. 3.6 for trigonometric derivation of Eq. (3.3). $\overline{ME}$ is the normal to the untilted mirror surface (dashed yellow line). Figure adapted from [Rewitz12a]. © (2012) Optical Society of America.

Here, a way of deriving the optical path differences that lead to the position-dependent pulse arrival time (PD-PAT) as defined in Eq. (3.3) is described. The angles in Fig. A.2 are defined as follows: $\delta = \angle(\overline{AM};\overline{ME}) = \angle(\overline{EM};\overline{MP})$, $\alpha = \angle(\overline{BZ};\overline{ZA})$, $\varphi = \angle(\overline{PM};\overline{MK})$, $\beta = \angle(\overline{CM};\overline{MP})$.
From Fig. A.2 the lengths of the optical paths 1 (green) and 2 (red) from the sample plane (AB) to the reference plane (PK) can be decomposed as:

- $\overline{1} = (H + L_{obj})n_{obj} + D + \overline{MP}$,
- $\overline{2} = \overline{BZ} + \overline{ZC} + \overline{CK}$.

The unknown length $\overline{MP}$ in path 1 can be found as follows:

- $\overline{MP} = \overline{MK}\cos\varphi$,
- $\overline{MK} = \overline{MC}/\cos(\varphi + \beta)$,

- $\overline{MC} = \{[L_{\text{obj}} - (f_{\text{obj}} - H)]n_{\text{obj}} + D\} \sin\alpha$.

Thus, $\overline{MP} = \{[L_{\text{obj}} - (f_{\text{obj}} - H)]n_{\text{obj}} + D\} \sin\alpha \cos\varphi / \cos(\varphi + \beta)$.

For the angles, following relations hold:

- $\varphi = \frac{\pi}{2} - \frac{\alpha}{2} - \delta$,
- $(\delta + \delta - \beta) + \frac{\pi}{2} + \alpha = \pi \Leftrightarrow \beta = 2\delta - \frac{\pi}{2} + \alpha$.

Therefore, $\varphi + \beta = \frac{\alpha}{2} + \delta$, and

$$\overline{MP} = \{[L_{\text{obj}} - (f_{\text{obj}} - H)]n_{\text{obj}} + D\} \sin\alpha \cos(\tfrac{\pi}{2} - \tfrac{\alpha}{2} - \delta) / \cos(\tfrac{\alpha}{2} + \delta).$$

For the unknown lengths in path 2, following relations hold:

- $\overline{BZ} = (f_{\text{obj}} n_{\text{obj}}) / \cos\alpha$,
- $\overline{ZC} = \{[L_{\text{obj}} - (f_{\text{obj}} - H)]n_{\text{obj}} + D\} \cos\alpha$,
- $\overline{CK} = \overline{MC} \tan(\varphi + \beta)$.

If all the information is combined and the optical path difference is mathematically simplified, one gets

$$\overline{2} - \overline{1} = -D - (H + L_{\text{obj}})n_{\text{obj}} + [D + (-f_{\text{obj}} + H + L_{\text{obj}})n_{\text{obj}}] \cos\alpha + f n_{\text{obj}} / \cos\alpha. \quad \text{(A.1)}$$

Note that this difference is independent of the angle δ, implying that this angle does not have to be 45°, which allows for a slight misalignment. In contrast, a parallel shift of the line AM, i.e., a displacement of the center of rotation of the piezo tip-tilt mirror with respect to the optical axis of the objective, shifts the PD-PAT center as discussed in Section 3.4 and measured in Appendix A.3.

By taking into account that $D > L_{\text{obj}} \gg f_{\text{obj}} > H$ [because $D = (39.7 \pm 0.5)\,\text{cm}$, $L_{\text{obj}} = 5.5\,\text{cm}$, $f_{\text{obj}} = 2\,\text{mm}$ and $H = 0.17\,\text{mm}$], $f_{\text{obj}} = H = 0$ can be assumed. This reduces the optical path difference to

$$\overline{2} - \overline{1} = (L_{\text{obj}} n_{\text{obj}} + D)(\cos\alpha - 1). \quad \text{(A.2)}$$

With the assumption that only very small angles are considered ($\pm 10\,\mu\text{m} \mathrel{\widehat{=}} \pm 0.005\,\text{rad}$) and by defining $A = L_{\text{obj}} n_{\text{obj}} + D$, this formula further simplifies to

$$\overline{2} - \overline{1} = -\frac{A}{2} \left(\frac{r}{f_{\text{obj}}} \right)^2, \quad \text{(A.3)}$$

which is Eq. (3.3).

All assumptions that are made, i.e., $f_{\text{obj}} = H = 0$, $\cos\alpha = 1 - \frac{\alpha^2}{2}$, and $\alpha = r/f_{\text{obj}}$, create a systematic deviation of the approximation [Eq. (A.3)] with respect to the exact formula [Eq. (A.1)] that is equal to $-0.1\,\text{fs}$ at a distance of $5\,\mu\text{m}$ to the PD-PAT center and, hence, is an order of magnitude below the estimated PD-PAT error of $\Delta t_{\text{corr}} \approx 1\,\text{fs}$ (cf. Section 3.5).

A.3 Determination of PD-PAT Center Position

Parts of this Appendix have been published in [Rewitz12a].

As explained in Section 3.3, the plasmon propagation on nanowires can be measured in two different directions (cf. Fig. 3.4b: "LL2UR-propagation" and Fig. 3.4c: "UR2LL-propagation" for the case of silver nanowires). Since the coupling to the nanowire does not influence the propagation velocity, both measurement directions should yield the same result. This statement was checked by measuring, e.g., a "LL2UR-propagation", turning the sample around 180°, and performing the same experiment again. In the case of silver nanowires, the relative difference of the calculated velocities for both experiments, which is independent of the PD-PAT correction, was on the order of $(v_{\mathrm{LL2UR},0^\circ} - v_{\mathrm{LL2UR},180^\circ})/(v_{\mathrm{LL2UR},0^\circ}) = 2\,\%$, i.e., within the measurement error. For comparison, the relative difference of the velocities, calculated without applying the PD-PAT correction, for different measurement directions was mostly $(v_{\mathrm{LL2UR}} - v_{\mathrm{UR2LL}})/(v_{\mathrm{LL2UR}}) \geq 10\,\%$.

This consideration yields a handle for determination of the unknown parameters Δx and Δy of Eq. (3.4). By applying the PD-PAT correction to the determined separation times Δt_j [cf. Eq. (3.5)] of both measurement directions (j = UR2LL and j = LL2UR) for various parameter pairs Δx and Δy, these two parameters can be found under the constraint that the corrected propagation velocities for both measurement directions have to be the same. Since in fact only the PD-PAT value at the excitation and emission position is fixed by this procedure, one nanowire measurement is not enough. However, by fitting the data of multiple nanowires (with preferably different lengths and—more importantly—different orientations) the parameters Δx and Δy can be found with sufficient accuracy. Note that no *a priori* knowledge of the absolute value of the plasmon group velocity is needed for this procedure.

For the results presented in Sections 3.4 and 4.2, a set of 13 silver nanowires was measured in both directions. Subsequently, an unconstrained nonlinear optimization procedure was used to minimize the total squared corrected velocity differences $[\Sigma_{k=1}^{13} (v_{\mathrm{UR2LL},k} - v_{\mathrm{LL2UR},k})^2]$ of both directions under variation of the parameters Δx and Δy. This resulted in $\Delta x = (0.68 \pm 0.3)\,\mu$m and $\Delta y = (1.13 \pm 0.3)\,\mu$m. In all "emission" figures of Chapter 3 (Figs. 3.4b, 3.4c, and 3.7) the axes are labeled with respect to the PD-PAT center, i.e., the position (0,0) is the PD-PAT center and the excitation/reflection position is at $(\Delta x, \Delta y)$. By applying the PD-PAT correction the relative difference of both measurement directions was decreased to about 2 %.

The described experimental procedure was later improved and accelerated by using a "PD-PAT calibration sample" that was fabricated by Peter Geisler. This sample consists of 16 focused-ion-beam (FIB) structured gold single nanowires oriented like sun rays around a center position, with orientation varying in steps of 22.5°. This sample facilitates fast measurements of multiple nanowires in both directions and helps to re-calibrate the PD-PAT, which was done before new group velocities measurements were made.

It should be noted that in the case that the PD-PAT center and the excitation/reflection position do coincide (i.e., $\Delta x = \Delta y = 0$), both measurement directions will always yield the same separation time ($\Delta t_{\mathrm{UR2LL}} = \Delta t_{\mathrm{LL2UR}}$) since the PD-PAT is rotational symmetric. By the same argument this is also true if the shift vector $\left(\begin{smallmatrix}\Delta x \\ \Delta y\end{smallmatrix}\right)$ is normal to the characterized nanowires. This might erroneously lead to the conclusion that no correction has to be applied for a perfectly aligned system. However, it should be clear that the determined

propagation velocity will always be systematically wrong if no PD-PAT correction is applied [e.g., $T_{\mathrm{PD-PAT}}(5\,\mu\mathrm{m}, 0) = -5\,\mathrm{fs}$; for $\Delta x = \Delta y = 0$, cf. Eq. (3.4)].

A.4 Annotations to Demonstration of PD-PAT

As discussed in Section 3.4, a convex lens was inserted in front of the polarizer (cf. Fig. 3.2) in order to focus the excitation beam in the back focal plane of the objective and, hence, obtain a large illuminated sample area.[1] Using this method to get the waist of a "collimated" beam in the sample plane is experimentally a very challenging task, i.e., a pulse-front curvature at the reflection plane is inevitable [Klein86]. However, theoretical calculations showed that residual curvatures contribute negligibly to the fitted amplitude A of Eq. (3.4).

Other effects, such as the radial group delay dependence in chromatic lenses [Bor88, Radzewicz96], could slightly increase the amplitude A of the model that has to be used for the correction: In Fig. 3.6 signals on the red path (2) encounter the lens L_3 a distance p parallel shifted with respect to signals on the green path (1). However, the measurements (yielding slightly lower fitted amplitudes) indicate that the used achromatic lenses do not show a significant radial group delay at distances that are of importance ($r = 10\,\mu\mathrm{m} \mathrel{\widehat{=}} p = 2\,\mathrm{mm}$).

Since an inaccuracy of the amplitude is taken into account for the error calculation (cf. Section 3.5), neither of these two aspects plays a role.

As a last annotation, it is interesting to note that the recorded time-integrated intensity pattern in an "emission scan" with this configuration (additional lens) differs strongly from the reconstructed pattern of spectral-interference measurements at the dedicated temporal separation (τ ca. 600 fs, both patterns not shown). From this it can be concluded that, additionally to the sample-plane reflection (substrate-glass–air interface), another interface must also reflect some intensity that arrives at a different time at the detector and is added to the pattern of the sample-plane reflection to yield the time-integrated pattern.

A.5 Nanoscale Directional Coupler Optimization

This Appendix has been published in [Rewitz14].

The nanoscale directional coupler has been designed and optimized by the Hecht group using simulations (cf. Appendix A.1). The nanostructure, situated on a glass–air interface, consists of gold. To mimic the experimental conditions, the nanostructure illumination was modeled from the substrate side using a tightly focused Gaussian beam ($\lambda_0 = 800\,\mathrm{nm}$ in vacuum, NA = 1.4) centered on the incoupling antenna gap. The far-field projections consider the properties of the imaging system including the analyzer oriented perpendicularly to the nanostructure's symmetry axis and the intensity is normalized to an unstructured gold surface reflection. Only the dominating antisymmetric mode emission from the output ports is recorded (cf. Fig. 4.3e). Therefore, the far-field projections in Chapter 5 provide a quantitative comparison with the experimental time-integrated sample emission maps and the recorded spatial contrast values [cf. Eq. (5.2)] in the same chapter.

[1] Other methods to visualize the PD-PAT that did not work out are documented in the appendix of [Keitzl11].

To optimize the coupler for a specific function, i.e., output port switching between $+45^\circ$ and -45° linear excitation polarization and high throughput, several parameters were tuned: cross-sectional geometry of the two-wire transmission line, four-wire transmission line starting position, branching position and bending angle. Furthermore, the antenna geometry (overall length 400 nm, width 100 nm) was chosen so that it provides similar excitation efficiencies for both eigenmodes, which is important for maximal near-field interference. The dimensions of the two-wire transmission line were chosen so that only two well-defined modes with considerable propagation length ($> 2\,\mu$m) exist and the four-wire starting position was optimized to minimize reflections due to impedance mismatch [Huang09]. The distance between the start of the four-wire transmission line and the branching position has to be sufficiently large to allow most of the fields to locate at an outermost wire of the nanostructure, while the branching position was optimized such that the spatial contrast (sc) is maximal for $\pm 45^\circ$ linear excitation. Furthermore, a high signal throughput was achieved by keeping the radii of curvature in the bending region as large as possible (thus reducing propagation losses) while still being able to clearly spatially separate the two output ports by far-field optical microscopy.

A.6 Spectral Behavior of the Nanoscale Directional Coupler

The optimization of the nanocircuit has been performed by the Hecht group for the design wavelength of $\lambda_0 = 800$ nm and, therefore, the spatial contrast [cf. Eq. (5.2)] for x- or y-polarized excitation at this wavelength is high ($\mathrm{sc_{sim}} = \pm 0.90$). Further simulations show that the nanoscale directional coupler performs well in a sufficiently broad wavelength region around this design wavelength. The spatial contrast is $\mathrm{sc_{sim}} = \pm 0.63$ for $\lambda_0 = 750$ nm and $\mathrm{sc_{sim}} = \pm 0.89$ for $\lambda_0 = 850$ nm, even though the beating wavelength λ_{beat} and, thus, the beating pattern (cf. Fig. 5.2b) is a function of the vacuum wavelength.

The beating wavelength, i.e., the distance between two intensity minima on one wire of a two-wire transmission line (cf. Fig. 5.2b), is defined as [Hecht02]

$$\lambda_{\mathrm{beat}} = \frac{\lambda_{\mathrm{eff}}^{\mathrm{sym}}\,\lambda_{\mathrm{eff}}^{\mathrm{antisym}}}{\lambda_{\mathrm{eff}}^{\mathrm{sym}} - \lambda_{\mathrm{eff}}^{\mathrm{antisym}}}, \tag{A.4}$$

where $\lambda_{\mathrm{eff}}^{\mathrm{sym}}$ and $\lambda_{\mathrm{eff}}^{\mathrm{antisym}}$ are the effective wavelengths of the symmetric and antisymmetric eigenmode of a two-wire transmission line. In Figure A.3 this beating wavelength is plotted versus the excitation wavelength. Since both eigenmodes on a two-wire transmission line have similar dispersion relations, the beating wavelength shows a mostly linear dependence on the excitation wavelength. In an interval of 50 nm around the design wavelength of 800 nm λ_{beat} changes only by about 10 %. This explains the good performance of the nanocircuit in a broad spectral region, as described above.

However, the input antenna determines the excitation efficiency of each eigenmode and similar amplitudes of both eigenmodes are crucial for a perfectly modulated beating pattern (maximal near-field interference). Furthermore, the impedance of the transition from two to four wires might differ for each mode and wavelengths other than the design wavelength.

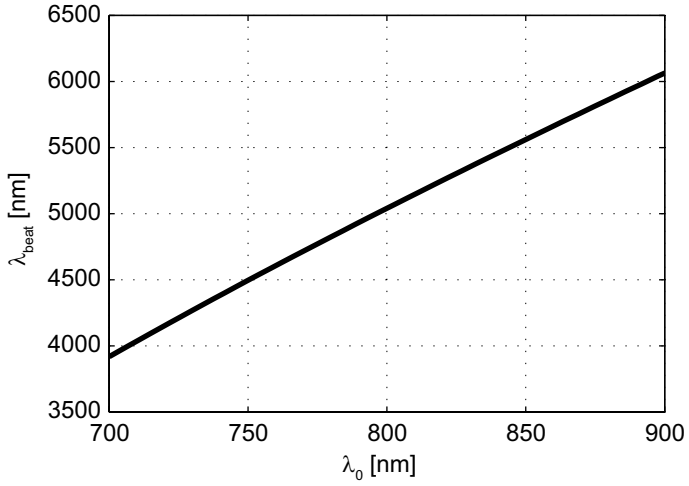

Figure A.3: Beating wavelength of a two-wire transmission line, cf. Fig. 5.2b and Eq. (A.4), as a function of excitation wavelength in vacuum. The beating wavelength changes basically linearly with excitation wavelength. Thanks to Gary Razinskas for providing the data.

Thus, the spectral dependence of the antenna incoupling efficiency and the impedance of the transition region might explain the asymmetric dependence of the spatial contrast on the excitation wavelength ($sc_{sim} = \pm 0.63$ for $\lambda_0 = 750\,nm$ and $sc_{sim} = \pm 0.89$ for $\lambda_0 = 850\,nm$). In any case, the experimentally determined spatial contrasts for spectrally broad laser pulses indicate a very good ultrafast performance of the nanocircuit (cf. Section 5.4).

As a last aspect related to the broadband, or better ultrafast, operation of the device, it is interesting to note that the difference in group velocity between both pulsed eigenmodes (cf. Section 4.3.2) becomes relevant only for very long propagation distances. For instance, a propagation length of about $40\,\mu m$ is required to separate the two pulsed propagating plasmon eigenmodes of a two-wire transmission line by a distance that is equivalent to a pulse duration of 40 fs.

Bibliography

[Aeschlimann07] Aeschlimann, M.; Bauer, M.; Bayer, D.; Brixner, T.; García de Abajo, F. J.; Pfeiffer, W.; Rohmer, M.; Spindler, C.; and Steeb, F.
Adaptive subwavelength control of nano-optical fields.
Nature **446(7133)**, 301–304 (2007).

[Aeschlimann10] Aeschlimann, M.; Bauer, M.; Bayer, D.; Brixner, T.; Cunovic, S.; Dimler, F.; Fischer, A.; Pfeiffer, W.; Rohmer, M.; Schneider, C.; Steeb, F.; Strüber, C.; and Voronine, D. V.
Spatiotemporal control of nanooptical excitations.
Proceedings of the National Academy of Sciences of the United States of America **107(12)**, 5329–5333 (2010).

[Agio13] Agio, M. and Alù, A., editors.
Optical Antennas.
Cambridge University Press (2013).

[Akimov07] Akimov, A. V.; Mukherjee, A.; Yu, C. L.; Chang, D. E.; Zibrov, A. S.; Hemmer, P. R.; Park, H.; and Lukin, M. D.
Generation of single optical plasmons in metallic nanowires coupled to quantum dots.
Nature **450(7168)**, 402–406 (2007).

[Allione08] Allione, M.; Temnov, V. V.; Fedutik, Y.; Woggon, U.; and Artemyev, M. V.
Surface Plasmon Mediated Interference Phenomena in Low-Q Silver Nanowire Cavities.
Nano Letters **8(1)**, 31–35 (2008).

[Alù08] Alù, A. and Engheta, N.
Input Impedance, Nanocircuit Loading, and Radiation Tuning of Optical Nanoantennas.
Physical Review Letters **101(4)**, 043,901 (2008).

[Assion98] Assion, A.; Baumert, T.; Bergt, M.; Brixner, T.; Kiefer, B.; Seyfried, V.; Strehle, M.; and Gerber, G.
Control of chemical reactions by feedback-optimized phase-shaped femtosecond laser pulses.
Science **282(5390)**, 919–922 (1998).

[Balistreri01] Balistreri, M. L. M.; Gersen, H.; Korterik, J. P.; Kuipers, L.; and van Hulst, N. F.
Tracking Femtosecond Laser Pulses in Space and Time.
Science **294(5544)**, 1080 –1082 (2001).

[Barnes03] Barnes, W. L.; Dereux, A.; and Ebbesen, T. W.
Surface plasmon subwavelength optics.
Nature **424(6950)**, 824–830 (2003).

[Bass95] Bass, M.
Handbook of Optics.
2nd edition. McGraw-Hill, New York (1995).

[Bennett70] Bennett, J. M.; Stanford, J. L.; and Ashley, E. J.
Optical Constants of Silver Sulfide Tarnish Films.
Journal of the Optical Society of America **60(2)**, 224–231 (1970).

[Berweger12] Berweger, S.; Atkin, J. M.; Olmon, R. L.; and Raschke, M. B.
Light on the Tip of a Needle: Plasmonic Nanofocusing for Spectroscopy on the Nanoscale.
The Journal of Physical Chemistry Letters **3(7)**, 945–952 (2012).

[Biagioni12] Biagioni, P.; Huang, J.-S.; and Hecht, B.
Nanoantennas for visible and infrared radiation.
Reports on Progress in Physics **75(2)**, 024,402 (2012).

[Bor88] Bor, Z.
Distortion of Femtosecond Laser Pulses in Lenses and Lens Systems.
Journal of Modern Optics **35**, 1907–1918 (1988).

[Bozhevolnyi06] Bozhevolnyi, S. I.; Volkov, V. S.; Devaux, E.; Laluet, J.-Y.; and Ebbesen, T. W.
Channel plasmon subwavelength waveguide components including interferometers and ring resonators.
Nature **440(7083)**, 508–511 (2006).

[Bozhevolnyi08] Bozhevolnyi, S. and García-Vidal, F.
Focus on Plasmonics.
New Journal of Physics **10(10)**, 105,001 (2008).

[Brinks11] Brinks, D.; Hildner, R.; Stefani, F. D.; and van Hulst, N. F.
Beating spatio-temporal coupling: implications for pulse shaping and coherent control experiments.
Optics Express **19(27)**, 26,486–26,499 (2011).

[Brixner01a] Brixner, T.
Adaptive Femtosecond Quantum Control.
Dissertation, Universität Würzburg (2001).

[Brixner01b] Brixner, T. and Gerber, G.
Femtosecond polarization pulse shaping.
Optics Letters **26(8)**, 557–559 (2001).

[Brixner05] Brixner, T.; García de Abajo, F. J.; Schneider, J.; and Pfeiffer, W.
Nanoscopic ultrafast space-time-resolved spectroscopy.
Physical Review Letters **95(9)**, 093,901–4 (2005).

[Brixner13] Brixner, T.; Aeschlimann, M.; Fischer, A.; Geisler, P.; Goetz, S.; Hecht, B.; Huang, J.-S.; Keitzl, T.; Kramer, C.; Melchior, P.; Pfeiffer, W.; Razinskas, G.; Rewitz, C.; Schneider, C.; Strüber, C.; Tuchscherer, P.; and Voronine, D. V.
Coherent spectroscopies on ultrashort time and length scales.
EPJ Web of Conferences **41**, 09,017 (2013).

[Cao10] Cao, L.; Nome, R. A.; Montgomery, J. M.; Gray, S. K.; and Scherer, N. F.
Controlling Plasmonic Wave Packets in Silver Nanowires.
Nano Letters **10(9)**, 3389–3394 (2010).

[Cheng10] Cheng, M.-T.; Luo, Y.-Q.; Wang, P.-Z.; and Zhao, G.-X.
Coherent controlling plasmon transport properties in metal nanowire coupled to quantum dot.
Applied Physics Letters **97(19)**, 191,903 (2010).

[Chiang94] Chiang, K. S.
Review of numerical and approximate methods for the modal analysis of general optical dielectric waveguides.
Optical and Quantum Electronics **26(3)**, S113–S134 (1994).

[Crutcher12] Crutcher, S. H.; Osei, A.; and Biswas, A.
Nonlinear evolution equations for surface plasmons for nano-focusing at a Kerr/metallic interface and tapered waveguide.
Optics & Laser Technology **44(4)**, 1156–1162 (2012).

[Curto10] Curto, A. G.; Volpe, G.; Taminiau, T. H.; Kreuzer, M. P.; Quidant, R.; and Hulst, N. F. v.
Unidirectional Emission of a Quantum Dot Coupled to a Nanoantenna.
Science **329(5994)**, 930–933 (2010).

[CVI09] CVI, M. G.
Gaussian Beam Optics.
In *CVI Melles Griot 2009 Technical Guide, Vol 2, Issue 1* (2009).

[Davoyan10] Davoyan, A. R.; Shadrivov, I. V.; Zharov, A. A.; Gramotnev, D. K.; and Kivshar, Y. S.
Nonlinear Nanofocusing in Tapered Plasmonic Waveguides.
Physical Review Letters **105(11)**, 116,804 (2010).

[Demtröder04] Demtröder, W.
Experimentalphysik, Bd. 2. Elektrizität und Optik.
3rd edition. Springer, Berlin (2004).

[Diels06] Diels, J.-C. and Rudolph, W.
Ultrashort Laser Pulse Phenomena: Fundamentals, Techniques, and Applications on a Femtosecond Time Scale (Optics and Photonics Series).
2nd edition. Academic Press Inc (2006).

[Ditlbacher02] Ditlbacher, H.; Krenn, J. R.; Felidj, N.; Lamprecht, B.; Schider, G.; Salerno, M.; Leitner, A.; and Aussenegg, F. R.
Fluorescence imaging of surface plasmon fields.
Applied Physics Letters **80(3)**, 404–406 (2002).

[Ditlbacher05] Ditlbacher, H.; Hohenau, A.; Wagner, D.; Kreibig, U.; Rogers, M.; Hofer, F.; Aussenegg, F. R.; and Krenn, J. R.
Silver Nanowires as Surface Plasmon Resonators.
Physical Review Letters **95(25)**, 257,403 (2005).

[Dorrer00] Dorrer, C.; Belabas, N.; Likforman, J.-P.; and Joffre, M.
Spectral resolution and sampling issues in Fourier-transform spectral interferometry.
Journal of the Optical Society of America B **17(10)**, 1795–1802 (2000).

[Dorrer01] Dorrer, C. and Joffre, M.
Characterization of the spectral phase of ultrashort light pulses.
Comptes Rendus de l'Académie des Sciences - Series IV - Physics **2(10)**, 1415–1426 (2001).

[Elechiguerra05] Elechiguerra, J. L.; Larios-Lopez, L.; Liu, C.; Garcia-Gutierrez, D.; Camacho-Bragado, A.; and Yacaman, M. J.
Corrosion at the Nanoscale: The Case of Silver Nanowires and Nanoparticles.
Chemistry of Materials **17(24)**, 6042–6052 (2005).

[Enderlein00] Enderlein, J.
Theoretical study of detection of a dipole emitter through an objective with high numerical aperture.
Optics Letters **25(9)**, 634–636 (2000).

[Etchegoin06] Etchegoin, P. G.; Le Ru, E. C.; and Meyer, M.
An analytic model for the optical properties of gold.
The Journal of Chemical Physics **125(16)**, 164,705–3 (2006).

[Fang10] Fang, Y.; Li, Z.; Huang, Y.; Zhang, S.; Nordlander, P.; Halas, N. J.; and Xu, H.
Branched Silver Nanowires as Controllable Plasmon Routers.
Nano Letters **10(5)**, 1950–1954 (2010).

[Frei09] Frei, F.; Galler, A.; and Feurer, T.
Space-time coupling in femtosecond pulse shaping and its effects on coherent control.
The Journal of Chemical Physics **130(3)**, 034,302–14 (2009).

[Fu12] Fu, Y.; Hu, X.; Lu, C.; Yue, S.; Yang, H.; and Gong, Q.
All-Optical Logic Gates Based on Nanoscale Plasmonic Slot Waveguides.
Nano Letters **12(11)**, 5784–5790 (2012).

[Fujiwara07] Fujiwara, H.
Spectroscopic ellipsometry: principles and applications.
John Wiley & Sons, Chichester, England; Hoboken, NJ (2007).

[Geisler13] Geisler, P.; Razinskas, G.; Krauss, E.; Wu, X.-F.; Rewitz, C.; Tuchscherer, P.; Goetz, S.; Huang, C.-B.; Brixner, T.; and Hecht, B.
Multimode Plasmon Excitation and In Situ Analysis in Top-Down Fabricated Nanocircuits.
Physical Review Letters **111(18)**, 183,901 (2013).

[Goetz12] Goetz, S.
Spektrale Interferometrie an plasmonischen Wellenleitern.
Master's thesis, Universität Würzburg (2012).

[Gramotnev05] Gramotnev, D. K.
Adiabatic nanofocusing of plasmons by sharp metallic grooves: Geometrical optics approach.
Journal of Applied Physics **98(10)**, 104,302 (2005).

[Gramotnev08] Gramotnev, D. K.; Vernon, K. C.; and Pile, D. F. P.
Directional coupler using gap plasmon waveguides.
Applied Physics B **93(1)**, 99–106 (2008).

[Gramotnev10] Gramotnev, D. K. and Bozhevolnyi, S. I.
Plasmonics beyond the diffraction limit.
Nature Photonics **4(2)**, 83–91 (2010).

[Grandidier08] Grandidier, J.; Massenot, S.; des Francs, G. C.; Bouhelier, A.; Weeber, J.-C.; Markey, L.; Dereux, A.; Renger, J.; González, M. U.; and Quidant, R.
Dielectric-loaded surface plasmon polariton waveguides: Figures of merit and mode characterization by image and Fourier plane leakage microscopy.
Physical Review B **78(24)**, 245,419 (2008).

[Guo13] Guo, X.; Ma, Y.; Wang, Y.; and Tong, L.
Nanowire plasmonic waveguides, circuits and devices.
Laser & Photonics Reviews pages 1–27 (2013).

[Halas10] Halas, N. J.
Plasmonics: An Emerging Field Fostered by Nano Letters.
Nano Letters **10(10)**, 3816–3822 (2010).

[Han13] Han, Z. and Bozhevolnyi, S. I.
Radiation guiding with surface plasmon polaritons.
Reports on Progress in Physics **76(1)**, 016,402 (2013).

[Hayashi12] Hayashi, S. and Okamoto, T.
Plasmonics: visit the past to know the future.
Journal of Physics D: Applied Physics **45(43)**, 433,001 (2012).

[Hecht02] Hecht, E.
Optics.
4th edition. Addison Wesley, San Francisco ; Munich [u.a.] (2002).

[Hecht06] Hecht, B. and Novotny, L.
Principles of Nano-Optics.
Cambridge University Press, Cambridge (2006).

[Huang09] Huang, J.-S.; Feichtner, T.; Biagioni, P.; and Hecht, B.
Impedance Matching and Emission Properties of Nanoantennas in an Optical Nanocircuit.
Nano Letters **9(5)**, 1897–1902 (2009).

[Huang10] Huang, J.-S.; Callegari, V.; Geisler, P.; Brüning, C.; Kern, J.; Prangsma, J. C.; Wu, X.; Feichtner, T.; Ziegler, J.; Weinmann, P.; Kamp, M.; Forchel, A.; Biagioni, P.; Sennhauser, U.; and Hecht, B.
Atomically flat single-crystalline gold nanostructures for plasmonic nanocircuitry.
Nature Communications **1(9)**, 150 (2010).

[Hung12] Hung, Y.-T.; Huang, C.-B.; and Huang, J.-S.
Plasmonic mode converter for controlling optical impedance and nanoscale light-matter interaction.
Optics Express **20(18)**, 20,342–20,355 (2012).

[Jeanmaire77] Jeanmaire, D. L. and Van Duyne, R. P.
Surface raman spectroelectrochemistry: Part I. Heterocyclic, aromatic, and aliphatic amines adsorbed on the anodized silver electrode.
Journal of Electroanalytical Chemistry and Interfacial Electrochemistry **84(1)**, 1–20 (1977).

[Johnson72] Johnson, P. B. and Christy, R. W.
Optical Constants of the Noble Metals.
Physical Review B **6(12)**, 4370–4379 (1972).

[Kane93] Kane, D. and Trebino, R.
Characterization of arbitrary femtosecond pulses using frequency-resolved optical gating.
IEEE Journal of Quantum Electronics **29(2)**, 571–579 (1993).

[Keitzl11] Keitzl, T.
Plasmonenpropagation an Nanostrukturen.
Diploma thesis, Universität Würzburg (2011).

[Klein86] Klein, M. V. and Furtak, T. E.
Optics.
2nd edition. Wiley (1986).

[Kolesov09] Kolesov, R.; Grotz, B.; Balasubramanian, G.; Stohr, R. J.; Nicolet, A. A. L.; Hemmer, P. R.; Jelezko, F.; and Wrachtrup, J.
Wave-particle duality of single surface plasmon polaritons.
Nature Physics **5(7)**, 470–474 (2009).

[Könenkamp12] Könenkamp, R.; Word, R. C.; Fitzgerald, J. P. S.; Nadarajah, A.; and Saliba, S. D.
Controlled spatial switching and routing of surface plasmons in designed single-crystalline gold nanostructures.
Applied Physics Letters **101(14)**, 141,114–4 (2012).

[Krenz10] Krenz, P. M.; Olmon, R. L.; Lail, B. A.; Raschke, M. B.; and Boreman, G. D.
Near-field measurement of infrared coplanar strip transmission line attenuation and propagation constants.
Optics Express **18(21)**, 21,678–21,686 (2010).

[Kriesch13] Kriesch, A.; Burgos, S. P.; Ploss, D.; Pfeifer, H.; Atwater, H. A.; and Peschel, U.
Functional Plasmonic Nanocircuits with Low Insertion and Propagation Losses.
Nano Letters **13(9)**, 4539–4545 (2013).

[Langhojer09] Langhojer, F.
New Techniques in Liquid-Phase Ultrafast Spectroscopy.
Dissertation, Universität Würzburg (2009).

[Laroche07] Laroche, T.; Vial, A.; and Roussey, M.
Crystalline structure's influence on the near-field optical properties of single plasmonic nanowires.
Applied Physics Letters **91(12)**, 123,101 (2007).

[Laux98] Laux, S.; Kaiser, N.; Zöller, A.; Götzelmann, R.; Lauth, H.; and Bernitzki, H.
Room-temperature deposition of indium tin oxide thin films with plasma ion-assisted evaporation.
Thin Solid Films **335(1-2)**, 1–5 (1998).

[Lepetit95] Lepetit, L.; Chériaux, G.; and Joffre, M.
Linear Techniques of Phase Measurement by Femtosecond Spectral Interferometry for Applications in Spectroscopy.
Journal of the Optical Society of America B **12(12)**, 2467–2474 (1995).

[Li10] Li, Z.; Bao, K.; Fang, Y.; Huang, Y.; Nordlander, P.; and Xu, H.
Correlation between Incident and Emission Polarization in Nanowire Surface Plasmon Waveguides.
Nano Letters **10(5)**, 1831–1835 (2010).

[Li11] Li, Z.; Zhang, S.; Halas, N. J.; Nordlander, P.; and Xu, H.
Coherent Modulation of Propagating Plasmons in Silver-Nanowire-Based Structures.
Small **7(5)**, 593–596 (2011).

[Lieb04] Lieb, M. A.; Zavislan, J. M.; and Novotny, L.
Single-molecule orientations determined by direct emission pattern imaging.
Journal of the Optical Society of America B **21(6)**, 1210–1215 (2004).

[Lindquist12] Lindquist, N. C.; Nagpal, P.; McPeak, K. M.; Norris, D. J.; and Oh, S.-H.
Engineering metallic nanostructures for plasmonics and nanophotonics.
Reports on Progress in Physics **75(3)**, 036,501 (2012).

[Liu05] Liu, J.-M.
Photonic devices.
Cambridge, Cambridge; New York (2005).

[Liu13] Liu, N.; Wei, H.; Li, J.; Wang, Z.; Tian, X.; Pan, A.; and Xu, H.
Plasmonic Amplification with Ultra-High Optical Gain at Room Temperature.
Scientific Reports **3** (2013).

[Lumerical12] Lumerical, I.
Imaging | FDTD solutions knowledge base (2012).
Http://docs.lumerical.com/en/fdtd/microscopy_imaging.html.

[Ly-Gagnon12] Ly-Gagnon, D.-S.; Balram, K. C.; White, J. S.; Wahl, P.; Brongersma, M. L.; and Miller, D. A.
Routing and photodetection in subwavelength plasmonic slot waveguides.
Nanophotonics **1(1)** (2012).

[Maier07] Maier, S. A.
Plasmonics: Fundamentals and Applications.
1st edition. Springer, Berlin (2007).

[Mühlschlegel05] Mühlschlegel, P.; Eisler, H.-J.; Martin, O. J. F.; Hecht, B.; and Pohl, D. W.
Resonant Optical Antennas.
Science **308(5728)**, 1607–1609 (2005).

[Mukamel99] Mukamel, S.
Principles of Nonlinear Optical Spectroscopy.
1st edition. Oxford University Press, New York (1999).

[Ni05] Ni, C.; Hassan, P. A.; and Kaler, E. W.
Structural Characteristics and Growth of Pentagonal Silver Nanorods Prepared by a Surfactant Method.
Langmuir **21(8)**, 3334–3337 (2005).

[Nicon13] Nicon.
MicroscopyU.com - the source for microscopy education (2013).
Http://www.microscopyu.com/articles/optics/cfintro.html.

[Novotny94] Novotny, L. and Hafner, C.
Light propagation in a cylindrical waveguide with a complex, metallic, dielectric function.
Physical Review E **50(5)**, 4094 (1994).

[Novotny11] Novotny, L. and van Hulst, N.
Antennas for light.
Nature Photonics **5(2)**, 83–90 (2011).

[Ozbay06] Ozbay, E.
Plasmonics: Merging Photonics and Electronics at Nanoscale Dimensions.
Science **311(5758)**, 189–193 (2006).

[Palik97] Palik, E. D.
Handbook of Optical Constants of Solids.
Academic Press, New York (1997).

[Pan13] Pan, D.; Wei, H.; and Xu, H.
Optical interferometric logic gates based on metal slot waveguide network realizing whole fundamental logic operations.
Optics Express **21(8)**, 9556 (2013).

[Pettersson95] Pettersson, L. A. A. and Snyder, P. G.
Preparation and characterization of oxidized silver thin films.
Thin Solid Films **270(1-2)**, 69–72 (1995).

[Prade91] Prade, B.; Vinet, J. Y.; and Mysyrowicz, A.
Guided optical waves in planar heterostructures with negative dielectric constant.
Physical Review B **44(24)**, 13,556–13,572 (1991).

[Radzewicz96] Radzewicz, C.; la Grone, M.; and Krasinski, J.
Interferometric measurement of femtosecond pulse distortion by lenses.
Optics Communications **126(4-6)**, 185–190 (1996).

[Reiserer09] Reiserer, A.
Functional elements on subwavelength plasmonic waveguides.
Master's thesis, Universität Würzburg (2009).

[Reiserer10] Reiserer, A. A.; Huang, J.-S.; Hecht, B.; and Brixner, T.
Subwavelength broadband splitters and switches for femtosecond plasmonic signals.
Optics Express **18(11)**, 11,810–11,820 (2010).

[Rewitz09] Rewitz, C.
Analytische und adaptive kohärente Kontrolle optischer Nahfelder durch Formung ultrakurzer Laserpulse.
Diploma thesis, Universität Würzburg (2009).

[Rewitz12a] Rewitz, C.; Keitzl, T.; Tuchscherer, P.; Goetz, S.; Geisler, P.; Razinskas, G.; Hecht, B.; and Brixner, T.
Spectral-interference microscopy for characterization of functional plasmonic elements.
Optics Express **20(13)**, 14,632–14,647 (2012).

[Rewitz12b] Rewitz, C.; Keitzl, T.; Tuchscherer, P.; Huang, J.-S.; Geisler, P.; Razinskas, G.; Hecht, B.; and Brixner, T.
Ultrafast Plasmon Propagation in Nanowires Characterized by Far-Field Spectral Interferometry.
Nano Letters **12(1)**, 45–49 (2012).

[Rewitz14] Rewitz, C.; Razinskas, G.; Geisler, P.; Krauss, E.; Goetz, S.; Pawłowska, M.; Hecht, B.; and Brixner, T.
Coherent Control of Plasmon Propagation in a Nanocircuit.
Physical Review Applied **1(1)**, 014,007 (2014).

[RI13] RI, I.
RefractiveIndex.INFO - Refractive index database (2013).

[Rokitski05] Rokitski, R.; Tetz, K. A.; and Fainman, Y.
Propagation of Femtosecond Surface Plasmon Polariton Pulses on the Surface of a Nanostructured Metallic Film: Space-Time Complex Amplitude Characterization.
Physical Review Letters **95(17)**, 177,401 (2005).

[Ropers06] Ropers, C.; Stibenz, G.; Steinmeyer, G.; Müller, R.; Park, D.; Lee, K.; Kihm, J.; Kim, J.; Park, Q.; Kim, D.; and Lienau, C.
Ultrafast dynamics of surface plasmon polaritons in plasmonic metamaterials.
Applied Physics B **84(1-2)**, 183–189 (2006).

[Sanders06] Sanders, A. W.; Routenberg, D. A.; Wiley, B. J.; Xia, Y.; Dufresne, E. R.; and Reed, M. A.
Observation of Plasmon Propagation, Redirection, and Fan-Out in Silver Nanowires.
Nano Letters **6(8)**, 1822–1826 (2006).

[Sandtke08] Sandtke, M.; Engelen, R. J. P.; Schoenmaker, H.; Attema, I.; Dekker, H.; Cerjak, I.; Korterik, J. P.; Segerink, B.; and Kuipers, L.
Novel instrument for surface plasmon polariton tracking in space and time.
Review of Scientific Instruments **79(1)**, 013,704 (2008).

[Schnell11] Schnell, M.; Alonso-Gonzalez, P.; Arzubiaga, L.; Casanova, F.; Hueso, L. E.; Chuvilin, A.; and Hillenbrand, R.
Nanofocusing of mid-infrared energy with tapered transmission lines.
Nature Photonics **5(5)**, 283–287 (2011).

[Schouten05] Schouten, H. F.; Kuzmin, N.; Dubois, G.; Visser, T. D.; Gbur, G.; Alkemade, P. F. A.; Blok, H.; Hooft, G. W. '.; Lenstra, D.; and Eliel, E. R.
Plasmon-Assisted Two-Slit Transmission: Young's Experiment Revisited.
Physical Review Letters **94(5)**, 053,901 (2005).

[Schramm00] Schramm, S.
Ausbau eines Femtosekunden-Lasersystems.
Diplomarbeit, Universität Würzburg (2000).

[Shegai11] Shegai, T.; Miljkovic, V. D.; Bao, K.; Xu, H.; Nordlander, P.; Johansson, P.; and Käll, M.
Unidirectional Broadband Light Emission from Supported Plasmonic Nanowires.
Nano Letters **11(2)**, 706–711 (2011).

[Singh12] Singh, D.; Raghuwanshi, M.; and Pavan Kumar, G. V.
Propagation of light in serially coupled plasmonic nanowire dimer: Geometry dependence and polarization control.
Applied Physics Letters **101(11)**, 111,111–5 (2012).

[Stockman02] Stockman, M. I.; Faleev, S. V.; and Bergman, D. J.
Coherent control of femtosecond energy localization in nanosystems.
Physical Review Letters **88(6)**, 067,402–4 (2002).

[Stockman04] Stockman, M. I.
Nanofocusing of Optical Energy in Tapered Plasmonic Waveguides.
Physical Review Letters **93(13)**, 137,404 (2004).

[Sukharev06] Sukharev, M. and Seideman, T.
Phase and Polarization Control as a Route to Plasmonic Nanodevices.
Nano Letters **6(4)**, 715–719 (2006).

[Takahara97] Takahara, J.; Yamagishi, S.; Taki, H.; Morimoto, A.; and Kobayashi, T.
Guiding of a one-dimensional optical beam with nanometer diameter.
Optics Letters **22(7)**, 475–477 (1997).

[Temnov07] Temnov, V. V.; Woggon, U.; Dintinger, J.; Devaux, E.; and Ebbesen, T. W.
Surface plasmon interferometry: measuring group velocity of surface plasmons.
Optics Letters **32(10)**, 1235–1237 (2007).

[Träger12] Träger, F.
Springer handbook of lasers and optics.
Springer handbooks, 2nd edition. Springer, Berlin [u.a.] (2012).

[Trebino93] Trebino, R. and Kane, D. J.
Using phase retrieval to measure the intensity and phase of ultrashort pulses: frequency-resolved optical gating.
Journal of the Optical Society of America A **10(5)**, 1101–1111 (1993).

[Trebino02] Trebino, R.
Frequency-Resolved Optical Gating: The Measurement of Ultrashort Laser Pulses.
Har/Cdr edition. Springer Netherlands (2002).

[Tuchscherer09] Tuchscherer, P.; Rewitz, C.; Voronine, D. V.; García de Abajo, F. J.; Pfeiffer, W.; and Brixner, T.
Analytic coherent control of plasmon propagation in nanostructures.
Optics Express **17(16)**, 14,235–14,259 (2009).

[Tuchscherer12] Tuchscherer, P.
A Route to Optical Spectroscopy on the Nanoscale.
Dissertation, Universität Würzburg (2012).

[Voll97] Voll, S.
Aufbau und Theorie eines Festkörper-Femtosekundenlasers.
Diplomarbeit, Universität Würzburg (1997).

[Wefers96] Wefers, M. and Nelson, K.
Space-time profiles of shaped ultrafast optical waveforms.
IEEE Journal of Quantum Electronics **32(1)**, 161–172 (1996).

[Wei11a] Wei, H.; Li, Z.; Tian, X.; Wang, Z.; Cong, F.; Liu, N.; Zhang, S.; Nordlander, P.; Halas, N. J.; and Xu, H.
Quantum Dot-Based Local Field Imaging Reveals Plasmon-Based Interferometric Logic in Silver Nanowire Networks.
Nano Letters **11(2)**, 471–475 (2011).

[Wei11b] Wei, H.; Wang, Z.; Tian, X.; Kall, M.; and Xu, H.
Cascaded logic gates in nanophotonic plasmon networks.
Nature Communications **2**, 387 (2011).

[Wei12] Wei, H. and Xu, H.
Controlling surface plasmon interference in branched silver nanowire structures.
Nanoscale **4(22)**, 7149–7154 (2012).

[Wen09] Wen, J.; Romanov, S.; and Peschel, U.
Excitation of plasmonic gap waveguides by nanoantennas.
Optics Express **17(8)**, 5925–5932 (2009).

[Wollenhaupt07] Wollenhaupt, M.; Assion, A.; and Baumert, T.
Femtosecond Laser Pulses: Linear Properties, Manipulation, Generation and Measurement.
In Träger, F., editor, *Springer Handbook of Lasers and Optics*, pages 937–983. Springer Science+Business Media, New York (2007).

[Yan09] Yan, R.; Pausauskie, P.; Huang, J.; and Yang, P.
Direct photonic–plasmonic coupling and routing in single nanowires.
Proceedings of the National Academy of Sciences **106(50)**, 21,045 –21,050 (2009).

[Yariv89] Yariv, A.
Quantum Electronics.
3rd edition. Wiley (1989).

[Zhang11] Zhang, S.; Wei, H.; Bao, K.; Håkanson, U.; Halas, N. J.; Nordlander, P.; and Xu, H.
Chiral Surface Plasmon Polaritons on Metallic Nanowires.
Physical Review Letters **107(9)**, 096,801 (2011).

[Zia06] Zia, R.; Schuller, J. A.; Chandran, A.; and Brongersma, M. L.
Plasmonics: the next chip-scale technology.
Materials Today **9(7-8)**, 20–27 (2006).

Acknowledgements

This dissertation summarizes the results of my work as a PhD student, which I did not achieve solitary but by being part of different teams. The fruitful and helpful environment at the "Lehrstuhl für Physikalische und Theoretische Chemie I" forms a basis for my accomplishments.

Even though it might not be possible to acknowledge every support, I want to thank some persons explicitly:

- *Prof. Dr. Tobias Brixner* for giving me the opportunity to perform my PhD studies in his well-equipped work group and for securing funding, mostly via the DFG program SPP 1391. Furthermore, I want to thank him for providing his feedback and ideas. Evenly valuable are the skills I acquired due to his supervision.

- *Prof. Dr. Bert Hecht* for his important contributions regarding the successful cooperation within the SPP 1391, the regular meetings that allowed me to structure and promote my projects, and for the invitation to the "Hiking-Seminar" of his work group. Moreover, I appreciate the pleasant level of communication and his extra time for scientific discussions in which I learned a lot.

- *Dr. Philip Tuchscherer* for his great support on both—the professional and personal level. I admire the way he handles problems.

- *Thomas Keitzl* and *Sebastian Götz* for working with me during their Diploma and Master's thesis, respectively. Furthermore, I want to thank *Dr. Monika Pawłowska* for her contributions during the last part of my studies, and *Sebastian Götz* for continuing the work in "Lab3".

- *Peter Geisler*, *Gary Razinskas*, and *Enno Krauss* for providing gold nanostructures, simulation data, and their expertise in our cooperation. Special thanks go to *Gary Razinskas*, who was very helpful by performing additional simulations for the theory part of this dissertation and who was not afraid of extra discussions in this context.

- *Dr. Monika Pawłowska*, *Sebastian Götz*, and *Christian Kramer* for carefully proofreading the entire dissertation and providing valuable comments. The same holds for *Johannes Kern* and *Philipp Rudolf* who commented on the Introduction and Summary.

- *Dr. Jer-Shing Huang* for his drive to transfer knowledge, his sincerity, and the fun.

- *Dr. Patrick Nürnberger* for his openness with respect to my questions, his scientifically sound answers, and his lunch-stories.

- My full-time office colleagues *Philipp Rudolf* and *Florian Kanal* for the great atmosphere, for always lending a sympathetic ear to me and the resulting professional and personal support, and for sharing ups and downs. I also appreciate both—accepting and ignoring the "red light".

- *Dr. Johannes Buback* / *Andreas Steinbacher*, *Christoph Schwarz*, and *Philipp Rudolf* for managing the VI-Pool, the workstations, and Zotero, respectively.

- *Former and current scientific members* of the "Lehrstuhl für Physikalische und Theoretische Chemie I" for valuable feedback or ideas, e.g., in status reports, as well as for common sports activities with some of them.

- *Johannes Kern* for sharing his knowledge on nanooptics in numerous discussions, and for scanning electron micrographs of one of my first silver nanowire samples.

- The *members of the machine and electronic workshop* for their proactive attitude.

- The *technical assistants*, as well as our secretary, *Andrea Gehring*. Many things would break down without their personal involvement.

- *Stefan Rützel* for managing the supply of coffee and—more important for me—snacks.

- The *"Stammtisch" guys* for the exceptional friendships that already have been lasting for several years, and for their support throughout all my studies and personal experiences.

- My *basketball team* for the distraction from work and the fun—on and off the court.

Last but not least I want to thank my parents for their love and support.